TÉCNICO LISBOA

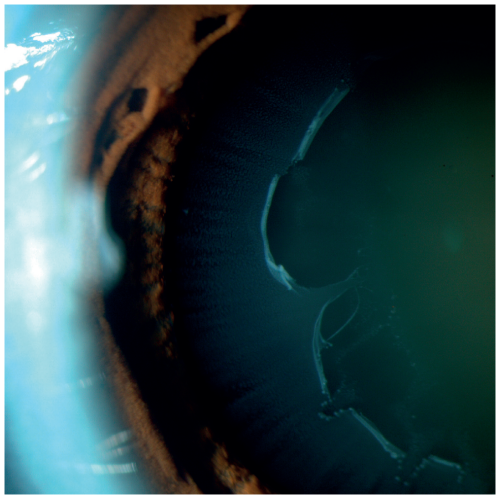

Biomechanical Analysis of the Crystalline Lens Complex: A Computational Model

Leonor Mariana Jud Guedes de Campos

Thesis to obtain the Master of Science Degree in

Mechanical Engineering

Supervisors: Prof. Paulo Rui Alves Fernandes
Prof. André Paulo Galvão de Castro

Examination Committee

Chairperson: Prof. Luís Filipe Galrão dos Reis
Supervisor: Prof. Paulo Rui Alves Fernandes
Members of the Committee: Prof. João Orlando Marques Gameiro Folgado
Prof. Maria Filomena Jorge Ribeiro

October 2021

Agradecimentos

Gostaria de agradecer o auxílio que me foi dado ao longo do desenvolvimento desta tese pelos Professores Paulo Fernandes e André Castro, bem como o apoio dado pelo Professor Rui Rúben, que se mostraram sempre disponíveis para me orientar.

Igualmente, queria agradecer à Dra. Filomena Ribeiro e ao Dr. Bernardo Feijóo, pelos seus contributos, em particular, pela sua ajuda no entendimento de conceitos médicos que foram essenciais no desenvolvimento deste trabalho.

À minha querida avó, cuja amizade foi constante e incansável desde sempre e ao Rodrigo, pelo seu apoio incondicional ao longo de todos estes anos.

Por fim, aos meus amigos do Técnico, mas que serão amigos muito para além disso, Mags e Rafas.

Resumo

O estudo do complexo do cristalino e das suas degenerações carece de conhecimentos tanto de base clínica como experimental. A presente dissertação pretende diminuir a carência de conhecimentos acerca da síndrome da pseudoexfoliação, facultando respostas sobre os comportamentos biomecânicos e ópticos da lente nessas condições.

Cristalinos de 62 anos foram modelados em variadas condições saudáveis e degenerativas, de forma a simular o impacto da síndrome mencionada. Os modelos desenvolvidos incluem o núcleo e córtex da lente, o saco capsular e as zónulas anteriores, equatoriais e posteriores. O alongamento das zónulas leva ao achatamento da lente, representando a mudança do estado de visão próxima para visão distante.

A pseudoexfoliação foi modelada tendo em conta dois níveis de severidade para cada zónula, bem como para o conjunto de zónulas anterior e equatorial e para todos os conjuntos de fibras. Adicionalmente, a sua origem e extensão foram estudadas.

Os resultados da presente dissertação reiteram a importância da correcta representação geométrica das zónulas, bem como uma correcta ancoragem destas estruturas ao saco capsular, no sentido de obter resultados apropriados de amplitude de acomodação para as lentes modeladas. No que toca à síndrome da pseudoexfoliação, este trabalho permitiu quantificar as tensões suportadas pelas estruturas com a progressão da doença, bem como a perda progressiva da amplitude de acomodação da lente, apontando as regiões de maior risco de degeneração.

Desta forma, o trabalho desenvolvido torna-se de elevado interesse a oftalmologistas que se envolvam no estudo da doença mencionada.

Palavras-chave: Cristalino, Pseudoexfoliação, Saco capsular, Zónulas, Método dos Elementos Finitos

Abstract

In the context of the study of the crystalline lens complex and its disorders, the lack of available clinical and experimental data demands the need for finite element method studies. This dissertation was developed with the objective of comprehending the relevant features that can lead to the worsening of an individual's visual capacity due to the pseudoexfoliation syndrome.

Models for a 62 year-old lens complex were developed, composed by the capsule, cortex and nucleus and anterior, equatorial and posterior zonular fibres. The stretching of the zonules changes the shape of the lens, from an accommodated to a relaxed state (near-to-far vision). Healthy and pseudoexfoliative conditions were assessed, with the latter being analyzed for each zonule individually, as well as for the groupings of anterior and equatorial zonules and of all the zonular sets. The zonulopathy origin was examined, as well as its extension throughout the whole composition of the zonules.

The results found in this work highlight the correct representation of the geometrical parameters of the zonules, as well as their anchorage to the capsular bag, in order to model an optimized design of the healthy crystalline lens. The pseudoexfoliation syndrome results quantified the stress variation endured by the components of the lens complex with the progression of the disease, as well as the lenticular accommodation amplitude reduction with the syndrome. Finally, the pseudoexfoliative locations that presented a greater risk were identified.

Taking into account these results, the present work becomes a valuable asset in the study of the mentioned syndrome.

Keywords: Crystalline lens, Pseudoexfoliation Syndrome, Zonular Fibers, Capsular Bag, Finite Element Method

Contents

List of Tables

List of Figures

Chapter 1

Introduction

The human crystalline lens allows the transmission and convergence of the light received by the eye into the retina, and it is a vital optical component of the human eye. Additionally, the change in shape of this component, with the support of the surrounding structures, allows for the variation between near and distant visions. As such, the study of the behavior of this complex becomes of utmost importance, on both healthy and diseased conditions.

1.1 Motivation

The present dissertation aims to evaluate the biomechanical and optical behaviors of the healthy lens complex, as well as depict the effects of zonulopathy in the lenticular system, in particular, under conditions of the pseudoexfoliation syndrome.

Ritch and Schlötzer-Schrehardt (2001) defined the pseudoexfoliation syndrome as the pathological production and accumulation of abnormal fibrillar extracellular material in ocular tissues. Nonetheless, this condition also affects extraocular structures, such as the heart, lungs, liver, kidneys, skin and blood vessels.

Pseudoexfoliation affects up to 30% of people older than 60 years-old in a worldwide distribution (Ritch and Schlötzer-Schrehardt, 2001). Under these circumstances, 70 million individuals are estimated to live with this condition. This age-related disease is often correlated with cataract and glaucoma conditions (Pedrosa et al., 2016).

Due to the progress in today's medicine that leads to health promotion and disease prevention, the population age group of 60 years-old and older is growing faster than any other age group (World Health Organization, 2002). As such, the prevalence of this condition will increase even further (Schlötzer-Schrehardt and Naumann, 2006).

Some of the first manifestations of the syndrome can be observed with the detection of white pseudoexfoliative material clumps in the anterior surface of the lens capsule, as can be seen in Figure 1.1, where slit-lamp examination shows the white deposits of material in this region.

Accordingly, this condition heavily impacts the zonular fiber integrity and is referred to as one of the

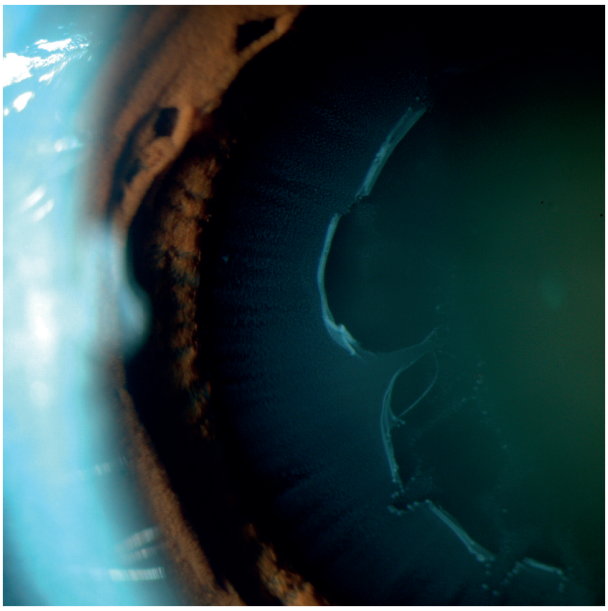

Figure 1.1: Pseudoexfoliation deposits on the anterior capsule of the lens (adapted from Pedrosa et al. (2016)).

most probable causes of adult-onset zonular dialysis and instability (Hoffman et al., 2013).

In involved eyes, the risk of conditions such as spontaneous subluxation or dislocation of the lens (*ectopia lentis*) can be up to ten times higher than in healthy eyes (Ritch and Schlötzer-Schrehardt, 2001).

In developing countries, pseudoexfoliation leads to a higher rate of preoperative complications, due to the postponing of needed treatment and interventions. Patients with this syndrome presented severe conditions such as subluxation and dislocation of the lens, with incidences of 52% and 4%, respectively, before undergoing cataract surgery (Schlötzer-Schrehardt and Naumann, 2006).

Pseudoexfoliation can also lead to serious complications during timely cataract surgery, such as poor pupil dilation and higher risk of vitreous loss, capsular rupture and further zonular dialysis. Additionally, the condition of phacodonesis i.e., the vibration and instability of the lens, has a higher occurrence for pseudoexfoliative eyes. The syndrome also yields a greater risk of post-surgical subluxation or dislocation of the new lens complex, also known as in-the-bag intraocular lens dislocation (Schlötzer-Schrehardt and Naumann, 2006). Studies conducted on post-surgery late in-the-bag dislocation, in 38 eyes, found that 44% of the total number of cases had pseudoexfoliation as a predisposing factor (Hayashi et al., 2007).

Schlötzer-Schrehardt and Naumann (2006) denoted that, despite the frequency and clinical importance of the pseudoexfoliation syndrome, there was little emphasis on research related to this disorder. Nonetheless, the authors pointed out that the prevalence of the more advanced stages of the disease will increase, due to the rising life expectancy of the world population.

Given all the previously mentioned factors of the pseudoexfoliation syndrome, the need to understand the biomechanical behavior of the eye with such a condition becomes crucial, since the biomechanical effects of the disease can bring knowledge related to the severity of the zonular dialysis and the best way to approach it, in a surgical context.

1.2 Objectives

The main goals of this dissertation are the creation of a comprehensive numerical study of the healthy lens complex and the analysis of the biomechanical impact caused by the pseudoexfoliation syndrome in the affected structures. This work is implemented with the intent of obtaining data that can be relevant in the evaluation of the severity of this disease, as well as understanding possible ways to approach it, from a clinical standpoint.

Bearing this in mind, the present work resorts to the use of finite element (FE) modeling, with the objective of gaining insight into the complex biomechanical problem of accommodation under healthy and diseased conditions. The use of this method becomes even more prominently necessary due to the scarcity of available clinical and experimental data (Wang and Pierscionek, 2019).

In order to replicate the biomechanical behavior of the human lens complex, this work intends to develop various three-dimensional (3D) models of the involved structures, with the goal of obtaining knowledge related to the healthy conditions of the system. Additionally, different geometry and boundary conditions are to be simulated in the healthy human lens, with the intention of discerning the biomechanical effects of these changes in the lens complex.

Moreover, with the objective of providing relevant clinical data, this dissertation also proposes to understand the optical behavior of the lens, by measuring the optical power evolution of the lens throughout its deformation.

When assessing the pseudoexfoliation syndrome and its impact in the system of interest, the condition of zonular dialysis is to be established in the healthy lens complex, in order to achieve a gradual and realistic depiction of this condition. Additionally, this dissertation proposes to provide a quantification of the visual capacity of the lens, related to its ability to accommodate, when afflicted by the pseudoexfoliation syndrome.

1.3 Overview and Document Structure

The present chapter introduces the reader to the subject of study in this dissertation, highlighting the need for the development of such work and depicting its essential motivation.

Chapter 2 provides a description of the related work conducted both in clinical and *in silico* settings. The clinical approach to the human lens complex is portrayed in this chapter, accounting for both healthy and diseased conditions and the underlying mechanisms that effect the transition from the former circumstance to the latter. On a similar note, the data available in the literature regarding the lens complex in FE computational studies is analyzed and accounted for.

Chapter 3 depicts the methodologies followed throughout the work in this dissertation, along with the tools and resources used to implement the selected approaches. Models for the healthy lens complex are developed, as well as models that simulate the pseudoexfoliation disease in the involved structures.

In Chapter 4, the results of the methodologies applied are laid out and discussed; an initial model of the healthy lens complex is validated and compared with literature data; and, additionally, the outcomes

from the optimizations of this model and from impositions of pseudoexfoliative conditions are thoroughly evaluated and reviewed.

Chapter 5 gives final remarks for the developed work, reporting its contributions and providing pointers for future work. The relevant scientific publications related to this dissertation are laid out in the following chapter and lastly, Appendixes A, B and C depict additional data for this work.

Chapter 2

Literature Review

The present chapter reports on the available literature on the lens complex, both in clinical and *in silico* contexts. The human crystalline lens is the optical component with the purpose of refracting and transmitting the light that enters the eye, and focusing it in the retina. This transparent structure also allows for the change in optical power of the human eye, guaranteeing its focus adjustment in objects at various distances, as a result of the accommodation process.

2.1 Clinical Background

In addressing the clinical studies of the human lens, this section approaches the crystalline and its surrounding structures from a healthy perspective, whilst also describing the most prominent alterations caused by the pseudoexfoliation syndrome, a condition that has a significant impact in the weakness of the zonular fibers.

2.1.1 The Lens Complex Anatomy and Accommodation

The crystalline lens is placed in the anterior segment of the eye, posterior to the iris and anterior to the vitreous body. The architecture of the eye can be observed in Figure 2.1, where the representation of the horizontal section of the ocular structures is depicted.

A closer perspective of the lens and its surrounding structures can be observed in Figure 2.2, where the sectional view of the ocular structures is depicted. The lens is composed by its cortical and nuclear regions and it is contained by an elastic membrane, also known as the capsular bag.

This structure is then connected to the main ocular architecture by the zonular fibers i.e., the suspensory ligament of the lens, which originate on the ciliary muscle. The fibers are divided in three different sets: the anterior, equatorial and posterior zonules.

The accommodation process is the mechanism that allows the change of optical power of the lens, in order to focus on objects at various distances. This is due to the shape alteration of the crystalline lens, provided by the deformation of the capsule. This deformation is achieved with the tension generated by the ciliary muscle, that is transmitted by the zonular fibers, altering the shape of the capsular bag.

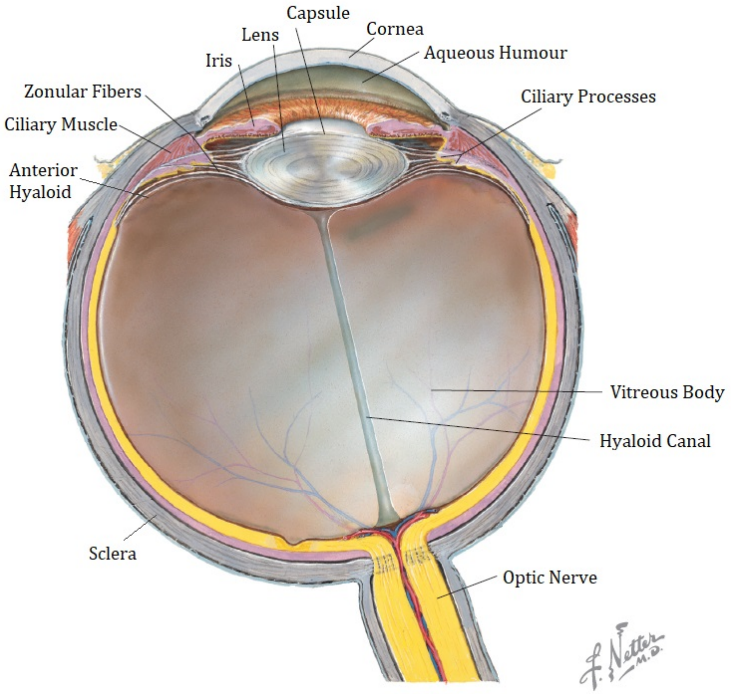

Figure 2.1: The ocular architecture (adapted from Netter (2010)).

In regards to the change of the lens shape, the most unanimous theory that explains the accommodation mechanism is presented by Helmholtz (Von Helmholtz and Southall, 1924). The authors understanding of the change of focus provided by the lens states is described as the Helmholtz theory of accommodation and states the following:

- The focus of the eye on a distant object is achieved with the relaxation of the ciliary muscle, which stretches the zonular fibers, and leads to the elongation of the lens, reaching the unaccommodated state (see Figure 2.3a).
- The eye, when focusing on a nearby object, leads to the contraction of the ciliary muscle and the consequent release of tension on the zonular fibers. This movement causes the lens to increase its curvature and thicken, coming to the accommodated state (see Figure 2.3b).

Nonetheless, the lens is subjected to permanent changes in its structure throughout the life of an individual. Atchison et al. (2000) referred to the crystalline lens as the optical component that suffers the most substantial age-related alterations. The lens shape, size and mass vary as one ages, and the accommodative capacity of an individual reduces significantly with age.

The condition of presbyopia is closely related to the gradual loss of accommodative ability in the aging eye. This ailment is characterized by the increasing difficulty that an individual faces when focusing on close objects (e.g. reading) and can be alleviated with the use of appropriate spectacles, in order to aid in nearby object visualization (Ribeiro, 2019). This condition affects more than one billion people worldwide and its on-set age ranges from 40 to 45 years-old (Holden et al., 2008).

The underlying cause of presbyopia remains undefined, even though its known origin is in the accommodative system. The causes can either be the changes in the lens and its capsule, the changes

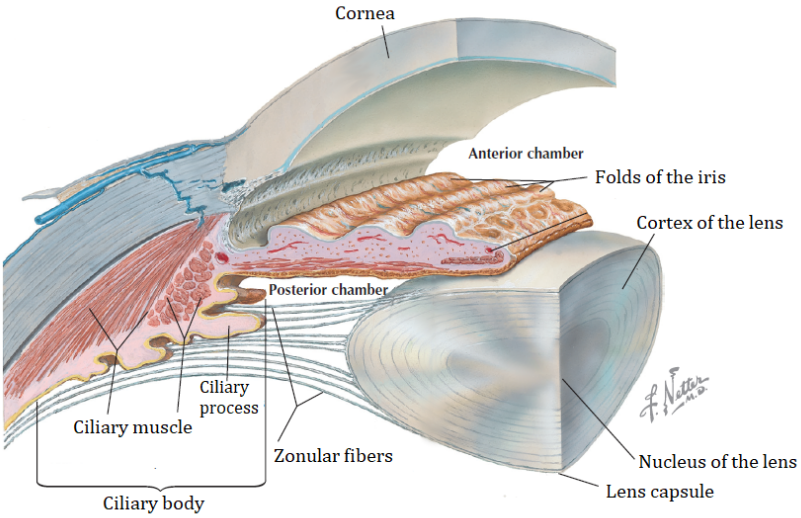

Figure 2.2: The lens and its surrounding structures (adapted from Netter (2010)).

in their supporting structures, or a combination of both. Additionally, the individual contribution of these factors can vary for each individual (Atchison et al., 2000).

Pierscionek et al. (2015) studied the age-related variations in the lens. In total, 66 lenses were studied, ranging from the ages of 16 to 91 years-old. The *ex-vivo* lenses were presumed to be in an accommodated form, since their removal lead to the lack of tension from the zonular fibers. The authors denoted a progressive growth of the eye lens throughout the human life, due to the continued accumulation of new cells in the lens, without any sort of tissue loss. Nonetheless, the authors pointed out the observation that there were individual variations in each lens.

As previously mentioned, the lens shape variation causes a change in its equivalent power (Atchison et al., 2000). The lenticular equivalent optical power measures how strongly the lens converges the receiving light. The optical power's international system of unit is the inverse meter (m^{-1}), which is more regularly named as dioptre (D).

Equation 2.1 allows the computation of the Central Optical Power (COP), a quantity that calculates the dioptres of the crystalline lens in its optical axis i.e., the straight line passing through the geometrical center of the lens, and joining the two centers of curvature of its anterior and posterior surfaces.

$$COP = \frac{n_l - n_p}{r_a} + \frac{n_l - n_p}{r_p} - \frac{t \cdot (n_l - n_p)^2}{r_a \cdot r_p \cdot n_l} \tag{2.1}$$

Where n_l stands for the refractive index of the lens and n_p the refractive index of the aqueous humour and vitreous body. The refractive indexes of these structures measure the bending degrees of a ray of light when passing through each of the mediums. Variable t represents the total thickness of the lens and r_a and r_p are the anterior and posterior radii of curvature, respectively. Such quantities are displayed in Figure 2.4, as well as the optical axis, ξ, where the lens is depicted in both the relaxed and accommodated states.

The value of the refractive index of the aqueous humour and vitreous is $n_p = 1.336$. The refractive

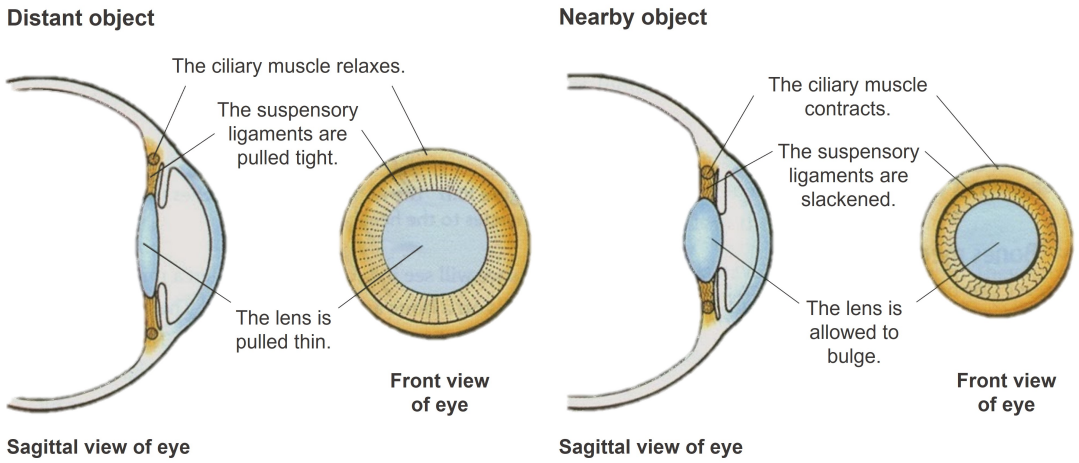

Figure 2.3: The accommodation mechanism according to Helmholtz's theory. (a) The eye focuses on a distant object, reaching a relaxed state. (b) The eye is accommodated and focused on a nearby object.[1]

index of the lens is not constant, being most uniform in the nucleus and denoting a greater variation in the cortex. When evaluating the varying refractive index values of the lens, Atchison et al. (2000) found a maximum index value of $n_l = 1.406$. However, "if the real lens with its gradient index is replaced by one with the same thickness, same radii of curvature and a uniform refractive index, this index must be made higher than the maximum index" (Atchison et al. (2000), p. 18). As such, the authors defined the lens equivalent refractive index as $n_l = 1.42$.

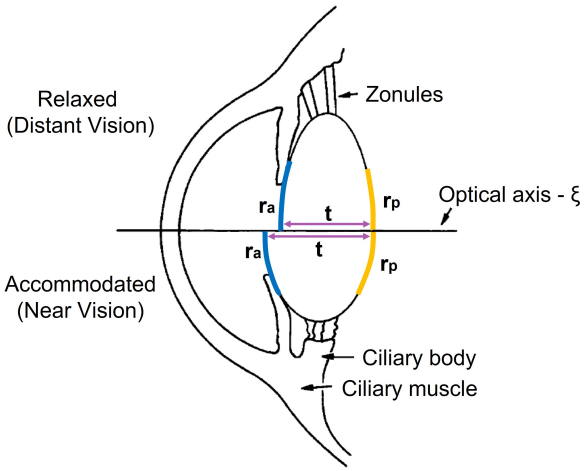

Figure 2.4: The lens in accommodated and relaxed states. Adapted from Atchison et al. (2000).

The amplitude of accommodation (ΔCOP) is calculated when one subtracts the dioptric power of the lens in its most relaxed state from the power of the fully accommodated state (Bocskai and Bojtár, 2013; Yavas et al., 2009) and is portrayed in Equation 2.2.

$$\Delta COP = COP_{accommodated} - COP_{relaxed} \tag{2.2}$$

[1]The original image was downloaded from `https://thebiolog.com/2020/03/25/myopia-and-hyperopia/` on 2021/05/20

This value reduces with age progression, since the aging eye loses its ability to accommodate, a characteristic of the presbyopia condition. The rate at which lenses from 20 to 60 years-old lose their accommodation capacity was estimated with use of Equation 2.3, provided by Ungerer (2000).

$$\Delta COP(age) = \exp\left(1.93 + 0.0401 \cdot age - 0.00119 \cdot (age)^2\right) \tag{2.3}$$

According to the exponential function, the lens reaches an amplitude of accommodation of $9.5D$ at 20 years-old and gradually looses this capacity, achieving $3.7D$ at 45 years and $1.0D$ at 60 years of age (Ungerer, 2000).

Moreover, Duane (1922) conducted a similar study, where the accommodation amplitude range was measured for each age, from 10 to 70 years-old. The results found by the author are of great use, since not only do they measure the accommodative capacity of the lens in a greater age range, but they also provide a minimum and maximum estimates of the accommodation amplitude for each age, given that there are individual variations between the studied lenses. The resulting values found for the accommodation capacity of the lenses, measured by Ungerer (2000) and Duane (1922) are depicted in Figure 2.5.

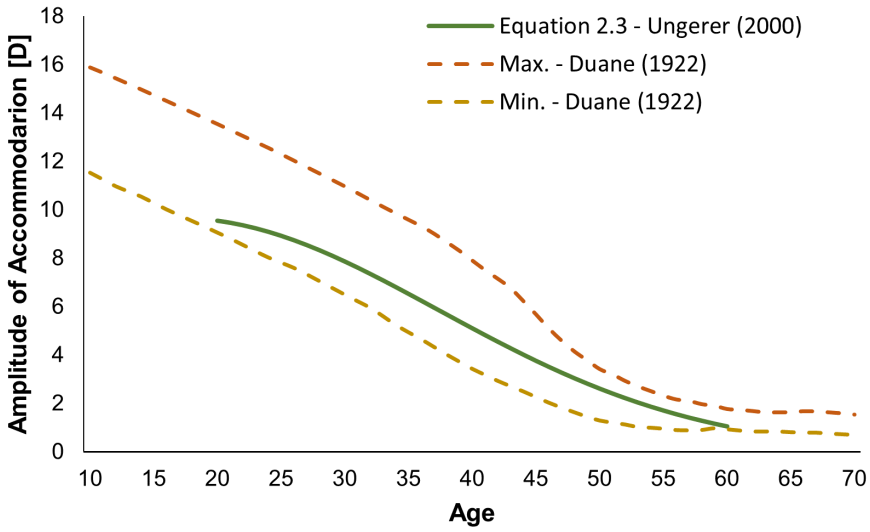

Figure 2.5: Amplitude of accommodation values found by Ungerer (2000) and Duane (1922).

Figure 2.5 shows that, even though the publication by Duane (1922) is older, the reported values by the author are comparable with more recent studies (Ungerer, 2000), having the advantages foremen-tioned. As such, these values are also taken into consideration in this work's context.

2.1.2 Pseudoexfoliation Syndrome

The subject of zonulopathy caused by the pseudoexfoliation syndrome is extremely relevant when surgeons evaluate the possibility of grave conditions such as *ectopia lentis*, or late in-the-bag dislocation, after cataract surgery. Nonetheless, its origin and mechanism lack understanding and essential experimental data (Schlötzer-Schrehardt and Naumann, 2006).

In the context of the human ocular structure, the pseudoexfoliation syndrome remains defined by the deposition of a white material in the eye's anterior segment, whose exact composition continues unknown to this day (Schlötzer-Schrehardt and Naumann, 2006).

Taking into account both the prevalence of this condition, which can affect up to 30% of the population older than 60 years-old, and the severe consequences that it can bring, its study becomes of utmost importance (Schlötzer-Schrehardt and Naumann, 2006).

The afflicted eye, in the presence of pseudoexfoliative conditions, denotes the deposition of extracellular fibrils that can be found both on the pupillary border and the anterior lens capsule (Ritch and Schlötzer-Schrehardt, 2001).

Resorting to transmission and scanning electron microscopy, Schlötzer-Schrehardt and Naumann (1994) ascertained that the sites of production of this substance, in concern to the lens complex, were the lenticular and ciliary proliferative regions i.e., locations where there is cell production. Consequently, the deposition of material bundles occurs in the ciliary processes and the pre-equatorial lens epithelium. These regions are also locations of zonular fiber insertion, leading to the deposition of the degenerative material in these fibers, having the consequence of zonular dialysis and weakness.

Accordingly, the authors found a disruption of the zonules in these anchorage regions and, in advanced cases, a complete abolition, due to the build-up of intercalating pseudoexfoliation clumps. This manifestation was observed in cases with lens subluxation, a severe consequence of pseudoexfoliation (Schlötzer-Schrehardt and Naumann, 1994).

When observing the proliferative region of the lens, the authors noted that the pseudoexfoliation clumps are produced by the lens epithelial cells. The effects of pseudoexfoliation syndrome in the capsule's morphology are not significant on either of its poles, which present the same thickness and elasticity as in control eyes. The same does not apply to the attachment region of the suspensory ligament. This area, when afflicted with pseudoexfoliation, suffers a severe disruption of the supporting zonules. The fibers are locally lifted off from the lens capsule and ultimately rupture, due to the outburst of degenerative material (Schlötzer-Schrehardt and Naumann, 1994).

In respect to these findings, the deposition of the material in the zonular fibers can be observed in an *in vitro* setting, where a macroscopic view of the pseudoexfoliative incrustation in the zonular fibers and ciliary processes can be observed in Figure 2.6a. A closer perspective is also depicted in Figure 2.6b, where the white bundles of fibrillar material can be observed, with the use of scanning electron microscopy. In this figure, the letter **Z** represents the zonular fibers that are located next to the lens equator (**L**).

The alterations caused by the syndrome were described as the mechanical loosening of the zonular insertion, where the disruption occurred in the attachment sites, rather than the fibers themselves (Schlötzer-Schrehardt and Naumann, 1994). Similarly, Naumann et al. (1998) described the underlying functioning of this mechanism with a proficient definition: "the zonular bundles are separated (...) by locally produced, intercalating pseudoexfoliation fibers acting like ice in the fissures of a rock and enlarging the separation" (Naumann et al. (1998), p. 955).

When examining the different sets of zonules, Schlötzer-Schrehardt and Naumann (1994) found that

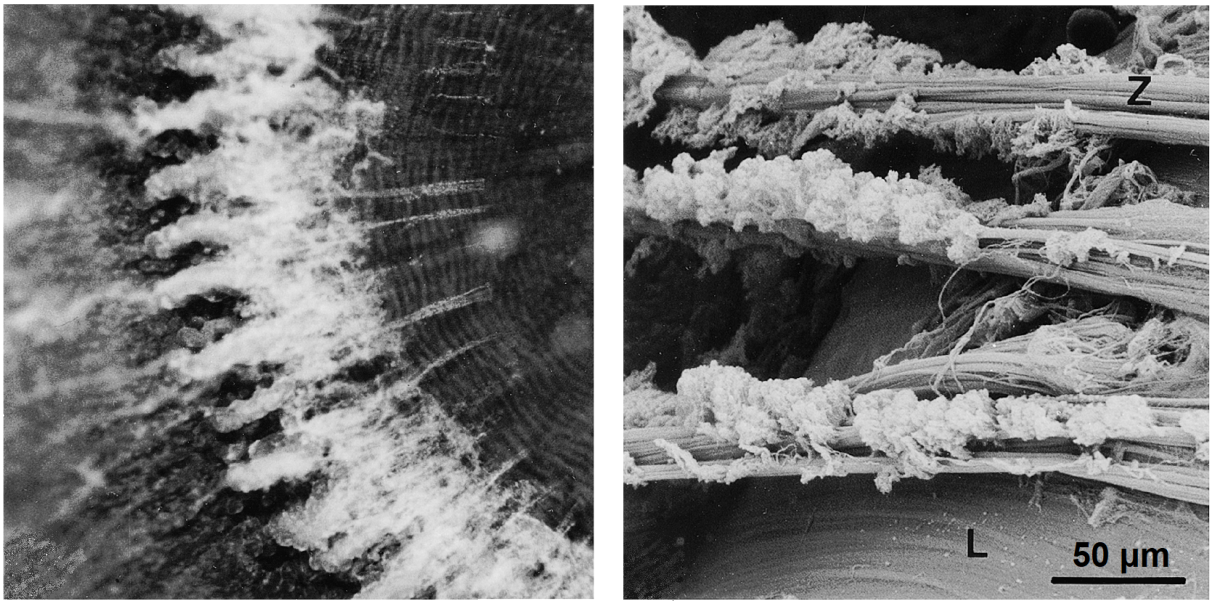

(a) (b)

Figure 2.6: Ocular structures denoting the presence of pseudoexfoliative material (adapted from Ritch and Schlötzer-Schrehardt (2001)). (a) Macroscopic view of ciliary processes and zonular fibers coated with pseudoexfoliative material. (b) Pseudoexfoliation material deposition in the zonular fibers.

the anterior zonular fibers were the ones with the most severe disinsertion and fragmentation, due to the heavy incrustation of pseudoexfoliative material. On the contrary, the posterior zonules presented a much smaller disruption, with small fragmentations throughout the bundle, but lack of complete zonular degeneration. Similarly, Wilson et al. (1987) observed that since part of the posterior zonules is firmly adherent to the anterior hyaloid (the membrane enclosing the vitreous), there was a smaller disruption of these fibers.

On the topic of the most affected zonular regions, Wilson et al. (1987) also studied the locations of zonular disruption from a frontal perspective. The authors found that, after cataract surgery, 4 of the 27 observed patients presented zonular disruption unrelated to the mentioned procedure. In particular, three of the patients presented zonular dialysis in the inferior region, whereas the remaining patient presented weakening of the suspensory ligaments in the superior region.

Recently, the zonular weakness was classified according to the term ”clock-hours”, which reflects the angle of zonulopathy, from a frontal perspective (Hoffman et al., 2013). Each clock-hour accounts for a 30 degree section. The authors described three levels of zonular dialysis extension, considering that the first level was defined by a dialysis extension from 0 to 3 contiguous clock-hours, that the second level of zonulopathy concerned a dialysis extension from 3 to 6 adjoining clock-hours and, finally, the third level accounted for dialysis cases with an extension of over 6 contiguous clock-hours of dialysis.

Yavas et al. (2009) studied the effect of pseudoexfoliation in the accommodative capacity of involved eyes. A total of 66 eyes was studied (37 with pseudoexfoliation, 29 control), with ages ranging from 40 to 60 years-old, and the accommodation amplitude was measured by means of infrared photorefraction. The authors reported that the accommodative capacity decreased significantly in patients with pseudoexfoliation, when compared to the control group.

The authors denoted a reduction of accommodative capacity for all the involved eyes, observing that for the older age group (50–60 years), the accommodation amplitude of healthy eyes was valued as $\Delta COP = 1.42 \pm 0.7D$ and the patients with pseudoexfoliation syndrome presented an accommodative capacity of only $\Delta COP = 1.10 \pm 0.6D$. Nonetheless, the severity of pseudoexfoliation for each of the involved eyes was not specified.

2.2 Finite Element Modeling

The main goal of computational modeling, when applied to the human lens complex, is the understanding of the optical and biomechanical behaviors of the lens throughout its deformation.

The finite element (FE) method proves to be a useful tool in the solution of mechanical problems that are too complex to be solved analytically, and is often the only pathway to obtain quantitative information about forces and material properties of the involved structures, when there is a lack of attainable experimental data (Lanchares et al., 2012).

Computational models, namely the finite element ones, related to the human lens complex, regularly comprise the modeling of the zonular fibers, the capsular bag and the crystalline lens. This last component is often divided in two structures: the cortex and nucleus (Wang et al., 2019).

Burd et al. (1999) developed the first model of the human lens complex with the aim of understanding its biomechanical behavior. The study's objective was the assessment of different theories of accommodation, finding that the Helmholtz accommodation theory was the one that best fitted younger lenses. The authors were brought to this conclusion while also highlighting the need for the use of nonlinear geometrical behavior formulations when modeling the lens deformation.

From then on, most studies assumed that the reference configuration of the lens is in a fully accommodated, stress-free state, with the resulting zonular force being negligible, and being then elongated by means of the zonular fibers in order to reach its unaccommodated state, in accordance with Helmholtz's theory of accommodation.

The authors later published another article, where the age-related changes in the accommodative capability of the lens were explored (Burd et al., 2002). For axisymmetric models of lenses aged 11, 29 and 45 years-old, the authors found that the 45 year lens was less accommodating ($\Delta COP = 2.29D$) than the 29 year one ($\Delta COP = 6.92D$). For the 11 year lens, the authors reported an anomalous accommodative result ($\Delta COP = 4.66D$), with the underlying factor being a possible underestimation of the range of *in vivo* zonular displacement data. This displacement was defined by Strenk et al. (1999), taking into account Equation 2.4.

$$\delta_Z = 0.5129 - 0.00525 \cdot age \tag{2.4}$$

Bearing in mind this expression, the displacement of the 11, 29 and 45 year-old lenses were defined as $\delta_Z = 0.455mm$, $\delta_Z = 0.361mm$ and $\delta_Z = 0.277mm$, respectively.

The model depicted by Burd et al. (2002) can be observed in Figure 2.7a, where the three zonular

sets connect to the ciliary muscle in a single insertion site (*point C*). Additionally, the displacement of the fibers, δ_Z, was performed in the radial direction of the ciliary muscle, which corresponded with the equatorial zonule radial direction. Furthermore, Figure 2.7b shows the lens before and after disaccommodation, with the latter state being represented in the meshed configuration.

As mentioned, the 45 year lens displacement of the zonular fibers was defined as $\delta_z = 0.277mm$, resulting in a total zonular force of $F_Z = 80.0mN$, after deformation. The resulting values found for the amplitude of accommodation, lens thickness and radius variations, and total zonular force of this model are depicted in Tables 2.1 and 2.2.

The authors reflected on the possibility of the material behavior of the lens complex components being anisotropic. However, all materials were considered as linear isotropic, due to the insufficient clinical data backing up anisotropy properties of said structures. Both the capsular bag and three sets of zonular fibers were modeled with membrane elements.

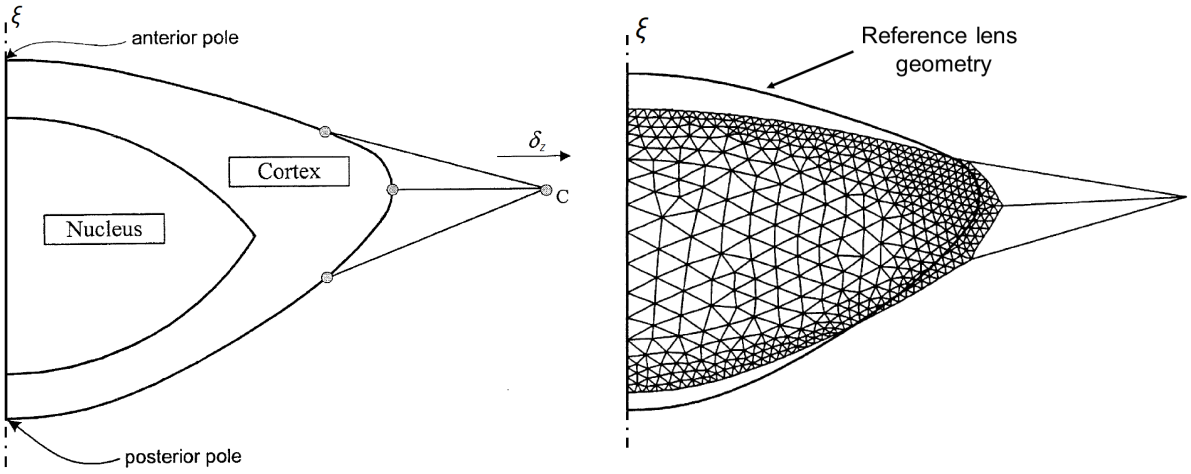

(a) (b)

Figure 2.7: Axisymmetric model designed by Burd et al. (2002). (a) Reference lens geometry. (b) Accommodated and relaxed states of the 29-year lens. Images adapted from Burd et al. (2002).

Following Burd et al.'s work, several models were developed, where the material properties of each structure, the zonular fiber modeling, and geometry of the lens were diverse. In regards to the zonular fiber modeling, the lack of available clinical data rendered this process quite more difficult than for other components of the lens complex (Wang and Pierscionek, 2019). As such, the modeling of the zonules differs significantly throughout the literature presented.

When approaching this problem, Hermans et al. (2006, 2008) disregarded the zonular structures and the ciliary muscle movement. Consequently, the authors defined regions of attachment in the capsular bag and acted a set of uniformly distributed zonular forces on these regions, with the goal of elongating the lens into its disaccommodated state. In order to understand the role of the zonular action in the accommodation process, different force angle and magnitude configurations were tested, in order to obtain optimal solutions that best fit the disaccommodated geometry of the lens.

When considering the three anchorage regions in the capsule (anterior, equatorial and posterior), Hermans et al. (2006) estimated the external zonular force acting on the 29 year-old lens, $F_Z = 81.0mN$,

for an amplitude of accommodation of $\Delta COP = 8.00D$. The authors also analyzed the Von-Mises stress endured by the cortex and nucleus (VM_{C+N}) of said model and found that it ranged from $0.035kPa$ to $0.523kPa$, being of greater magnitude in the cortical regions with proximity to the capsule belts and lower in the nuclear section of the lens.

With the goal of quantifying the age-related changes in the zonular force acted on the lens, Hermans et al. (2008) studied lenses of 11, 29 and 45 years-old, similarly to Burd et al. (2002). The authors performed several simulations with different material properties, coming to the conclusion that the force on the lens presented an increase in the 29 and 45 year lenses ($F_Z = 56.0mN$), when compared to the 11 year one ($F_Z = 41.0mN$). This value was, however, significantly lower than the one presented by the authors two years prior. This contrast in results can be related to the use of different material properties both in the cortex and nucleus of the lens, as reported in Annex A, Table A.1. Using the linear isotropic material properties obtained by Heys et al. (2004), Hermans et al. (2008) found that the 45 year-old lens had an accommodative capacity of 4.00 dioptres, and that the lenticular radius increased $\Delta R_L = 5.20\%$ after disaccommodation.

Belaidi and Pierscionek (2007) created a three-dimensional model representing a quarter of the human lens and applied ciliary forces of different magnitudes in order to impose the deformation of the lens. The capsule was modeled as a shell-like structure, and the contact between the lens and capsule was assumed to be frictionless. The zonular fibers were modeled as beam elements, with the interior end connected to the capsule and the external one attached to an analytical point (simulating the ciliary muscle insertion location), where the forces were applied, as represented in Figure 2.8. The acting force, f_Z, depicted in Figure 2.8 accounts for the force applied in 5 zonular beams anchored to the capsular bag, in the sagittal plane of the lens. The modeled 46 year-old lens, when subjected to a total zonular force of $F_Z = 100mN$, presented Von-Mises stress values ranging from $0.060kPa$ to $0.657kPa$.

These results were obtained when defining different Young's moduli to the cortex ($E_C = 4kPa$) and nucleus ($E_N = 1kPa$). Nonetheless, the authors noted that having a greater elastic modulus for the cortex than the nucleus was conflicting with studies that found a higher protein density in the nuclear region of the lens (Belaidi and Pierscionek, 2007).

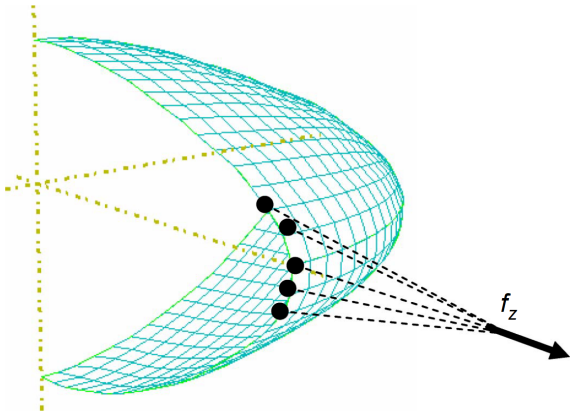

Figure 2.8: Capsular bag mesh with f_Z representing the zonular force acted in the sagittal plane of the lens (adapted from Belaidi and Pierscionek (2007)).

Weeber and Van Der Heijde (2008) assumed that the disaccommodated state of the lens would be reached with an equatorial lens stretching magnitude of $\Delta R_L = 7.00\%$, provided by the radial stretching of the outer edge of the zonules. Taking that into account, the 60 year-old modeled lens had an accommodation amplitude of 0.20 dioptres. When obtaining the change in lens dioptric power, the authors resorted to Equation 2.1, by fitting spheres over the central $3mm$ radial amplitude of the anterior and posterior surfaces of the lens.

The authors represented all the components with linear elastic isotropic material properties, although introducing a gradient stiffness in the lens that decreased gradually from the central region ($E_{L_{int}} = 108.54kPa$) to its periphery ($E_{L_{ext}} = 6.25kPa$). Within each marked region (10 total), the stiffness was constant. The zonular depiction of Weeber and Van Der Heijde's model had both the anterior and posterior zonules attaching to the ciliary muscle in a single insertion point. Nonetheless, the equatorial zonular fibers attached to the midpoint of the posterior zonular set instead of the ciliary muscle, as previously described in other publications.

Following work studied the lens deformation in a 3D simulation that comprised the complete lenticular and capsular structures (Lanchares et al., 2012). When approaching the zonular depiction in the models, Lanchares et al. (2012) implemented the same methodology as Hermans et al. (2006, 2008), by acting uniformly distributed forces in the anchorage bands of the capsule. The representation of the capsule bands can be observed in Figure 2.9, as well as their width and location in accordance to the lens equator ($y_{ant} = 1.04mm, y_{post} = 1.29mm$).

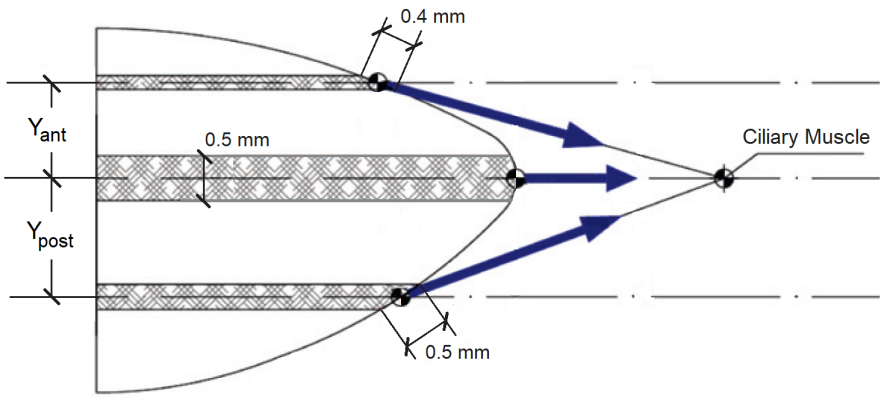

Figure 2.9: Configuration of the band regions of the capsular bag developed by Lanchares and co-authors. Adapted from Lanchares et al. (2012).

Taking a 30 year-old lens as a base model, the authors determined the zonular forces imposed on the capsule that would have the best correspondence with the relaxed geometry of the lens. The resulting zonular force found for the lens was valued $F_Z = 78mN$, and the capsule's strain and stress distributions were studied, along with the principal stress endured by the cortical and nuclear components of the lens. The outcomes found by this work are portrayed in Tables 2.1 and 2.2.

Similarly to previous studies, Lanchares et al. (2012) varied the capsule's thickness. The depiction of the capsular thickness provided by the authors presented a greater magnitude in the equator

($T_{CB} = 20\mu m$), and smaller in the anterior and posterior poles ($T_{CB} = 10.87\mu m$ and $T_{CB} = 3.16\mu m$, respectively).

When analysing the accommodation process of the lens, Bocskai and Bojtár (2013) portrayed not only the lens complex depicted in previous works, but also the sclera, ciliary muscle and cornea of the human eye. In order to simulate the support of these structures, the surrounding fatty tissue was modeled as well, leading to a complex finite element model. The authors defined the zonular fibers and lens capsule with shell elements, and the materials of the lens complex were all modeled with linear isotropic properties.

The other variable introduced to their study was the change of the refractive index of the lens with age. The authors highlighted that, while studying the age-related changes of the lens, not only the material properties and geometric parameters of the lens have a great importance, but also the lens optical properties need to be taken into account. The authors found that when varying both the material properties and refractive index of the lens with age-related trends, the 60 year-old lens had an amplitude of accommodation of $\Delta COP = 1.64D$.

Bahrami et al. (2016) represented the zonules as a single surface in order to attain global anchorage regions both to the capsule and the ciliary processes, and enforced a displacement $\delta_Z = 0.1mm$ in the radial direction of the ciliary body. The authors implemented a varying cortical stiffness, with smaller magnitude in the center of the lens ($E_{C_{int}} = E_N = 0.6kPa$), which then increased up to the outer surface of the lens to a value of $E_{C_{ext}} = 3.0kPa$. The resulting accommodation amplitude of the 27 year-old lens was $\Delta COP = 10D$.

Wang et al. (2016) studied the influence of the use of different material properties in the crystalline lens while also testing different forms of zonular stretching angles and forces, in order to obtain the one that would best portray the physiological behavior of the humans lens.

The capsule was modeled with shell elements and the cortex and nucleus as solid components. The zonular fibers only had the capability of being uniaxially loaded. The authors found that, when portraying the zonular fibers with different stretching directions i.e, having more than one insertion point in the ciliary muscle, this form presented a better correspondence with the physiological behavior of the living lens.

When analysing the varying cortical stiffness of the lens, similarly to Bahrami et al. (2016), Wang et al. (2019) reached the conclusion that this factor had no influence in the resulting amplitude of accommodation, when compared with lenses with constant cortical stiffness.

Later on, the same investigation group evaluated the impact of each of the zonular sets in the accommodation process, as well as the influence caused by different assignments in capsular bag thickness (Wang et al., 2017).

The authors designed models of 16 and 35 year-old lenses, and found that for the older lenticular structures, there was no significant difference in the biomechanical behavior between uniform and varying capsular thicknesses. In addition, the authors provided novel data concerning the Central Optical Power (COP) evolution of the lens, throughout its deformation. By doing so, Wang et al. (2017) divided the simulation in six equal stretching steps, with the objective of understanding the trend of the anterior

and posterior radii of curvature, being then able to calculate the COP quantity for the same steps. The authors noted that for the 35 year-old lens, the Central Optical Power showed an increase in the first sixth of the deformation, and a reduction throughout the rest of the disaccommodation process.

The first work developed at Instituto Superior Técnico (Cardoso, 2018) comprehended an axisymmetric model of the human lens before and after cataract surgery. In pre-surgical conditions, the lens presented thickness and radius variations of $\Delta T_L = 6.90\%$ and $\Delta R_L = 8.10\%$, respectively. The total zonular force for the modeled lens was valued as $F_Z = 71.0mN$.

Recently, Wang et al. (2019) published yet another article, showcasing the finite element modeling of lenses aged from 16 to 62 years-old, in order to understand how the lens complex system changes with its aging. The authors defined each of the three sets of zonular fibers as structures measuring $l_Z = 1.5mm$ in length and $T_Z = 50\mu m$ in thickness.

Similarly to their previous study conducted in 2017, Wang et al. (2019) obtained values for the progression of Central Optical Power values throughout six equal increments of the simulation process and, for the case of 62 year old lens, obtained the same trend in COP slope, with an increase of 1.2 dioptres in the first stretching step and a consequent decrease throughout the rest of the deformation of the lens. Hence, the resulting amplitude of accommodation of the 62 year-old lens was valued as $\Delta COP = 1.94D$.

In this study, the group obtained the greatest value of lens thickness variation ($\Delta T_L = 15.80\%$), which is worth mentioning, considering that the value concerns an older lens. Nonetheless, this value seems unrelated to the accommodative capacity of the lens, since this former quantity is in accordance with the accommodation age-related trends shown in Figure 2.5.

A more recent work developed at Instituto Superior Técnico (Paulino, 2019) introduced an innovative perspective into the constitutive properties of the zonular structures of the lens complex. Accordingly, the developed work achieved a description of the zonular fibers with hyperelastic anisotropic properties, as a consequence of a thorough optimization and ensuing validation with available literature data. Bearing this in mind, the biomechanical behavior of the modeled 29 year-old healthy lens under these circumstances was analogous to results found by other authors, where the resulting zonular force was valued as $F_Z = 94.5mN$, and the lens geometry variation was measured both in the radial ($\Delta R_L = 6.60\%$) and thickness-related ($\Delta T_L = 10.75\%$) parameters.

Tables 2.1 and 2.2 present a summarized overview of the results obtained throughout the literature data analyzed in this section. In the first table, the radial (ΔR_L) and thickness (ΔT_L) variation parameters found for the lens disaccommodated state are depicted, as well as the resulting accommodation amplitude of the lens (ΔCOP).

The literature data related to the accommodation amplitude (ΔCOP) values presented in this table depict a trend that is closely related to the presbyopia condition, being that as the lens age progresses there is an overall reduction of the accommodative capacity found for each lens. The values found by Hermans et al. (2008) and Weeber and Van Der Heijde (2008) denote small deviations from the rest of the values presented, but that can be explained with the fact that due to the small amount of available data, each author provides different methodologies for their model construction.

	Age	$\Delta COP[D]$	$\Delta T_L[\%]$	$\Delta R_L[\%]$
Cardoso (2018)			6.90	8.10
Bahrami et al. (2016)	27	10.00	9.91	
Hermans et al. (2006)	29	8.00		7.04
Paulino (2019)	29		10.75	6.60
Lanchares et al. (2012)	30	7.50	10.90	6.60
Wang et al. (2017)	35	3.01		
Burd et al. (2002)	45	2.29		7.60
Hermans et al. (2008)	45	4.10		5.20
Weeber and Van Der Heijde (2008)	60	0.20		7.00
Bocskai and Bojtár (2013)	60	1.64	9.92	
Wang et al. (2019)	62	1.94	15.80	

Table 2.1: Literature data for the lens geometry variation and accommodation amplitude.

	Age	Zonules F_Z [mN]	Capsular Bag LE_{CB}	Capsular Bag S_{CB} [kPa]	Cortex + Nucleus S_{C+N} [kPa]	Cortex + Nucleus VM_{C+N} [kPa]
Cardoso (2018)		71.0		53.0 - 160.0		
Hermans et al. (2006)	29	81.0				0.035 - 0.523
Paulino (2019)	29	94.5	3.01E-2 - 6.65E-2	70.3 - 123.5		
Lanchares et al. (2012)	30	78.0	4.19E-2 - 7.03E-2	82,8 - 160.3	-0,247 - 0.526	
Hermans et al. (2008)	45	56.0				
Burd et al. (2002)	45	80.0				
Belaidi and Pierscionek (2007)	46	100.0				0.060 - 0.657
Wang et al. (2016)	48	80.0				0.043 - 0.438
Wang et al. (2019)	62					0.041 - 0.204

Table 2.2: Literature data for zonular force, strain and stress endured by the capsule and stress measurements of the nucleus and cortex.

Table 2.2 illustrates the resulting force acted on the zonules (F_Z), as well as the logarithmic strain (LE_{CB}) and principal stress (S_{CB}) endured by the lens capsule. Finally, the ranges of principal (S_{C+N}) and Von-Mises (VM_{C+N}) stress in the cortical and nuclear regions are reported in the same table.

The material properties defined for each of the models portrayed in Tables 2.1 and 2.2 are depicted in Appendix A, Table A.1.

Chapter 3

Materials and Methods

In this chapter, the methodologies practiced throughout the construction and design of the computational models of the present work are described. Additionally, the procedures implemented in the result analysis process are characterized, leading to a full disclosure of the experimental work developed throughout this dissertation.

3.1 Healthy Lens Complex

With the objective of studying the human lens complex at an age where there would be a significant prevalence of the pseudoexfoliation syndrome, the healthy modeled lens had an age of 62 years-old. Accordingly, the geometry, material properties and boundary conditions are pertinent to this configuration, allowing for a correct description of the designed models. The deformation of the lens was modeled with nonlinear geometrical behavior formulations, similarly to the approach by Burd et al. (1999).

3.1.1 Geometry and Mesh

The geometry of the 62 year-old lens was based on the study conducted by Pierscionek et al. (2015), where the lens geometry was extracted from Figure 3.1, that represents the iso-indicial contours of the refractive index of the lenticular structure.

The outer shape of the cortex was designed taking as a baseline the minimum value of the refractive index contour. The outline of the nucleus was constructed taking into account the second most inner isoline of the refractive index. Consequently, the obtained cortical and nuclear partial profiles of the lens are portrayed in orange, in Figure 3.1.

The total thickness of the lens, measured in the optical axis, was valued as $T_L = 4.67mm$. The lens radius was measured in the equatorial plane of the lens i.e., where the lens radius has a broader dimension. The radius value was then defined as $R_L = 4.41mm$. According to Figure 3.1, the values found for the nuclear thickness and radius were $T_N = 2.66mm$ and $R_N = 2.56mm$, respectively.

Due to the irregular nature of the nuclear-defining isoline, the correct geometrical representation of the nucleus also took into consideration the analysis performed by Wang et al. (2019) to the data

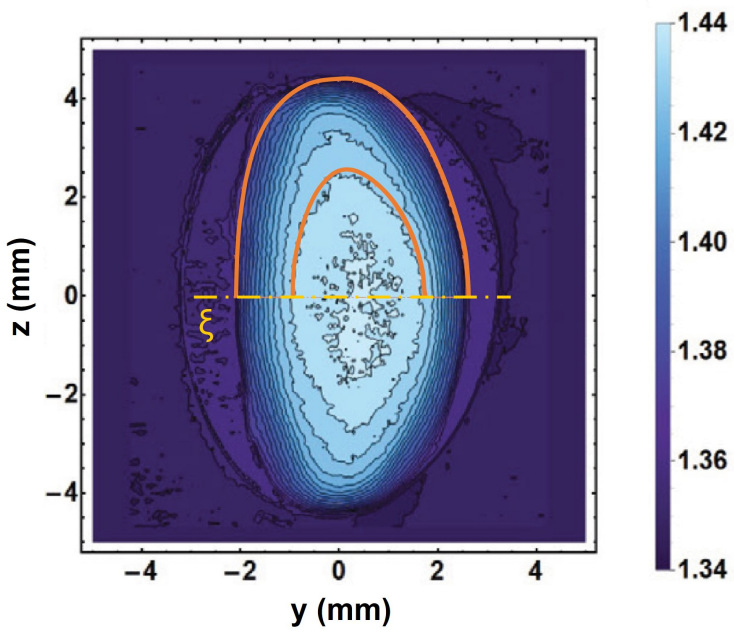

Figure 3.1: Contours of the refractive index and geometrical parameters defined for the lenticular components of the 62 year-old lens.

provided by Pierscionek et al. (2015). In this evaluation, the proportion between lenticular and nuclear thicknesses was assessed for each lens, as well as the relation between nucleus and lens radii.

With the scattered data provided, Wang et al. (2019) obtained the relationship between the lens thickness (T_L) and nuclear thickness (T_N) with age dependence, which is given by Equation 3.1.

$$\frac{T_N}{T_L} = 0.0013 \cdot age + 0.4525 \tag{3.1}$$

The authors also provided an expression that depicts the proportion between nuclear and lenticular radii (R_N and R_L). This relationship, also age-related, lead to Equation 3.2.

$$\frac{R_N}{R_L} = 0.0029 \cdot age + 0.3307 \tag{3.2}$$

Figure 3.2 displays Equations 3.1 and 3.2 as well as the results found for the proportions of the geometry developed in Figure 3.1, where the proportion found between the thicknesses of nucleus and lens is given by $\frac{T_N}{T_L} = 0.57$, and the ratio of nuclear and lenticular radii is given by $\frac{R_N}{R_L} = 0.58$. Taking the findings of Figure 3.2 into account, where there is a close proximity between age-dependent ratios of Wang et al. (2019) and the present work's scaling ratios, the dimensions found for the nucleus were verified.

In order to obtain the resulting geometry of the lens, the profile defined in Figure 3.1 determined the outer surfaces of both the nucleus and cortex, which were then used to create axisymmetric structures, recurring to the axis of revolution, represented in said figure by the optical axis, ξ.

Using the same methodology, the capsule of the lens was defined taking into account the outer defining edge of the lens, leading to the generation of the membrane that encloses the crystalline.

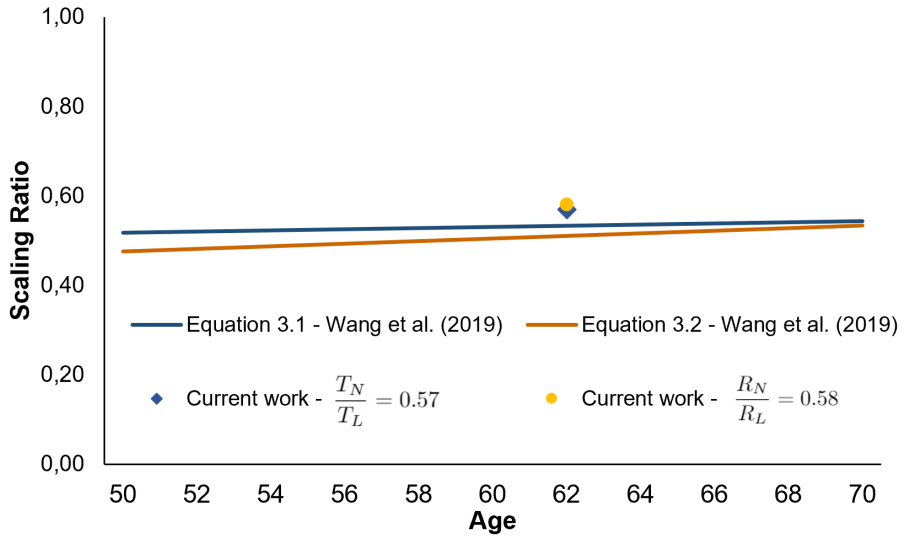

Figure 3.2: Age-related scaling ratios between lenticular and nuclear dimensions.

The design of the structures was rendered recurring to SolidWorks®(Dassault Systèmes, France) and the resulting geometry of the lens complex is depicted in Figure 3.3, where both the three-dimensional and two-dimensional (2D) views of the lens complex are illustrated. The nuclear component of the lens is represented in orange, the cortex in the purple region and the three sets of zonules are colored in blue. The capsular bag is depicted in a checkered grey pattern in the 3D illustration of the model, and in a dark grey line for the case of the 2D view.

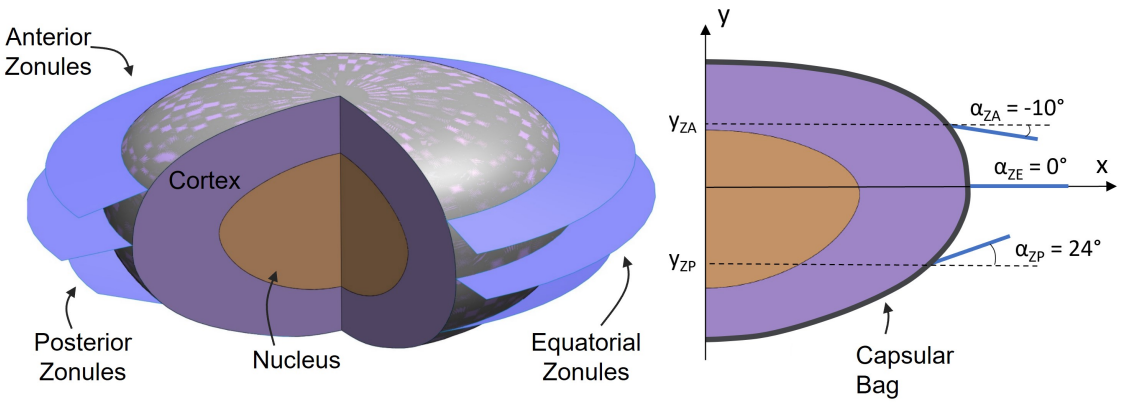

Figure 3.3: Geometry of the 62 year-old lens complex, sectioned 3D and axisymmetric views.

When defining the configuration of the zonular fibers geometry, the findings by Wang et al. (2019) were taken into consideration. Accordingly, the anterior (ZA), equatorial (ZE) and posterior (ZP) sets of zonular fibers were defined with the same zonular length, $l_Z = 1.5mm$. The capsule's insertion locations of the zonular fibers were based on data provided by Lanchares et al. (2012). By using parallel planes to the equatorial plane ($y_{ZE} = 0mm$), the authors assigned the anterior and posterior y-coordinates of zonular insertion as $y_{ZA} = 1.04mm$, and $y_{ZP} = -1.29mm$, respectively.

The defining angles of the zonular sets were the following: the anterior zonules had an angle value of $\alpha_{ZA} = -10deg$; the equatorial fibers had $\alpha_{ZE} = 0deg$; and finally, the posterior zonules angle was

Component	Element type	Element number	Node number
Capsular bag	S3	14760	7382
Cortex	C3D4	193744	36067
Nucleus	C3D4	43403	8395
Anterior zonules	M3D3	3132	1740
Equatorial zonules	M3D3	2842	1589
posterior zonules	M3D3	2916	1620
Total		260797	56793

Table 3.1: Type of elements, element number and node number for the designed model.

$\alpha_{ZP} = 24deg$. As reported by Wang et al. (2019), this combination of zonular angles led to the maximum values for the amplitude of accommodation, among other angle assortments that the authors tested.

Taking these factors into account, the modeled zonules attach to the ciliary muscle in three different insertion points. The three sets were defined with the same thickness value ($T_Z = 10\mu m$), based on findings from Van Alphen and Graebel (1991). The capsule's thickness was defined with a dimension of $T_{CB} = 20\mu m$, uniformly defined throughout its structure, equivalently to the approach employed by Wang et al. (2019).

The mesh construction of each of the constituents of the lens complex was performed using Abaqus ® (Dassault Systèmes, France). The nucleus and cortex were both represented with 4-node linear tetrahedrical elements, C3D4. The three zonular sets were modeled with 3-node triangular membrane elements, M3D3, whereas the capsule was modeled with 3-node triangular shell elements, S3. The number of elements and nodes for each of the components of the lens complex are depicted in Table 3.1. The mesh representation of the model is depicted in Figures 3.4a and 3.4b, where the frontal and sagittal views of the lens complex can be observed.

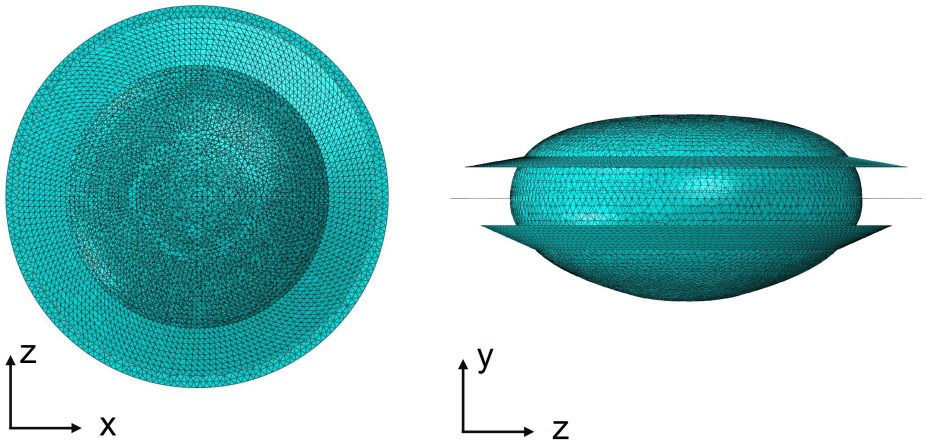

(a) (b)

Figure 3.4: Designed mesh for the lens complex. (a) Frontal view. (b) Sagittal view.

3.1.2 Constitutive Modeling

The cortex and nucleus of the lens were modeled with linear elastic isotropic properties. Besner et al. (2016) performed a recent study on lenses aged from 19 to 63 years and found that for healthy lenticular conditions, the material properties had a negligible age dependence. The authors provided data related to the longitudinal modulus of the lens, M. In the finite element study of Wang et al. (2019), the authors corresponded the longitudinal modulus values M found by Besner et al. (2016) with linear isotropic properties of the nucleus and cortex.

The authors resorted to the longitudinal modulus profiles obtained by Besner et al. (2016), and determined the average values of cortical and nuclear longitudinal moduli, $M_C = 2.471GPa$ and $M_N = 3.286GPa$. Resorting to Equation 3.3, the authors defined an empirical relationship between the longitudinal modulus, and the Young's modulus of both the nuclear and cortical regions of the lens.

$$\log M = a \cdot \log G + b \tag{3.3}$$

Where $a = 0.093$ and $b = 9.29$ are material dependent coefficients that were determined for porcine lenses, and G stands for the shear modulus of the lens components. Given that the eye lens is considered as a quasi-incompressible structure, a linear relationship between the Young's modulus and shear modulus can be obtained, $E = 3G$.

As a result, Wang et al. (2019) obtained the Young's moduli of the crystalline's nuclear and cortical components: $E_N = 0.82kPa$ and $E_C = 0.04kPa$. These values were assigned as the Young's moduli of the present work, as well as the assigned Poisson coefficients, that were the same for the two lenticular sections ($\nu_C = \nu_N = 0.47$).

The capsule was modeled with linear isotropic properties, similarly to the components of the lens. Young's modulus and Poisson coefficient values were defined as $E_{CB} = 1.5MPa$ and $\nu_{CB} = 0.47$, similarly to the approaches taken by previous publications (Weeber and Van Der Heijde, 2008; Wang et al., 2019).

Structure	Constitutive Properties	Parameters
Cortex	Linear Elastic Isotropic	$E_C = 0.04kPa$ $\nu_C = 0.47$
Nucleus	Linear Elastic Isotropic	$E_N = 0.82kPa$ $\nu_N = 0.47$
Capsule	Linear Elastic Isotropic	$E_{CB} = 1.5MPa$ $\nu_{CB} = 0.47$
Zonular Fibers	Hyperelastic Anisotropic	$C_{10} = 0.0583$ $D_1 = 1.0286$ $k_1 = 0.87MPa$ $k_2 = 21.75$ $kappa = 0.3$

Table 3.2: Material properties defined for the lens complex components of the present work.

Equivalently to the findings from Paulino (2019), the zonular fibers are represented with hyperelastic anisotropic properties. Accordingly, the hyperelastic anisotropic constitutive properties were based on

the Holzapfel-Gasser-Ogden model (Holzapfel et al., 2000), given that this model is applicable to work concerning circumferential systems (Castro and Alves, 2020). When representing the material properties concerning the zonular fibers in Abaqus, the provided coefficients are defined in Table 3.2, as well as the parameters that define the material properties of the remaining components of the lens complex.

3.1.3 Boundary and Interaction Conditions

In order to ensure that there was no relative movement between the internal surface of the capsular bag and the external surface of the cortex, a tie constraint was applied between the two faces. In addition, the same type of constraint was applied to the nuclear external surface and the cortical internal face. By doing so, the forementioned regions were fused, allowing for a collective movement of the designated components, due to the binding of the displacement and rotation degrees of freedom of the surfaces, during the deformation of the lens.

The tie constraint was also applied in the three insertion rings of the capsular bag, corresponding to the three sets of zonules: the interior edge of the zonular set was defined as the slave surface, and the capsular ring the master surface, guaranteeing a cohesive movement of the capsule upon stretching of the zonules. In order to ensure that the capsule's master nodes were located in the same y-coordinates as the nodes of the interior edges of the zonules, the capsular bag's membrane was partitioned in $y = 0mm$, $y = -1.04mm$ and $y = -1.29mm$ for the corresponding cases of the equatorial, anterior and posterior fiber anchorages.

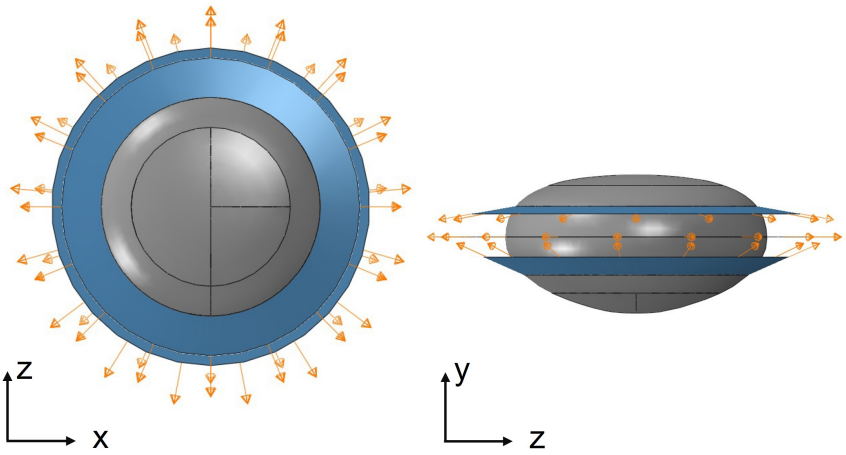

(a) (b)

Figure 3.5: Displacement of the zonular fibers during the disaccommodation process. (a) Frontal view. (b) Sagittal view.

With the objective of restraining the movement of the lens in all directions except the one of the optical axis, that corresponds to the y-axis represented in Figure 3.5b, the most anterior and posterior nodes of the cortex and nucleus were constrained, allowed to move only in the y direction. This approach is similar to the one taken by Lanchares et al. (2012), that restrained all the nodes of these components along the optical axis, and only allowed movement in the y direction.

When considering the zonular fibers, these were also restrained, and only allowed to partake movement in their corresponding radial orientation, in order to best simulate the stretching movement of the individual fibers, which is done in the radial direction of the zonular sets.

The displacement applied to disaccommodate the lens was done in the external edge of each zonular set and in the radial orientation of the set, as can be observed in Figures 3.5a and 3.5b. The magnitude of the radial displacement was the same for the three zonular sets and valued $\delta_Z = 0.5mm$, representing the movement amplitude enforced by the ciliary muscle (Wang et al., 2017). Similarly to the approach taken by Wang et al. (2019), this displacement was introduced in six even increments, favoring the evaluation of the lens deformation throughout the disaccommodation process.

3.2 Geometry of the Zonular Fibers

The present section aims to understand the influence of the frontal geometry variation of the zonular fibers, since the zonules were described as having an ellipsoid shape (Amigó and Bonaque-González, 2016). Due to the delimitation of the zonules by both the crystalline lens and the ciliary muscle, the measurements of these structures were taken into consideration.

Biermann et al. (2011) conducted an *in vivo* study, with the purpose of measuring the ciliary distance in four axes (0 degrees, $\pm$ 90 degrees and 180 degrees). The authors determined that the ciliary structure is vertically oval in 35 of the 37 examined eyes. For emmetropic eyes, the vertical measurement can be up to 5.6% higher than the horizontal one.

The crystalline lens measurements were also evaluated *in vivo*, where the lenticular vertical and horizontal diameters were compared. The results found by Khng and Osher (2008) revealed that the lens diameters were almost equal in the horizontal and vertical diameters (difference of 0.2%), leading to the outcome that the lens is an axisymmetric structure.

These results led to the deduction that the zonular fibers aligned in the vertical direction are longer than the ones aligned in the horizontal one, for an axisymmetric lens, given that they provide the connection between the ciliary structure and the lens.

In order to evaluate the clinical data presented, a study was conducted to analyze the variation of the frontal oval geometry of the zonular fibers.

Having the initial model as a starting point, where the frontal geometry of the zonular fibers is circular ($l_{Z_V} = l_{Z_H} = 1.5mm$), several models were assembled.

The designed models that comprehended a variation of the horizontal zonular length, had a constant value for the vertical zonular length ($l_{Z_V} = 1.5mm$). Model *Oval-5.6* had fibers that were 5.6% smaller in the horizontal direction than the vertical one ($l_{Z_H} = 1.416mm$) and model *Oval-2.8* represented fibers 2.8% shorter in the horizontal direction than the vertical one $l_{Z_H} = 1.458mm$.

For models with vertical zonular length variation, the horizontal zonular length remained constant ($l_{Z_H} = 1.5mm$). The first developed model, *Oval+2.8*, embodied zonules that were 2.8% longer in the vertical direction, as opposed to the horizontal one ($l_{Z_V} = 1.542mm$). On a similar note, model *Oval+5.6* depicted zonules that were 5.6% greater in the vertical direction than the horizontal one ($l_{Z_V} = 1.584mm$).

The corresponding zonular lengths of the designed models are depicted in Table 3.3.

Models with a constant vertical length $l_{Z_V} = 1.5mm$ and a smaller horizontal one are represented in Figure 3.6 (left). The dashdotted red line identifies the model with the horizontal length 5.6% smaller than the vertical one, *Oval-5.6*, and the short-dashed blue line displays the model with a 2.8% difference between the constant vertical dimension and the smaller horizontal one, *Oval-2.8*.

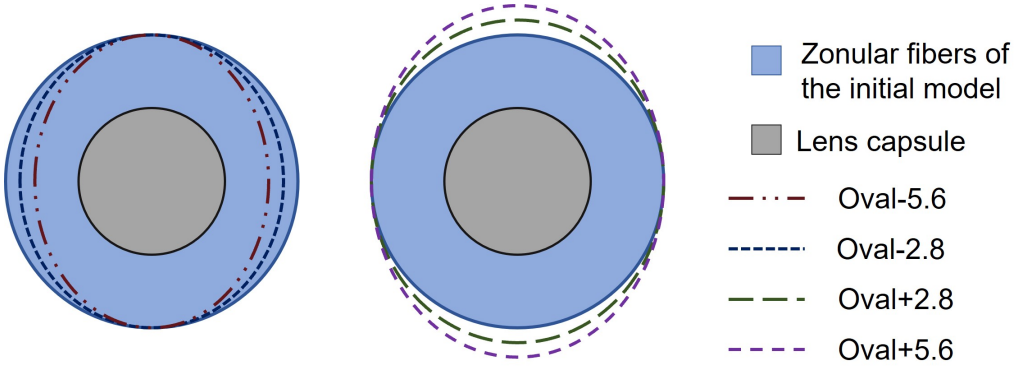

Figure 3.6: Frontal view schematic of the models with an oval zonular geometry.

Models with a constant horizontal length ($l_{Z_H} = 1.5mm$) and greater vertical length are represented in Figure 3.6 (center), with the long-dashed green line portraying the model where the vertical length of the zonular fibers is 2.8% greater than the horizontal one, and the dashed purple line portraying the situation where l_{Z_V} is 5.6% greater than the horizontal length of the zonules.

Note that the evolution of the models in Table 3.3 also denotes both an increase in the overall area occupied by the zonular fibers and their average length ($\overline{l_Z}$). Figure 3.6 shows the zonular area of the initial model, represented in light blue.

Model	Vertical length $l_{Z_V}[mm]$	Horizontal length $l_{Z_H}[mm]$	Line type (shown in Figure 3.6)
Oval-5.6	1.500	1.416	
Oval-2.8	1.500	1.458	
Initial Model	1.500	1.500	
Oval+2.8	1.542	1.500	
Oval+5.6	1.584	1.500	

Table 3.3: Models developed to assess the geometry of the zonular fibers.

3.3 Capsular Bag Attachment

The subject of the connection between the zonules and the capsular bag has been approached in different manners. As reported in Section 2.2, initial studies involved a zero-width ring of insertion in the capsule, and connected this component to the internal edge of the zonules (Burd et al., 2002). Following works took a different path, not portraying the zonules and instead simulating a force across a band width of the capsular bag, for each of the zonular sets, due to the numerical kinks that the previous approach had as a consequence of doing so (Hermans et al., 2006, 2008; Lanchares et al., 2012).

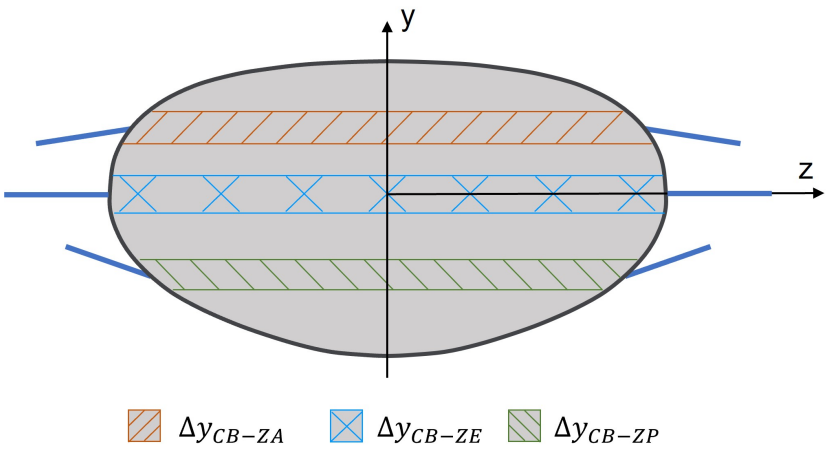

Figure 3.7: Sagittal view schematic of the attachment bands of the capsule.

In these works, the authors defined band widths of insertion of $\Delta y_{CB-ZA} = 0.5mm$, $\Delta y_{CB-ZE} = 0.5mm$ and $\Delta y_{CB-ZP} = 0.4mm$ for the anterior, equatorial and posterior zonules, respectively.

With the objective of avoiding the numerical kinks originated by the zero-width rings, whilst also portraying the essential components of the lens complex that are the zonules, Wang et al. (2017) implemented a tie with a master-slave approach. The authors defined as the master surface the belt of anchorage in the capsular bag for each of the zonular sets, with widths of correspondingly $\Delta y_{CB-ZA} = 0.86mm$, $\Delta y_{CB-ZE} = 0.86mm$ and $\Delta y_{CB-ZP} = 0.99mm$, for the anterior, equatorial and posterior zonular fibers.

Therefore, with the objective of understanding the impact of the insertion band width in the biomechanical behavior of the lens, several models were assembled, where the connection between capsule and zonules was varied. The master surfaces corresponding to the capsule's insertion bands were varied in width. The representation of the bands of the capsule is depicted in Figure 3.7, where Δy_{CB-ZA}, Δy_{CB-ZE} and Δy_{CB-ZZ} represent the band widths of the master surfaces of the capsule for attachment to the anterior, equatorial and posterior zonules. The configuration of the band width of each of the models is displayed in Table 3.4, where models *Band3* and *Band7* have a band width correspondence with values determined by Hermans et al. (2006) and Wang et al. (2017), respectively.

Model	Anterior Band Width $\Delta y_{CB-ZA}[mm]$	Equatorial Band Width $\Delta y_{CB-ZE}[mm]$	Posterior Band Width $\Delta y_{CB-ZP}[mm]$
Band1	0.167	0.167	0.133
Band2	0.333	0.333	0.267
Band3	0.500	0.500	0.400
Band4	0.590	0.590	0.548
Band5	0.680	0.680	0.695
Band6	0.770	0.770	0.843
Band7	0.860	0.860	0.990

Table 3.4: Band widths of the capsule's anchorage regions for different model configurations.

The models *Band1* to *Band2* were constructed in two equal band-width intervals between zero-width insertion rings and the band widths of model *Band3*, and the remaining models (*Band4* through *Band6*) were assembled in three equal band width intervals between the band widths of *Band3* and *Band7*.

For all the models, and each of the zonular sets, the central y-coordinate of the band width was correspondent with the y-coordinate of the internal edge of the zonule.

3.4 Gravity in the Lens Complex

In order to assess the influence of the gravitational force in the lens complex, the final healthy model, after geometrical and interaction optimizations (Sections 3.4 and 3.3), was also modeled with the imposition of the gravity acceleration ($\vec{g} = 9.81m/s^2$) as a loading condition.

In order to do so, the density of the zonules was set as $\rho_Z = 1000kg/m^3$, equivalently to the value defined by Bocskai and Bojtár (2013).

Resorting to *in vitro* scattered data obtained by Rosen et al. (2006), portrayed in Figure 3.8, the same authors provided a relationship between the lens volume and weight, described by Equation 3.4.

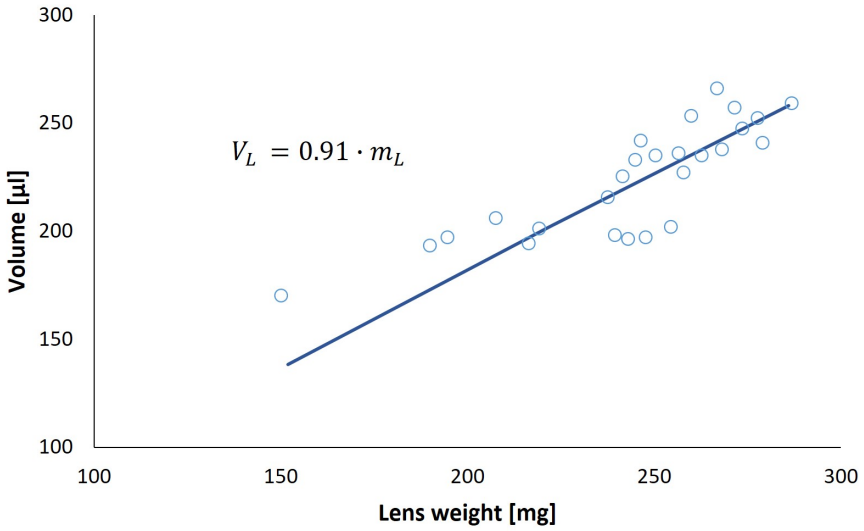

Figure 3.8: Comparison of human lens weights and volumes (adapted from Rosen et al. (2006)).

Where, V_L accounts for the internal volume of the lens and m_L for its mass. Accordingly, the specific volume of the lens is valued as $v_L = 0.91[\mu l/mg]$ and its resulting density is then defined as $\rho_L = 1099[kg/m^3]$.

$$V_L = 0.91 \cdot m_L \rightarrow v_L = 0.91[\mu l/mg] \rightarrow \rho_L = 1.099[mg/\mu l] = 1.099[mg/mm^3] = 1099[kg/m^3] \quad (3.4)$$

Since the values found by Rosen et al. (2006) included the lens capsule in its full integrity, this component also had a density value of $\rho_{CB} = 1099kg/m^3$.

3.5 Pseudoexfoliative Conditions

Taking into account the findings presented in Subsection 2.1.2, the dialysis of the zonules was modeled bearing in mind the description provided by Naumann et al. (1998), where the pseudoexfoliative material is said to intercalate the presence of the zonular fibers, and lifting them off locally, leading to the separation of the fibers from their anchorage to the ciliary muscle, lens capsule or even both.

Additionally, for the less common case of disruption of the fibers in particular, the resulting effect of this type of dialysis lacks information related to the material properties that the fibers retain after degeneration (whether they become less stiff or more fragile).

As such, the only type of degeneration considered was the one where the thickness of the zonular set of fibers is reduced, due to the local lifting off of a portion of the fibers, whether it be from the ciliary muscle or the lens capsule.

Consequently, two cases of zonular fiber separation were considered. A moderate situation, where 50% of the fibers were disconnected, leading to a resulting thickness of the afflicted areas of $T_Z = 5\mu m$ and a severe case, where the critically affected areas had 5% of healthy zonular thickness ($T_Z = 0.5\mu m$) with transitional regions of moderate dialysis, where $T_Z = 5\mu m$.

When implementing the zonular degeneration in the developed models, the findings by Schlötzer-Schrehardt and Naumann (1994) and Wilson et al. (1987) were taken into account and consequently, the dialysis was imposed in the anterio-posterior direction. As such, the anterior zonules, the group of anterior and equatorial fibers, and the group of three sets of zonular fibers were degenerated in order to ascertain their influence in the biomechanical and optical behavior of the lens complex.

Nonetheless, for the sake of the individual characterization of the impact of the singular equatorial and posterior sets of zonules in the process of disaccommodation, the individual dialysis of the equatorial and posterior fibers was also modeled.

The location of the zonular dialysis origin was defined taking into account the study by Wilson et al. (1987), that found that the zonulopathy could either occur in the inferior or superior regions of the zonules. Subsequently, two types of degeneration origin were implemented in the designed models, one with inferior zonular dialysis, and the other with a superior origin in the zonulopathy appearance.

On the subject of the dialysis extension, Hoffman et al. (2013) presented the term clock-hours, as already mentioned in Section 2.1.2. The clock-hour elements that denoted a transition between the severity of the zonulopathy conditions were 3 and 6 clock-hours. Nonetheless, with the objective of recreating a gradual disruption of the zonules, when modeling the extension of zonular dialysis, the degeneration was accounted for 1, 3, 6, 9 and 12 clock-hours, which corresponded to angles of 30, 90, 180, 270 and 360 degrees of zonulopathy.

Note that, for the case of severe dialysis of the zonules, due to the transitional regions of moderate degeneration, the models were designed as follows: for x clock-hours of severe degeneration, whether it be from superior or inferior origin, two regions of $x/2$ clock-hours were assigned to have moderate dialysis, on the medial and lateral sides of the severe dialysis region. As an example, for the case of severe superior dialysis with extension of 30 degrees, the 30 degree region would have a thickness

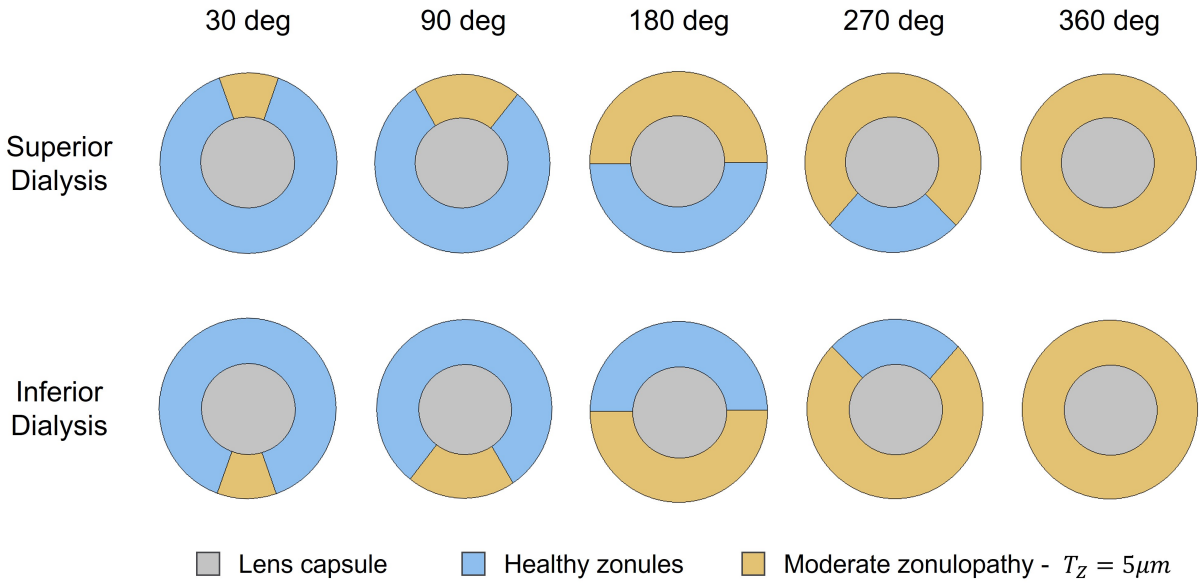

Figure 3.9: Frontal view schematic of the models with moderate anterior zonule dialysis.

accounting for 5% of the healthy condition, with 15 degrees of the medial and lateral sides of the region accounting for a moderate zonulopathy, with 50% of the healthy zonular thickness.

Given the mentioned aspects of pseudoexfoliation, all these variables were taken into account, when generating the designed pseudoexfoliation models, i.e.: the thickness of the resulting degenerated fibers; the sets of dialysed zonules; the origin of zonulopathy; and finally, the angle extension of dialysis.

In order to better illustrate the design enforced in the models, Figures 3.9 and 3.10 show the frontal view of dialysis of the anterior zonules, for moderate and severe cases, respectively. The figures represent all angle cases of zonulopathy extension, as well as the two cases of dialysis origin (inferior and superior).

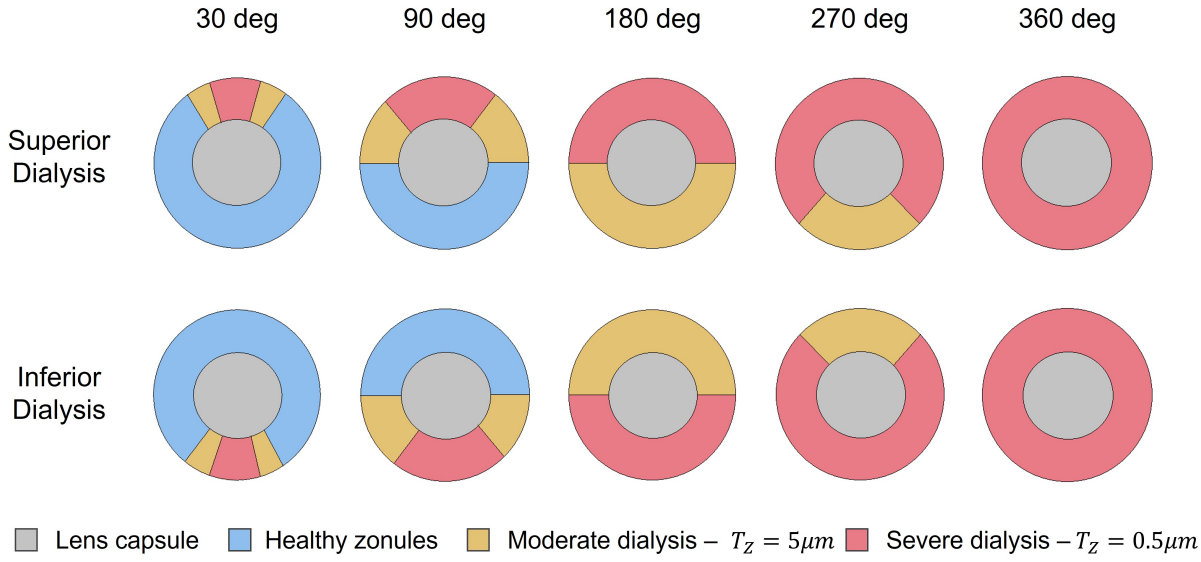

Figure 3.10: Frontal view schematic of the models with severe anterior zonule dialysis.

Considering the models represented in Figures 3.9 and 3.10, the study of the dialysis that comprehends the individual behavior of the anterior fibers leads to a total number of 18 models. Although the figures account for 20 models, the 360 degree extension for the superior and inferior cases of dialysis are actually the same.

Given that the work developed in this dissertation involves the study of the anterior (ZA), equatorial (ZE), posterior (ZP), anterior and equatorial ($ZA + ZE$), and finally all sets of zonular fibers ($ZA + ZE + ZP$), a total of 90 models were designed in order to portray all the mentioned variables of the pseudoexfoliative conditions. The summary of the models developed for the pseudoexfoliation syndrome is depicted in Appendix C, Table C.8.

3.6 Procedures for Result Analysis

Due to the amount of designed models, in order to facilitate the result analysis process, a script was developed in Python ®(Python Software Foundation, Delaware, USA), where several data outputs were collected, throughout the six equal increments of lens deformation.

The lens thickness was analyzed taking into account the y-coordinates of the most anterior and posterior points of the lens in the optical axis. The calculation of the percentage thickness variation of the lens was computed resorting to Equation 3.5, where T_{L_I} and T_{L_F} account for the lens thickness values before and after disaccommodation, respectively.

$$\Delta T_L[\%] = \frac{T_{L_I} - T_{L_F}}{T_{L_I}} \cdot 100 \tag{3.5}$$

The lens radius variation was calculated resorting to Equation 3.6. Nonetheless, due to the axi-asymmetric nature of some of the developed models (as described in Section 3.2), the radius calculation was performed by obtaining the average value of four different radii values. These were measured in the most medial, lateral, superior and inferior nodes of the lens in its equatorial plane. The averaged initial and final radii of the lens are depicted in Equation 3.6 as R_{L_I} and R_{L_F}, respectively.

$$\Delta R_L[\%] = \frac{R_{L_F} - R_{L_I}}{R_{L_F}} \cdot 100 \tag{3.6}$$

Equations 3.5 and 3.6 allow for the comparison of thickness and radius variations of the lens with values from literature data presented in Section 2.2, Table 2.1.

The total force suffered by the zonular fibers was computed taking into account the sum of the individual force value endured by each of the nodes composing the mesh of the zonular sets.

The evaluation of the stress endured by the components of the lens complex was performed taking into account the Von-Mises stress values, since this equivalent stress quantity allows for a quantification of the stress magnitude endured by these components. Accordingly, this stress measurement provides a valuable insight on the most and least solicited regions of each component.

Subsequently, maximum, minimum and average values of Von-Mises stress were computed for the capsular bag, the collective group of three zonular sets and, finally, for the lens, composed by its nuclear

and cortical features.

When evaluating the capsular bag's behavior throughout the imposed disaccommodation of the lens complex, two outcomes were analyzed for comparison with literature data provided by Lanchares et al. (2012), the logarithmic strain and principal stress endured by the capsule. Accordingly, the maximum and minimum logarithmic strains of the capsular bag during deformation were obtained for all the models. The same methodology was applied when evaluating the principal stress values endured by the capsule during disaccommodation, where maximum and minimum stress values were measured. The authors also depicted the range of principal stress values endured by the cortex and nucleus and, as such, these stress quantities were also obtained.

The Central Optical Power was also calculated for all models, throughout the six simulation steps defined for the disaccommodation process. According to literature values found for the refractive indexes of the relevant mediums, the refractive index of the aqueous humour and vitreous body was defined as $n_p = 1.336$, whereas the equivalent refractive index of the lens was determined as $n_l = 1.42$.

The Central Optical Power was measured in the sagittal plane of the lens, and based on the anterior and posterior radii of curvature of the lens in this plane.

When calculating the radii of curvature of the lens, the estimation of these quantities was based on the simplification that the surfaces of the lens were perfect spheres, similarly to the approaches by other authors (Wang et al., 2016), where this method was defined as a spherical surface approximation.

As such, the approach taken in this work was based off on finding a circle passing though three given points, with y and z coordinates, given that the points were located in the sagittal plane. The mathematical description of a circumference, in its general form leads to Equation 3.7.

$$y^2 + z^2 + 2 \cdot c \cdot y + 2 \cdot d \cdot z + f = 0 \tag{3.7}$$

Where the coordinates of the center of the circumferences and its radius are given by $y_{center} = -c$, $z_{center} = -d$ and $R = \sqrt{y_{center}^2 + z_{center}^2 - f}$, respectively.

For three given points, there will be three equations such as Equation 3.7 for three unknown variables, allowing for the solution of the value of the corresponding radius of curvature.

Nonetheless, due to the aspherical nature of both the anterior and posterior surfaces of the lens (Liou and Brennan, 1997), the estimation of the curvature radius would not be feasible when obtaining only one value for this variable. As a result, a total of 6 nodes per radius of curvature were chosen, in order to provide for the calculation of the radii for different combinations of points. For illustration purposes, a table showing a total number of 20 combinations of three point groups is displayed in Table B.2, Appendix B.

Furthermore, also due to the asphericity of the lenticular surfaces, the location of the chosen nodes that would allow for the estimation of the anterior and posterior radii of curvature had to be the same for all models, in both anterior and posterior surfaces. Similarly to the procedure by Wang et al. (2016), the chosen nodes could only be located within the central paraxial $3mm$ zone of the lens.

Given the mentioned criteria, the resulting representation of the obtained node dispositions used

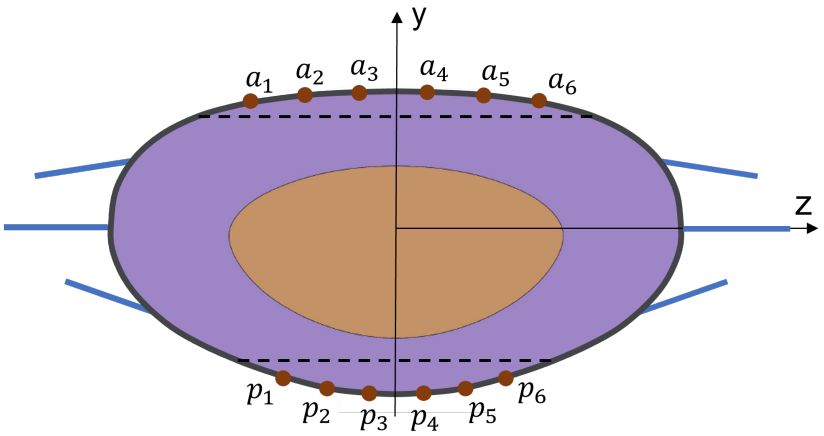

Figure 3.11: Sagittal view schematic of the node locations used in the calculation of the lenticular radii of curvature.

to calculate both the anterior and posterior radii of curvature is represented in Figure 3.11, where the dashed lines represent the anterior and posterior planes that define the central paraxial $3mm$ zone of the lens. The coordinates of the mentioned nodes are displayed in Appendix B, Table B.1.

Chapter 4

Results and Discussion

The present chapter analyzes the models developed throughout this dissertation, comparing the base model, constructed in Section 3.1, with outcomes from finite element method literature data. Further modeling developments of the healthy lens complex are also analyzed. Additionally, the evaluation of the refined model under afflicted conditions of pseudoexfoliation is also presented.

4.1 The Healthy Lens Complex

The result analysis of the healthy lens complex is based on the initial model developed in Section 3.1. Taking this original design as a foundation, the impact of changing both the frontal geometry of the zonules and the anchorage regions of the capsular bag is further scrutinized in order to evaluate their mechanical, optical and physiological relevances in this work's context.

4.1.1 Initial Model

The base model, constructed taking into account the methodologies of Section 3.1, presented the following lens thickness variation result: the lens flattened $\Delta T_L = 14.20\%$ during the disaccommodation process, similarly to the 62 year-old model of Wang et al. (2019), which found a decrease in lens thickness of 15.80%.

The lens radius increased $\Delta R_L = 7.87\%$, similarly to the values found for the 60 year-old lens modeled by Weeber and Van Der Heijde (2008) ($\Delta R_L = 7.00\%$).

The resulting force in the zonular fibers was totaled as $F_Z = 134.1mN$, which shows a slight increase from the values found in Table 2.2. Nonetheless, Hermans et al. (2008) denoted an increase of the total zonular force with age progression. As such, the values found for the initial model fit with the authors description, given that this older lens has values that are greater than the ones found for younger lenses in the literature data.

The logarithmic strain (LE_{CB}) endured by the capsular bag ranged from $1.66E-2$ to $8.25E-2$. Figure 4.1 shows the visual representation of the values found for both the initial model and the one portrayed by Lanchares et al. (2012), of a 30 year-old lens. Note that, as previously mentioned, the

capsular bag's membrane designed by Lanchares et al. (2012) had a non-constant thickness throughout its structure. As such, in regions with a thinner capsule membrane, such as the posterior pole, there was a greater level of strain endured. Nevertheless, the equatorial area of the capsule also endured a great strain magnitude, even though this was the region where the capsule was thicker ($T_{CB} = 20\mu m$). In this region, the strain endured by the capsule was valued as $LE_{CB} = 7.03E - 2$. This strain level is somewhat comparable with the behavior of this work's initial model in the equatorial region, since the whole structure of the initial model's capsule has a value of $T_{CB} = 20\mu m$. Accordingly, in the equatorial region of the capsule, the initial model presents a logarithmic strain value of $LE_{CB} = 8.25E-2$, a similar result to Lanchares et al. (2012) in the same location.

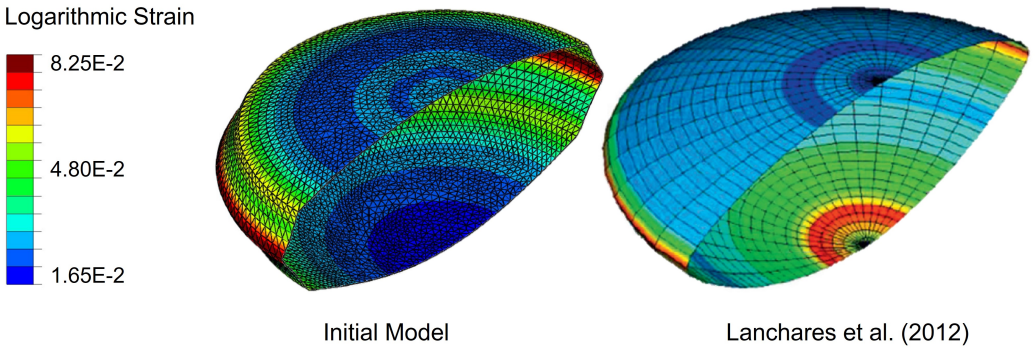

Figure 4.1: Distribution of the logarithmic strain values along the capsular bag. Comparison between current work and Lanchares et al. (2012) simulation with 30 year-old lens.

The principal stress values found for the capsular bag in the validation model ranged from $41.53kPa$ to $171.59kPa$. When compared with Lanchares et al.'s model of a 30 year-old lens, whose values ranged from $82.84kPa$ to $160.30kPa$, the principal stress distributions can be observed in Figure 4.2, where the behaviors of the membranes have slight differences in the most afflicted regions, due to the non-constant capsular thickness of Lanchares et al.'s model. As mentioned by the authors, the maximum stress value found for the capsule was located in the areas where the capsular membrane was thinner, in particular, its posterior pole. Additionally, the stress has a lower value in the equatorial area, due to the greater thickness of the capsule in that region.

As for the case of the initial model, the thickness of the capsule is constant throughout its whole structure. Consequently, the regions under a greater amount of stress are the capsular bag's anchorage rings, which connect to each of the zonular fiber sets, given that the effort caused by the stretching of the zonules leads to a stress concentration in the regions of attachment to the connected structure, the capsule. As such, the capsule's attachment ring to the equatorial fibers is under the greater amount of stress ($172.02kPa$), whilst the anterior and posterior regions of insertion show stress values of $137.43kPa$ and $105.96kPa$, respectively.

The stress in the nucleus and cortex was evaluated simultaneously, similarly to the approaches found in Table 2.2. The initial model's values found for the principal stress on the cortex and nucleus ranged from $-0.654kPa$ to $0.841kPa$. This range of values is similar to the one found by Lanchares et al. (2012), which presented a principal stress ranged from $-0.247kPa$ to $0.526kPa$.

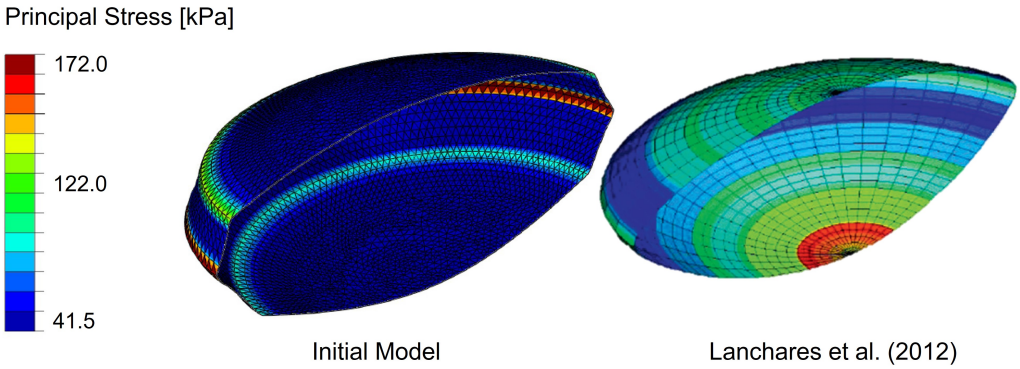

Figure 4.2: Distribution of the principal stress values along the capsular bag. Comparison between current work and Lanchares et al. (2012) simulation with 30 year-old lens.

Furthermore, the Von-Mises stress values of the present model vary between $0.020kPa$ and $0.188kPa$. In Figure 4.3, the depiction of Von-Mises stress distribution can be observed for the initial model, as well as the results found for the modeled 62 year-old lens modeled by Wang et al. (2019). As can be observed in the mentioned figure, both the cortical and nuclear regions of Wang et al.'s lens are under a greater amount of stress, although the difference is not significant since the range of Von-Mises stress is actually of a considerably small magnitude.

Nonetheless, the external region of the nucleus is the one under greater stress magnitudes for the model depicted by Wang et al. (2019), whereas the stress distribution in the initial model's nucleus shows a more uniform behavior.

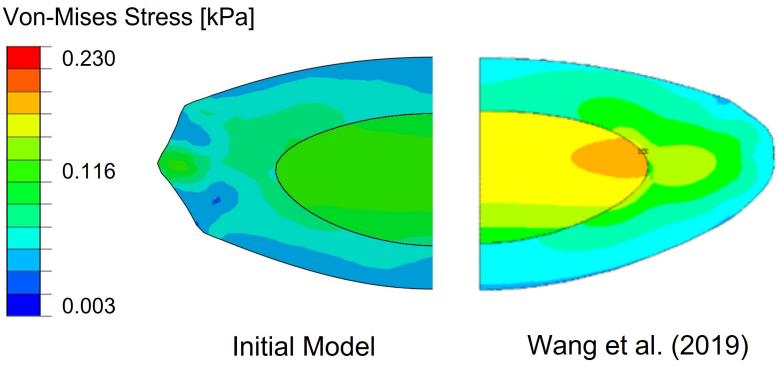

Figure 4.3: Comparison of the distribution of the Von-Mises stress values along the cortex and nucleus between current work and the 62-year-old model by Wang et al. (2019).

When analyzing the cortical stress distribution, for the case of the initial model, there is a greater stress in the regions proximal to the capsule's attachment rings of the zonular fibers, showing a stress response of the cortex to the displacement of the fibers caused by the disaccommodation process. This is not the case for the 62 year-old lens modeled by Wang et al. (2019), that shows a greater stress in the internal and equatorial region of the cortex, displaying a smaller amount of stress in the regions of attachment to the zonules. This might be the case because of the implementation of a smooth coupling between the capsule and the zonular fibers, where a master-slave approach was applied between bands of the capsule and the internal edge of the zonules. This subject will be further analyzed in

Subsection 4.1.3, where the implementation of capsular insertion bands is also considered in this dissertation. Nonetheless, the stress distribution found for the initial model is similar to the one found by Hermans et al. (2006), that also presented a greater magnitude in the cortical regions proximal to the capsular attachment regions of the zonules.

The evaluation of the Central Optical Power (COP) evolution concerned the analysis of several quantities in Equation 2.1, where the lens radii of curvature and thickness were the quantities that varied with the deformation of the lens. The initial model's obtained values of the anterior and posterior curvature radii (r_a and r_p) are portrayed in Figure 4.4, where the values obtained by Wang et al. (2017, 2019) are also represented, being that the former publication only presents the initial and final values of both the anterior and posterior radii of curvature.

Resorting to Equation 2.1, one can then calculate the value of the Central Optical Power throughout the deformation of the lens, from the accommodated to the relaxed state. Its resulting depiction is represented in Figure 4.5, along with values estimated by Wang et al. (2017, 2019).

The values determined by Wang et al. (2017) and Wang et al. (2019) led to the calculation of the amplitude of accommodation, with values of $\Delta COP = 3.01D$ and $\Delta COP = 1.94D$ for the studied 35 year-old and 62 year-old lenses, respectively. The initial model's estimated amplitude of accommodation is $\Delta COP = 1.57D$.

Note that the behaviors of the Central Optical Power of the lenses differ in the sense that the initial model has an increase of COP in the first and second steps of the lens deformation, while the same does not happen for the remainder of the models, which only show a COP increment in the first step.

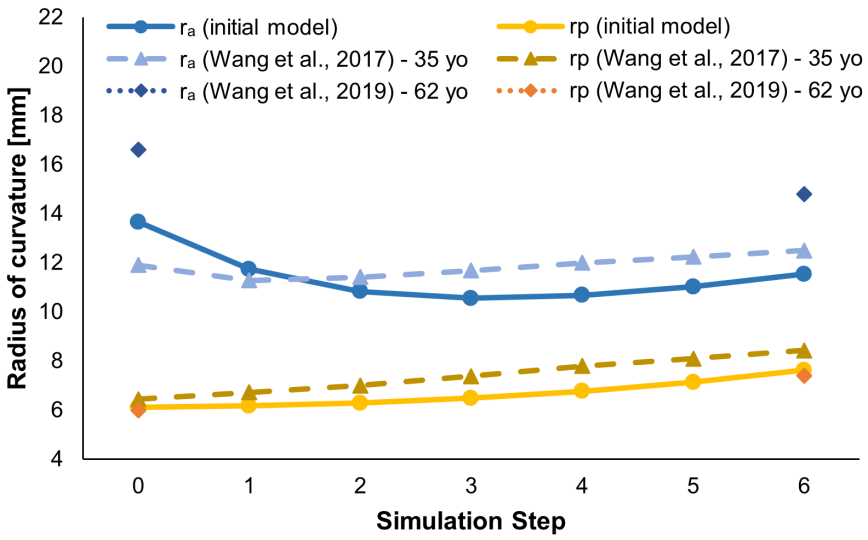

Figure 4.4: Evolution of the anterior and posterior radii of curvature of the lens, throughout its deformation.

When examining Figure 4.4, one observes that the slopes of the posterior radius of curvature of all the models have the same course of action i.e., grow throughout the deformation of lens (due to its flattening). The same cannot be said for the anterior radius of curvature, being that for Wang et al. (2017) this quantity decreases slightly in the first step and increases throughout the rest of the simulation.

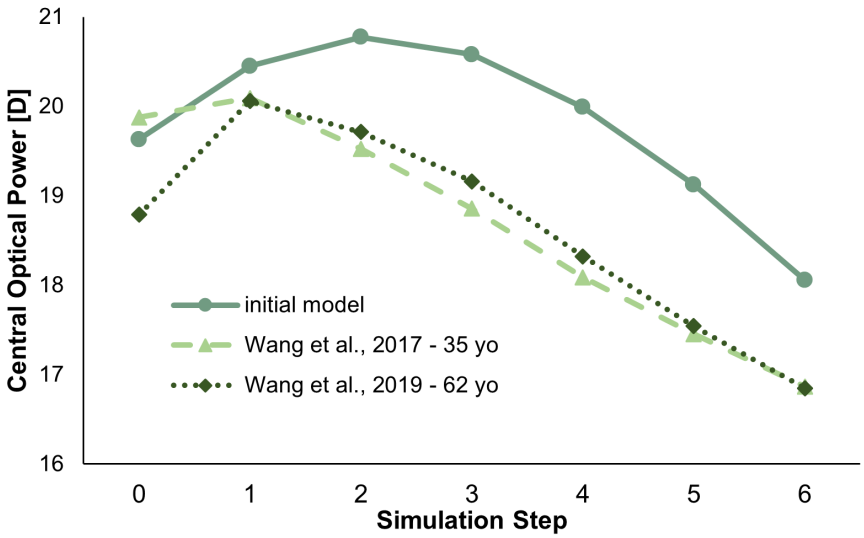

Figure 4.5: Evolution of the Central Optical Power of the lens, throughout its deformation.

Nonetheless, the value for the anterior radius of curvature of the initial model has a steeper reduction in the first step, and a less significant one in the second step, which then are mitigated throughout the rest of the deformation, with the increase of r_a.

As such, the slope difference found in the COP evolution of the initial model and the literature data can be explained with the referred behavior of the anterior radius of curvature. This result is due to the fact that the lens surfaces are not perfectly spherical: this is an assumption taken when performing the calculation of the radii of curvature, which can lead to disparities between slopes in the portrayed models. Given that Wang et al. (2017, 2019) did not disclose the locations of the coordinates chosen in the calculation of the radii of curvature, their methodologies are inevitably different from the one implemented in this work and, as such, the behavior of the Central Optical Power cannot be the same for the analyzed models.

Nonetheless, the value found for the accommodation amplitude of the initial model, $\Delta COP = 1.57D$, denotes a close correspondence with the result by Wang et al. (2019) ($\Delta COP = 1.94D$), that also portrayed a 62 year-old lens. This result shows that the lens is under presbyopic conditions, in the sense that it cannot accommodate as efficiently as younger lenses, as should be expected for a lens of 62 years of age. Additionally, the initial model's value is a better fit for the amplitude of accommodation estimates by Duane (1922), that determined a maximum value of the accommodation amplitude of 62 year-old lenses as $\Delta COP_{max} = 1.70D$, as portrayed in Figure 2.5.

4.1.2 Geometry of the Zonular Fibers

As described in Section 3.2, the frontal geometry of the zonular fibers was varied in order to ascertain the importance associated with the clinical data provided by Biermann et al. (2011).

The designed models and corresponding values found for the amplitude of accommodation, resulting zonular force and lens radius and thickness variations are represented in Table 4.1.

Additionally, the accommodation amplitude results are illustrated in Figure 4.6, where the values

Model	$\Delta COP[D]$	$\Delta R_L[\%]$	$\Delta T_L[\%]$	$F_Z[mN]$
Oval-5.6	2.03	8.14	15.20	142.8
Oval-2.8	1.73	7.99	14.59	138.0
Initial Model	1.57	7.87	14.20	134.1
Oval+2.8	1.45	7.76	13.86	131.4
Oval+5.6	1.38	7.66	13.55	129.9

Table 4.1: Results found for models assessing the zonular fiber geometry.

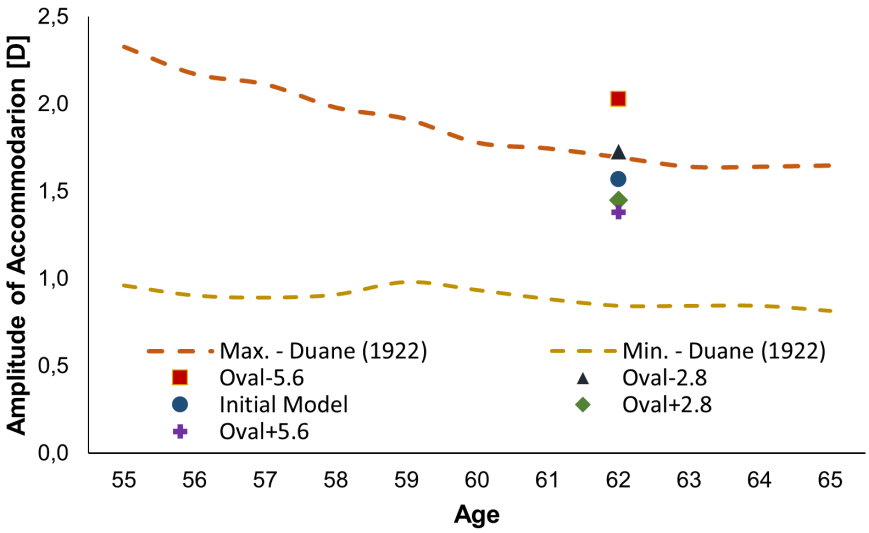

Figure 4.6: Accommodation amplitude values obtained for the zonular geometry assessment, along with values obtained by Duane (1922).

obtained for each model are represented along with the maximum and minimum values of attainable accommodation defined by Duane (1922), between the ages of 55 and 65 years-old. For the sake of simplicity, the values obtained by Ungerer (2000) are not represented, since the models depict 62 year-old lenses and Ungerer only presents accommodative amplitude data up to ages of 60 years-old.

The amplitude of accommodation of the lens showed a reduction throughout the evolution of the models presented in Table 4.1. For the model with the smallest average zonular length ($\overline{l_Z}$), *Oval-5.6*, the amplitude of accommodation had the highest value, with $\Delta COP = 2.03D$. Both this model and *Oval-2.8* had accommodation amplitude values that were outside of the range defined by Duane (1922) (see Figure 4.6).

As the zonular average length increased with model progression, the amplitude of accommodation decreased, reaching the lowest value in model *Oval+5.6*, with a resulting accommodative capacity of $\Delta COP = 1.38D$.

This is the model that presented the best approximation to the average accommodation amplitude value of the range presented by Duane (1922) for 62 year-old lenses ($\overline{\Delta COP} = 1.27D$).

The evolution of the lens radius and thickness variations denotes a similar trend: as the zonular average length increases with the evolution of the models, the variations in thickness and radius of the lens decrease.

As for the resulting force in the zonular fibers, there is also a decrease in the presented values, as the

fibers average length increases. These values are consistent with the rationale based on the following: when one considers a single zonular fiber as a beam structure, its deformation under axial loading can be depicted in Equation 4.1. For constant values of zonular displacement (δ_z), material properties (K_z) and cross-sectional area (A_z), when one augments the average zonular length ($\overline{l_z}$), the resulting force on the zonular fiber (f_z) decreases, in order to balance said equation.

$$\delta_Z = \frac{f_Z \cdot l_Z}{K_Z \cdot A_Z} \tag{4.1}$$

As such, the total force values found in Table 4.1 are consistent with the reasoning found resorting to Equation 4.1: the total zonular force has the greatest magnitude ($F_Z = 143.1mN$) for the case of model *Oval-5.6* and *Oval+5.6* depicts the model with the smallest total zonular force ($F_Z = 129.9mN$).

When comparing the stress endured by the zonular fibers after disaccommodation, the behavior of the anterior zonules is depicted in Figure 4.7. The figure illustrates the Von-Mises stress endured by the anterior zonules for the most extreme models (*Oval-5.6* and *Oval+5.6*) and the *Initial Model* from a frontal perspective.

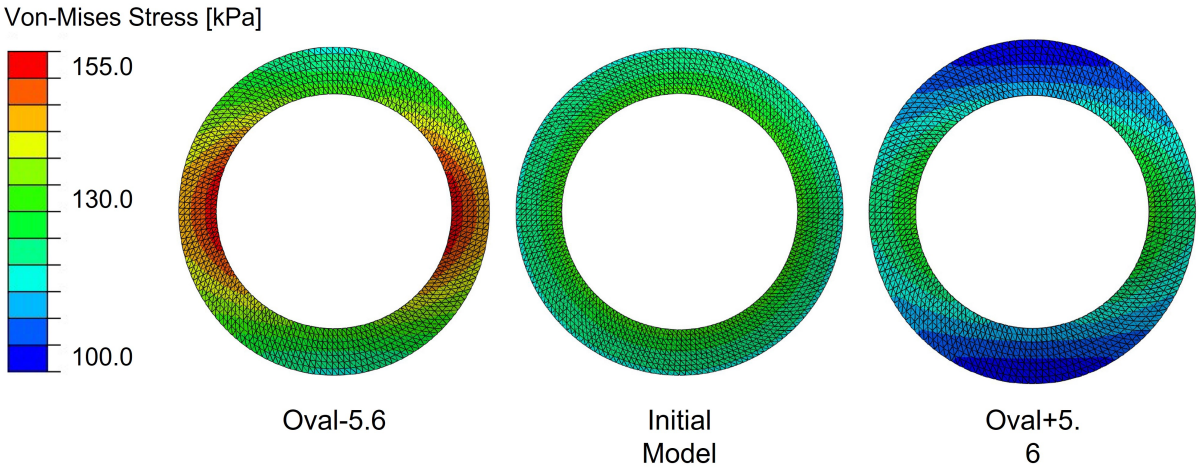

Figure 4.7: Von-Mises stress in the anterior zonules, for models *Oval-5.6*, *Initial Model* and *Oval+5.6* (frontal view).

For the cases of *Oval-5.6* and *Oval+5.6*, the greater stress magnitude is concentrated in the longitudinal direction, since this is the location of the shorter fibers. As the alignment of the fibers evolves from a horizontal to a vertical direction, the stress endured by fibrils decreases, reaching a minimum value when vertically aligned. As can be noted in Figure 4.7, model *Oval-5.6* presented the greatest stress magnitude values ($117.6 - 153.7kPa$), whereas model *Oval+5.6* was the one with less significant stress values, ranging from $100.6kPa$ to $128.7kPa$.

As for the case of the *Initial Model*, the stress endured by the fibers is axisymmetric, due to the fact that the fibers have the same length in the vertical and longitudinal directions. The Von-Mises stress values endured by the anterior zonules in the case of the *Initial Model* varied between $118.0kPa$ and $129.6kPa$.

These results led to the deduction that with the model progression of Table 4.1, the stress values

endured by the zonules decrease as well.

The capsule's Von-Mises stress values can be observed in Figure 4.8. Both the models *Oval-5.6* and *Oval+5.6* show smaller magnitudes of stress in the vertical direction, when compared with the longitudinal one (Figure 4.8, frontal view), similarly to the behavior of the zonular fibers.

The same cannot be said for the *Initial Model*, since the capsule's behavior is axisymmetric, equivalently to the anterior zonular stress depicted in Figure 4.7. As previously stated, this is due to the circular geometry nature of the zonular fibers.

The increase of the average zonular fiber length also has an impact in the stress surrounding the zonular insertion rings of the capsule, that had as a consequence the overall reduction of the stress around these regions. Nonetheless, even for the case of *Oval+5.6*, the capsule denotes a higher stress value in the proximity region of the equatorial zonule insertion.

Model *Oval+5.6* shows an overall reduction of the stress endured throughout the capsule (with the exception of the anchorage ring to the equatorial zonules, as can be noted in Figure 4.8).

When comparing the average value of the Von-Mises stress felt by the capsular bag in *Oval-5.6* and *Oval+5.6*, the former presents a value of $81.62kPa$, whereas the latter shows an average value of $70.75kPa$, leading to a reduction of 13.31%.

This suggests that due to the longer average zonular length, during the disaccommodation process, the pulling of the fibers leads to a smaller stress in the capsule, as is the case for model *Oval+5.6*.

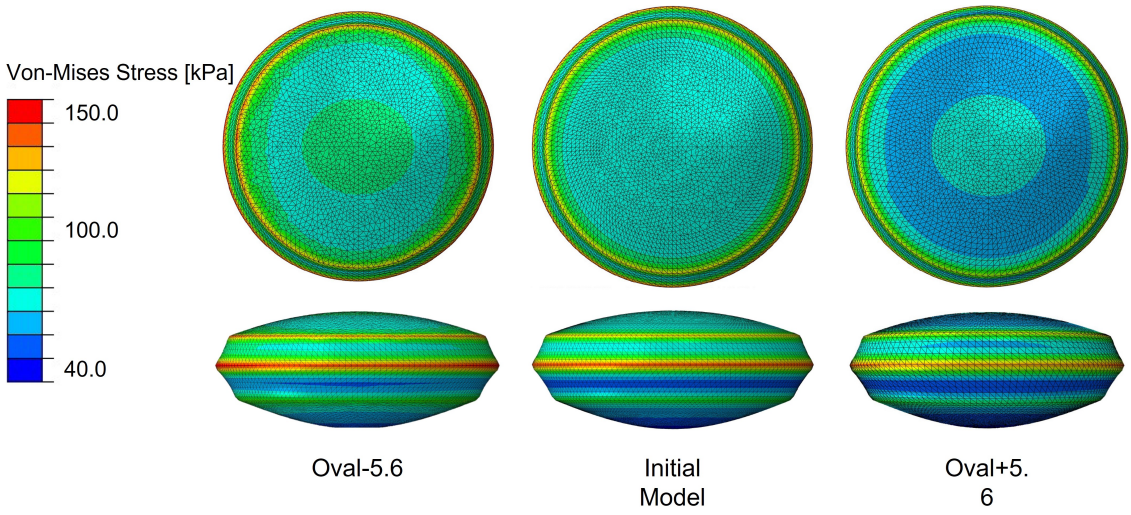

Figure 4.8: Von-Mises stress in the capsular bag, for models *Oval-5.6*, *Initial Model* and *Oval+5.6* (frontal and superior views).

The results concerning the oval geometry of the zonular fibers show that even a small percentage difference in the average length of the zonules denotes a considerable variation in the resulting amplitude of accommodation, highlighting the need for the representation of a correct geometry of the zonules.

When selecting the model with the most significant physiological relevance, *Oval+5.6* shows the accommodative result that best approximates the average value found by Duane (1922), while also portraying the model with the closest zonular force estimation, when compared with literature values presented in Table 4.4.

Consequently, after careful consideration, *Oval+5.6* became the model that serves as a base for further healthy lens complex analysis, given that this model presented the optimized geometrical configuration of the zonules, within the tested models.

4.1.3 Capsular Bag Attachment

In this subsection, the influence of creating anchorage bands on the capsular bag is analyzed, with the goal of creating an optimized boundary condition configuration for this component. Taking as a base model the one selected in Subsection 4.1.2, *Oval+5.6*, where the fibers are anchored to zero width insertion rings, several models were construed according to Table 3.4.

Initially, when comparing the first designed model from Table 3.4 (*Band1*), with *Oval+5.6*, the accommodation amplitude showed a slight reduction in value (from $1.38D$ to $1.30D$), and the same occurred with the total force acted on the zonules (from $F_Z = 129.9mN$ to $F_Z = 113.4mN$). For the case of both the radius and thickness change of the lens, the two models showed no significant difference. The resulting values for the zonular force, lens thickness and radius variations and amplitude of accommodation of these models, as well as the remaining models depicted in Table 3.4, are represented in Table 4.2.

The results depicted in Table 4.2 show that although there is a slight difference between values of the models *Oval+5.6* and *Band1*, there are no relevant differences between values from model *Band1* through model *Band7*, in all the quantities depicted.

These values suggest that due to the imposition of the anchorage bands, the zonular connection was performed in a more uniform manner than with zero-width rings, but that the variation of widths of the bands does not have an importance. Accordingly, all models developed in Table 3.4 achieved a slight reduction in zonular force, when compared with the zero-width base model, *Oval+5.6*, but did not show a significant disparity within the group.

From models *Band1* through *Band7*, the values found for resulting zonular force remained almost constant, ranging from $F_Z = 112.9mN$ to $F_Z = 114.4mN$. The discrepancy between the amplitude of accommodation of the mentioned models also has a maximum value of 0.04 dioptres, which suggest a negligible disparity between models. The same occurs for both the lens thickness and radius variations of all the models excepting model *Oval+5.6*.

Model	$\Delta COP[D]$	$\Delta R_L[\%]$	$\Delta T_L[\%]$	$F_Z[mN]$
Oval+5.6	1.38	7.66	13.55	129.9
Band1	1.30	7.86	13.60	113.4
Band2	1.34	7.89	13.63	114.4
Band3	1.32	7.90	13.59	112.9
Band4	1.33	7.87	13.61	113.7
Band5	1.32	7.90	13.59	113.5
Band6	1.32	7.87	13.58	113.0
Band7	1.31	7.88	13.56	113.3

Table 4.2: Results found for models assessing the capsular bag attachment configuration.

The analysis of the stress distribution in the cortex and nucleus is portrayed in Figure 4.9, where the

models with zero-width rings of attachment (*Oval+5.6*) and with maximum insertion band widths (*Band7*) are depicted. These models did not account for a significant variation between stress distribution in the cortex and nucleus. Even though Wang et al. (2019) pointed out that the numerical kinks were negligible after application of the band widths in the capsular bag with the same configuration of model *Band7*, that behavior cannot be observed in Figure 4.9. Additionally, the behavior of the portrayed models continues to present a greater stress magnitude in the cortex in regions proximal to the capsular bag insertions, a behavior that had been previously noted in Subsection 4.1.1, Figure 4.3. The present results show that the application of a greater band width does not, in fact, lead to a reduction of numerical kinks in the final geometry of the lens, neither does it provide a redistribution of the stress felt by the lenticular components.

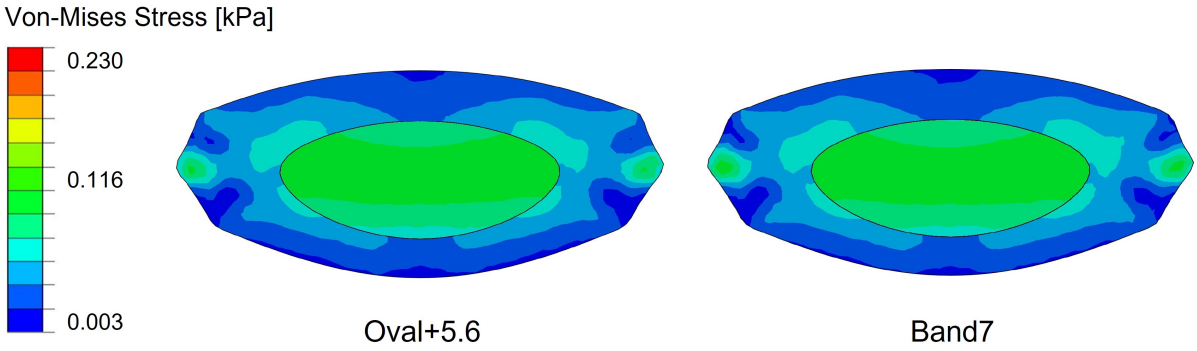

Figure 4.9: Von-Mises stress in the cortex and nucleus for models assessing the band width configuration (sagittal plane).

In essence, the greatest difference found was between the zero-width insertion rings model, and all the models with a greater-than-zero band width. Nonetheless, the values found for *Band* models show a better correlation with literature data related to the resulting force values, F_Z. Additionally, these models provide a smaller value for the accommodation amplitude, which presents a better fit with average values provided by Duane (1922) for the 62 year-old lens models, $\overline{\Delta COP} = 1.27D$. In spite of that, there were no relevant discrepancies between values of these models.

As such, the chosen model moving forward was *Band4*, where the band widths of the anterior, equatorial and posterior anchorage regions of the capsule were $\Delta y_{CB-ZA} = 0.590mm$, $\Delta y_{CB-ZE} = 0.590mm$, and $\Delta y_{CB-ZP} = 0.548mm$, respectively.

Accordingly, after optimization of the zonular frontal geometry and of the capsular band anchorage configuration, the model *Band4* was the one that presented the optimal form, serving as the final basis for the healthy lens complex model without the imposition of the gravity conditions.

4.1.4 Effects of Gravity in the Lens Complex

As mentioned in Section 3.4, the gravitational acceleration was applied to the refined healthy model, after zonular geometry and capsular band width considerations.

When accounting for the thickness and radius percentage variation, the values found for the models with and without gravity show no significant change:

- Refined model, *Band4*: $\Delta T = 13.61\%$, $\Delta R = 7.87\%$
- Gravity model: $\Delta T = 13.35\%$, $\Delta R = 7.94\%$

These values lead to the deduction that the lens has a greater radial variation and smaller thickness variation under the effect of gravity, although these differences do not show a significant nature.

The assessment of the resulting force in the zonules also showed a negligible variation between the two models: the gravity model had a reduction of $\Delta F_Z = 1.6mN$ compared to the refined model, which accounted for a total zonular force of $F_Z = 112.1mN$.

Figure 4.10 displays sectional sagittal views of the lenticular Von-Mises stress values of model *Band4*, with and without gravitational conditions. The left area of each represented lens is the anterior region, whereas the posterior region is represented in the right side of each lens.

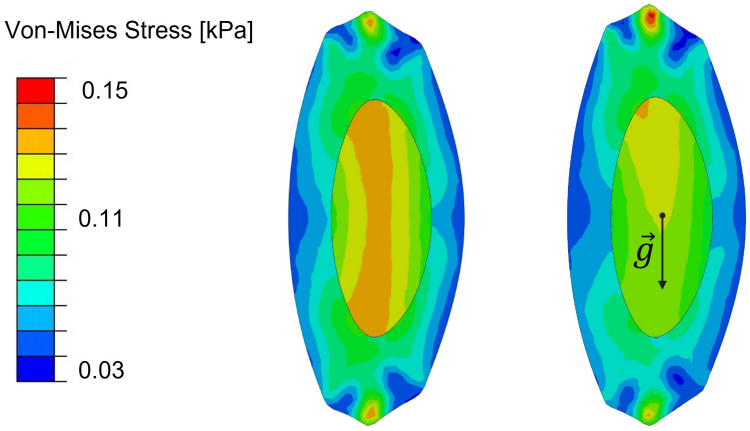

Figure 4.10: Von-Mises stress in the cortex and nucleus for models assessing gravity conditions (sagittal plane).

Although the Von-Mises stress range is similar for both models, the figure depicts stress distribution variations between the two models. There is a stress redistribution in the presence of gravity, which leads to a greater stress concentration in the superior region of the cortex, close to the region of attachment of the equatorial fibers, whereas the inferior cortical region shows a stress magnitude reduction.

Due to the presence of gravity, there is also a reduction of the overall stress endured by the nuclear region of the lens. Nonetheless, similarly to the case of the cortical region, the superior area of the nucleus endures a greater amount of stress than the inferior one.

The findings of stress redistribution are in agreement with the presence of gravity, since the lens is suspended in the main ocular structure, supported by the zonular fibers. As the superior region of the zonules endures a greater effort, the lenticular stress is also redistributed, due to the connection between the structures.

Finally, the accommodation amplitude results showed that the lens with gravity conditions had a slightly smaller capacity to accommodate, given that its accommodation amplitude was $\Delta COP = 1.24D$. This result shows a reduction of 0.09 dioptres.

From hereon out, the models developed for the diseased lens complex contained the gravitational condition, given that its consideration could have an effect when studying conditions such as the pseudoexfoliative syndrome.

	Age	$\Delta COP[D]$	$\Delta T_L[\%]$	$\Delta R_L[\%]$
Cardoso (2018)			6.90	8.10
Bahrami et al. (2016)	27	10.00	9.91	
Hermans et al. (2006)	29	8.00		7.04
Paulino (2019)	29		10.75	6.60
Lanchares et al. (2012)	30	7.50	10.90	6.60
Wang et al. (2017)	35	3.01		
Burd et al. (2002)	45	2.29		7.60
Hermans et al. (2008)	45	4.10		5.20
Weeber and Van Der Heijde (2008)	60	0.20		7.00
Bocskai and Bojtár (2013)	60	1.64	9.92	
Wang et al. (2019)	62	1.94	15.80	
Initial Model	62	1.57	14.20	7.87
Oval+5.6	62	1.38	13.55	7.66
Band4	62	1.33	13.61	7.87
Gravity	62	1.24	13.35	7.94

Table 4.3: Literature data and healthy model results for the lens geometry variation and accommodation amplitude.

	Age	Zonules F_Z [mN]	Capsular Bag LE_{CB}	Capsular Bag S_{CB} [kPa]	Cortex + Nucleus S_{C+N} [kPa]	Cortex + Nucleus VM_{C+N} [kPa]
Cardoso (2018)		71.0		53.0 - 160.0		
Hermans et al. (2006)	29	81.0				0.035 - 0.523
Paulino (2019)	29	94.5	3.01E-2 - 6.65E-2	70.3 - 123.5		
Lanchares et al. (2012)	30	78.0	4.19E-2 - 7.03E-2	82,8 - 160.3	-0,247 - 0.526	
Hermans et al. (2008)	45	56.0				
Burd et al. (2002)	45	80.0				
Belaidi and Pierscionek (2007)	46	100.0				0.060 - 0.657
Wang et al. (2016)	48	80.0				0.043 - 0.438
Wang et al. (2019)	62					0.041 - 0.204
Initial Model	62	134.1	1.66E-2 - 8.25E-2	41.52 - 171.59	-0.642 - 0.841	0.020 - 0.188
Oval+5.6	62	129.9	1.71E-2 - 8.23E-2	40.29 - 171.72	-0.616 - 0.752	0.016 - 0.196
Band4	62	113.7	1.71E-2 - 8.44E-2	46.70 - 181.54	-0.576 - 0.764	0.014 - 0.202
Gravity	62	112.1	1.69E-2 - 8.53E-2	30.11 - 182.57	-0.471 - 0.637	0.018 - 0.210

Table 4.4: Literature data and healthy model results for zonular force, strain and stress endured by the capsule and stress measurements of the nucleus and cortex.

Tables 4.3 and 4.4 display the comparison between the literature values considered in Section 2.2 and the values found for the relevant models in the present section:

- *Initial Model* is the original model developed in this dissertation, that resorted to available literature data in order to be constructed, as laid out in Section 3.1.
- *Oval+5.6* concerned the optimization of the geometrical parameters of the crystalline lens complex, where the zonular fiber length was varied in order to obtain a refined model, as presented in Section 3.2.
- The design of the capsular band width attachment regions, which led to the final model*Band4* before the imposition of gravity acceleration, was constructed as described in Section 3.3.
- Finally, the *Gravity* model was designed taking as a basis all the previous refinements, as well as the resources in Section 3.4.

All the results found for the healthy models of the lens complex are depicted in Appendix C, Table C.1.

4.2 The Lens Complex under Zonular Dialysis

Taking into account the methodology applied in Section 3.5, and the anterio-posterior direction of the deposition of the pseudoexfoliative material, the following types of models constructed allow for the degeneration of the anterior zonules, collective of anterior and equatorial fibers, and the collective of the three sets of fibers.

Considering the extension of degeneration of the disease, the models were constructed with regions of 30 degrees, 90, 180, 270 and 360 degrees i.e., throughout the whole structure of the zonules.

Taking into account the amount of data to be analyzed, the present section details on the results found for the superior dialysis origin of the zonulopathy condition, whilst also presenting a comparison between the results found with the two different origin locations of zonular dialysis. The results found for the inferior dialysis models are depicted in Appendix C, Figures C.1–C.7.

Lens thickness variation

When analyzing the resulting thickness variation of the lens, the values can be found in Figure 4.11, where the degeneration has a superior origin. The figure comprises the dialysis of the anterior zonules (ZA), equatorial zonules (ZE) and posterior ones (ZP), when degenerated in moderate (represented by the term 50%) and severe (5%) conditions. As for the case of 0 degree degeneration, the healthy model represented is the one obtained in Subsection 4.1.4, and the results obtained for 360 degree dialysis are equal for the inferior and superior degenerations, since they are in reality the same model.

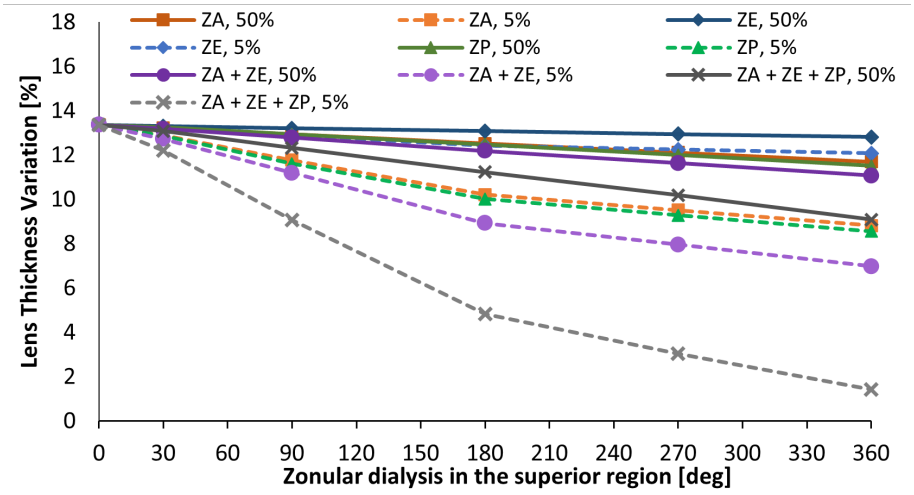

Figure 4.11: Lens thickness variation for pseudoexfoliative models with initial superior dialysis.

Concerning the lens thickness variation results, one can observe that as the disease progresses, both in severity and extension, this measurement attains increasingly smaller values.

When considering the individual impact of each of the zonules in the thickness variation of the lens, the equatorial zonules have the lowest impact in this quantity, both when degenerated with moderate (dark blue line) and severe (dashed blue line) dialysis.

In terms of the full degeneration of the zonules i.e., degeneration throughout the 12 clock-hours of

the zonular structure, the moderate degeneration of the anterior zonules (dark orange line) led to a small decrease of the lens thickness variation (reduction of 1.63% when fully degenerated, compared with the healthy model). The same occurred for the case of the moderate degeneration of the posterior fibers (dark green line), which led to a reduction of 1.85% for 360 degree dialysis. Nonetheless, for the individual characterization of the severely and fully afflicted anterior (dashed orange line) and posterior zonules (dashed green line), the lens could only attain a thickness variation of $\Delta T_L = 8.82\%$ and $\Delta T_L = 8.55\%$, respectively.

Although the 12 clock-hour moderate degeneration of the group of anterior and equatorial fibers (dark purple line) did not account for a significant reduction in lens thickness variation (reduction of 2.29% from the healthy model), the case of moderate dialysis of the three sets of fibers (dark grey line) led to a more impactful reduction in lens thickness change (4.28%).

Applying a severe degeneration in all zonular sets (dashed grey line) led to the most prominent discrepancy in lens thickness variation. When comparing the severe dialysis of two ($ZA + ZE$) and three ($ZA + ZE + ZP$) zonular sets, one can observe that the lens thickness variation of the model with 90 degrees of dialysis in the three sets of zonules was equivalent to the model with 180 degree severe dialysis of the anterior and equatorial sets of zonules. As such, when accounting the additional posterior zonule dialysis, the reduction of thickness change becomes much more significative since, from then on, as the disrupted clock-hours of $ZA + ZE + ZP$ increased, the disaccommodation led to increasingly smaller values of lens thickness variation (180 degrees - 4.90%, 270 degrees - 3.07%). The lens with three sets of fully afflicted zonules could only vary in thickness a percentage amount of $\Delta T_L = 1.42\%$, a most significant decrease from the healthy model, accounting for a $\Delta T_L = 13.35\%$ value of thickness variation.

Lens radius variation

The variation of the lens equator radius was also taken into consideration, and the results found for this quantity are portrayed in Figure 4.12. Similarly to the results found for the lens thickness variation, the progression of zonular dialysis leads to a decrease in the lenticular capacity to change its radial dimension.

The analysis of the equatorial fibers revealed that, contrarily to the analysis of the lens thickness variation, the equatorial zonules play now an important role in the variation of the lens equator radius. This is due to the location of the equatorial fibers i.e., in the plane of the equator of the lens, where its radius is measured. Therefore, the weakening of the equatorial fibers leads to a smaller deformation of the lens in this region, which can be directly measured by the lens radius variation quantity.

As such, this set of fibers has a greater impact in the lens radius variation than the other two individual sets of zonules, ZA and ZP.

The moderate zonular disruption of all the considered zonular sets (ZA, ZE, ZP, $ZA + ZE$, $ZA + ZE + ZP$), does not have a great impact in the radius variation of the lens, even when applied to the complete structure of the zonules (360 degrees). For the three sets of zonules, when moderately afflicted throughout their complete structures, the lens equator shows a variation of $\Delta R_L = 6.42\%$, a reduction

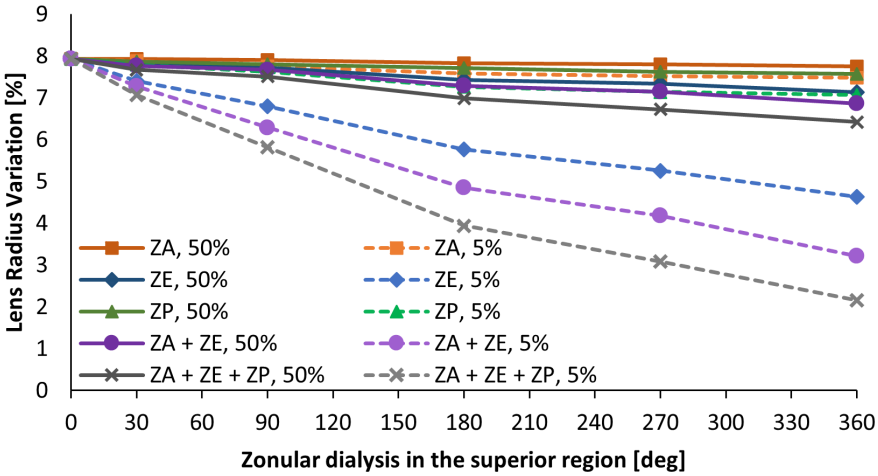

Figure 4.12: Lens radius variation for pseudoexfoliative models with initial superior dialysis.

of 1.52% from the value found for the healthy model.

For the case of severe dialysis of the fibers, both the anterior and posterior zonules, when considered individually, show no effect in the radius variation of the lens.

Nonetheless, the severe disruption of the equatorial fibers denotes a greater variation in the lens radius variation. When disrupted in the 12 clock-hours, the lens radius variation presents a value of only $\Delta R_L = 4.64\%$, as opposed to the value found for the healthy model ($\Delta R_L = 7.94\%$).

Considering the severe disruption of the two most anterior sets of zonules ($ZA + ZE$) throughout their structures, the final radius change of the lens accounts for $\Delta R_L = 3.22\%$, whereas the equivalent disruption of the three sets of zonules accounts for a final value of $\Delta R_L = 2.15\%$.

Amplitude of Accommodation

The accommodative capacity of the human lens, when subjected to pseudoexfoliative conditions, is of extreme importance when evaluating the clinical visual capability of the lens. The results found for the accommodation amplitude of the diseased lenses can be observed in Figure 4.13, for cases of superior dialysis.

When evaluating the singular impact of the equatorial zonules in the accommodative capacity of the lens, one can recognize that both when moderately and severely dialysed, the amplitude of accommodation attained by the lens shows no significant reduction for all cases of dialysis extent (30, 90, 180, 270 and 360 degrees).

The same cannot be said for the individual behavior of the posterior zonule. For the case of the moderately impaired posterior fibers, the amplitude of accommodation descents somewhat constantly when the degree of dialysis increases, up to the whole dialysis of the posterior zonules, leading to an accommodative capacity of $\Delta COP = 0.41D$. As for the case of the severe dialysis of the posterior zonules, the lens looses the capability of accommodation in a steeper slope according to the dialysis degree, encompassing 1.03 dioptres when dialysed in 30 degrees, 0.45 dioptres for the case of 90 degree degeneration, and abruptly reaching a value of 0 dioptres at 180 degree dialysis, which is never

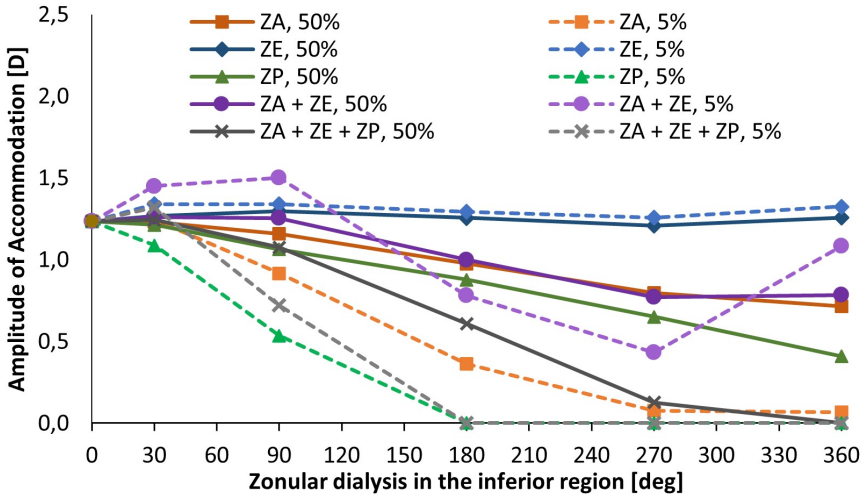

Figure 4.13: Amplitude of accommodation for pseudoexfoliative models with initial superior dialysis.

recuperated for cases with a greater degree of posterior dialysis.

Considering the singular performance of the dialysed anterior fibers, when moderately afflicted, show a reduction of the accommodation amplitude as the extension of dialysis increases, reaching a minimum value of $\Delta COP = 0.72D$ for the fully afflicted anterior fibers i.e., throughout their complete structure.

When the anterior zonule is severely dialysed in a 30 degree extension, the lens shows a much similar accommodative capacity as the moderate dialysis. Nonetheless, when the extension of the dialysis reaches greater magnitudes, the behavior of the lens with severely afflicted zonules shows much lower accommodative capabilities, with values of 0.86 dioptres and 0.34 dioptres for 90 and 180 degree zonulopathy, respectively, and reaching the minimum value at 270 degree dialysis ($\Delta COP = 0.07D$), which is then preserved in the 360 degree dialysis of the referred zonules.

The moderate dialysis of the three zonular sets leads to the most acute reduction of accommodative amplitude in the models with 50% zonular thickness. The accommodation amplitude decreases significantly when increasing the dialysis degree, reaching a value of 0.08 dioptres in the case with 270 degree dialysis, and 0 dioptres when all zonular sets are completely disrupted. As for the case of the severe dialysis of the three sets of zonules, the lens completely looses the ability to accommodate when the dialysis extent reaches 180 degrees.

When assessing the results found for the dialysis of the group of anterior and equatorial fibers, the values obtained for the moderately afflicted sets of zonules demonstrate an analogous behavior to the moderate disruption of the anterior zonules, showing once more, the lesser role that the equatorial fibers play in the accommodative capacity of the lens when moderately dialysed.

However, when analyzing the outcomes obtained for the severely disrupted group of equatorial and anterior zonules, the lens amplitude of accommodation shows an atypical behavior, when compared to the rest of the data obtained. For the 30 and 90 degree severe dialysis of the group of zonules, the values obtained for the accommodation amplitude were 1.42 and 1.49 dioptres, respectively. With a greater extent of fiber disruption, the values found for 180 degree and 270 degree dialysis were 0.81 and 0.48 dioptres. Finally, for dialysis in the whole structure of the anterior and equatorial fibers, the resulting

amplitude of accommodation was 1.08 dioptres.

Taking these results into account, the rationale that best accords with these values would be that the behavior of the 180 and 270 degree dialysis would be more in line with the results found for the rest of the data obtained throughout the degeneration models, since the accommodation amplitude increase of the 30 and 90 degree dialysed models has no clinical significance, and the final increase of accommodative capacity from 0.48 dioptres at 270 degree to 1.08 dioptres at 360 degree also portrays an irregular occurrence.

In order to understand the underlying factors that can have an influence in the anomalous behavior of the severely disrupted group of anterior and equatorial fibers, the non-constant variables in Equation 2.1 must be assessed (anterior and posterior radii of curvature of the lens, and lens thickness).

Regarding the lens thickness change in the models, the results found in Figure 4.11 show that the thickness variation decreases linearly with a greater extent of severe dialysis of the anterior and equatorial fibers, which is in accordance with the expected behavior of the lens, given that this behavior is observed for all the other cases of zonulopathy.

The anterior and posterior radii of curvature evolutions obtained for the models are shown in Figures 4.14a and 4.14b. In these figures, each line represents the evolution of the anterior and posterior radii of curvature throughout the deformation of each of the modelled lenses represented in the circular markers of the dashed purple line of Figure 4.13.

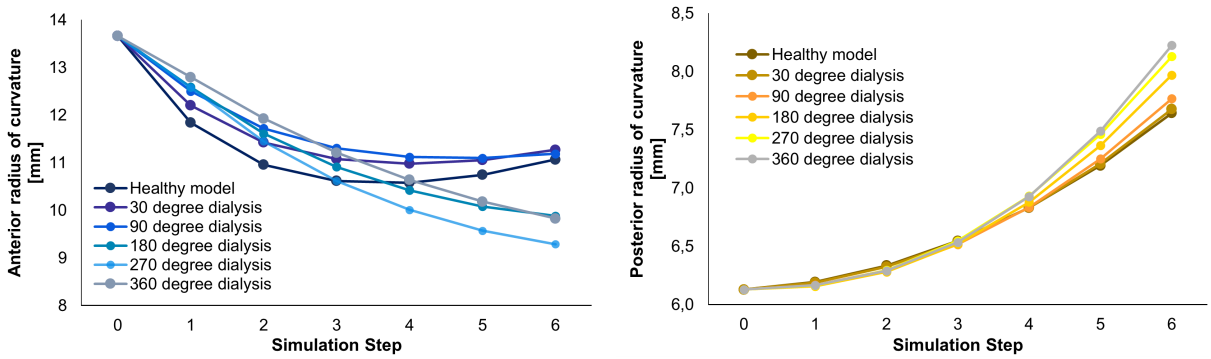

(a) (b)

Figure 4.14: Radii of curvature of the models with severe dialysis of the anterior and equatorial zonules. (a) Anterior radius of curvature. (b) Posterior radius of curvature.

The evaluation of the values of the posterior radii of curvature shows that, as the zonular dialysis extension increases, the posterior radius of curvature is able to obtain higher final values. For the healthy lens, the value for the posterior radius of curvature in the accommodated state is $r_p = 6.13mm$, attaining a value of $r_p = 7.64mm$ in the relaxed state. Nonetheless, the lens with 12 clock-hour severely disrupted anterior and equatorial zonules reaches a value of $r_p = 8.22mm$ for the disaccommodated stated of the lens (for the same value in the initial state as the healthy lens).

This behavior comes in line with the hypothesis that, since the posterior fibers are in a healthy state, contrarily to the anterior and equatorial ones, the displacement exacted by the posterior fibers allows for the increase of the posterior surface curvature with the progression of the models (since there is a lack

of anterior and equatorial fibers to counteract a greater deformation of the posterior surface of the lens).

As for the anterior radius of curvature, as the extent of dialysis increases, the trend of the slopes does not show a consistent evolution. With the lack of some of the supporting fibers, the behavior of the anterior surface of the lens became atypical, as can be seen in Figure 4.14a.

The models with 30 and 90 degree dialysis, show a similar behavior as the one attained by the healthy lens. Models with 180 and 270 degree dialysis show a downward slope of the anterior radius of curvature throughout the deformation of the lens. Consequently, the deformation of the anterior surface of the lens cannot follow the displacement acted by the anterior fibers, having a greater influence from the healthy posterior fibers, which can lead to the reduction of the anterior radius of curvature throughout the deformation of the lens.

This leads to the deduction that although the 30 and 90 degree lenses can maintain the behavior of the anterior surface curvature similar to the one of the healthy model, they can no longer counteract the behavior of the posterior surface of the lens which is being imposed by the healthy posterior fibers. As such, this leads to the abnormal increase of the amplitude of accommodation of the lenses, which can be observed also with the evolution of the Central Optical Power, portrayed in Figure 4.15. Taking into account the fact that the slopes of the radii of curvature of the 360 severe dialysis case show the same trend as the 30 and 90 degree cases, the same deduction can be applied to this case.

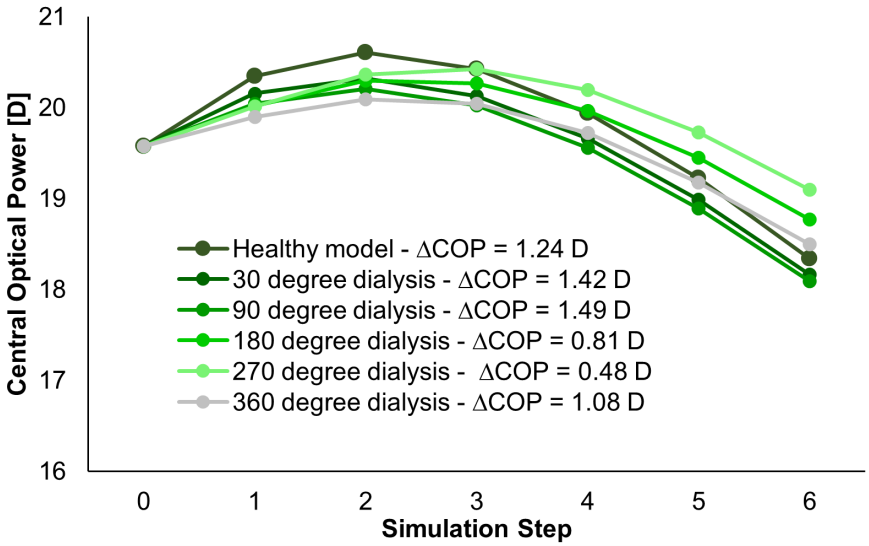

Figure 4.15: Central Optical Power of models with severely dialysed anterior and equatorial zonules.

Nevertheless, the results found for the amplitude of accommodation of the lens show that the behavior found for this case group of dialysis is in fact an outlier, given that all the other cases of dialysis show a gradual reduction of the accommodation amplitude of the lens.

These results show that, when it comes to the individual role of the zonular sets, the posterior zonules portray the most important role in the accommodative capacity of the lens, being then followed by the anterior zonular fibers, and finally the equatorial ones, which do not play an important part in the change of the curvatures of the lens when moderately or severely afflicted.

Overall, the values found for the accommodation amplitude evolution with the progression of the

pseudoexfoliation syndrome are aligned with the findings of Yavas et al. (2009), that denoted an accommodative deficiency in eyes with pseudoexfoliation syndrome. Nevertheless, the estimation of the authors did not quantify the degree of pseudoexfoliation of the involved eyes.

Total Zonular force

The results found for the total force endured by the zonules during the deformation of the lens can be observed in Figure 4.16. All types of degeneration showed a downward slope in the resulting zonular force, as the extension of dialysis progressed from 30 degrees upwards.

Similarly to the outcomes found for accommodation amplitude and lens thickness, the results found for the total force endured by the zonules show that the equatorial fibers do not play an important part in this quantity. For 12 clock-hour moderate and severe dialysis of the equatorial fibers, the resulting zonular force had values of $F_Z = 105.9mN$ and $F_Z = 100.8mN$, respectively, denoting a non-significant variation from the healthy model's zonular force value ($F_Z = 112.1mN$), when compared with the other cases of zonulopathy.

The moderate dialysis of the anterior zonules also had no significant impact in the total zonular force, as was the case of the moderate degeneration of the posterior zonules. Nonetheless, for the cases of severe disruption of the anterior fibers, a greater extension of dialysis led to a reduction of the total zonular force, reaching a value of $F_Z = 82.7mN$. This value is equivalent to a reduction of 26.2% from the healthy model's resulting zonular force. The severe dialysis of the posterior zonules led to a similar trend, leading to a value of $F_Z = 78.2mN$, correspondent to the 12 clock-hour severe disruption of the posterior fibers.

Note that, for all the cases of 30 degree disruption of the zonular fibers except for the singular analysis of the posterior zonules, there was a slight increase of the total zonular force (from the healthy model), up to $\Delta F_Z = 1.4mN$. Although this variation shows a negligible increase in the total force, the reasoning behind this value was investigated since the total zonular force should decrease with the imposition of zonular dialysis, as can be seen for greater extensions of dialysis (90 degrees and upwards).

As such, the zonular force of models with moderate dialysis of the three sets of zonular fibers was assessed. Figure 4.17 represents the zonular force endured by the anterior zonular fibers for models represented in the cross-shaped markers of the dark grey line in Figure 4.16.

Starting from the healthy model, with an initial value of $F_Z = 112.1mN$ for the total zonular force, this value increases with 30 degree moderate dialysis of all three sets of fibers ($F_Z = 113.5mN$), decreasing from then on for dialysis extensions of 90 degrees ($F_Z = 108.7mN$), 180 degrees ($F_Z = 100.4mN$), 270 degrees ($F_Z = 89.4mN$) and 360 degrees ($F_Z = 73.1mN$).

The zonular force due to the displacement of the fibers has a greater value in the exterior edge of the zonules, since this is the location of the boundary condition enforced on the fibers. As can be seen in the 30 degree dialysis representation of the force in the posterior zonules, the discontinuity imposed between healthy and afflicted areas of zonules, leads to an increase of zonular force in the joining edge between the two regions. This is a numerical effect, where the stretching of the outer edge of the fibers leads to the stretching of the transitional edge between healthy and diseased areas, leading to the

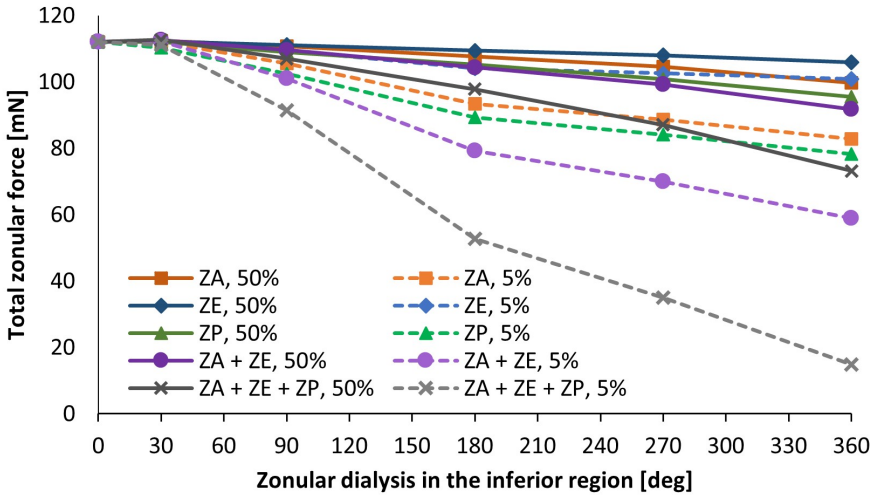

Figure 4.16: Total zonular force for pseudoexfoliative models with initial superior dialysis.

previously mentioned total zonular force increase.

Additionally, for the cases where there were both healthy and diseased zonular regions, an increase of force in the interior region of the zonule can be observed, proximal to the discontinuity regions. These two types of zonular force increment led to a slight increase of the total resulting force in the zonules with smaller regions of degeneration (30 degrees).

As for the case of the severe dialysis, instead of two separation edges between regions, there are four, which leads to a similar situation. The smaller force values acted in the severely disrupted region, and the transitional moderately disrupted areas are opposed by the force in the joining edges between the disrupted and healthy regions, leading to a balance in the total zonular force for 30 degree dialysis cases.

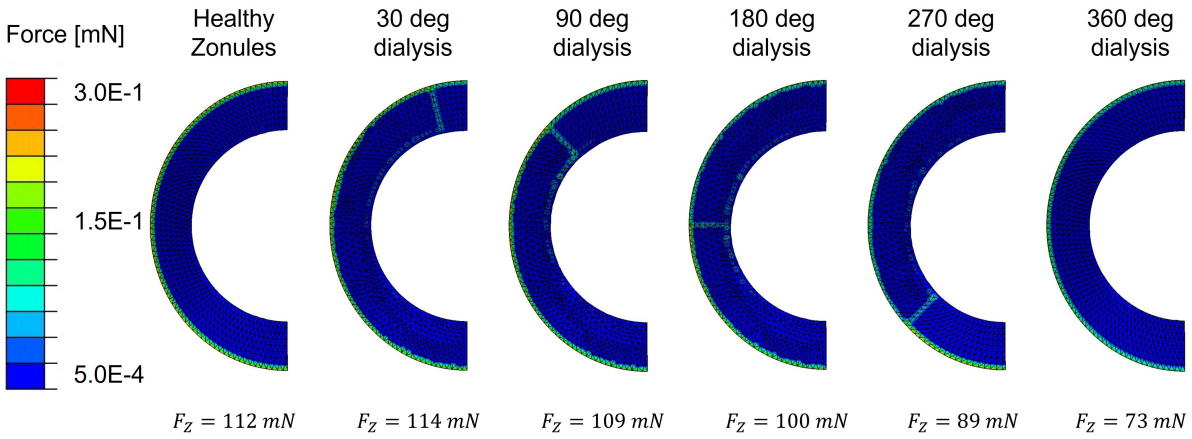

Figure 4.17: Zonular force configuration of the posterior zonules for models depicting moderate dialysis of the three sets of fibers.

For cases with greater dialysis extension, this balance is no longer achieved, since the growth of the diseased region leads to a smaller total zonular force.

Capsular bag average stress

When assessing the stress endured by the lens capsule, the average Von-Mises stress was taken into consideration and the values obtained for the pseudoexfoliative models are depicted in Figure 4.18.

As portrayed in this figure, the moderate disruption of each of the zonules (ZA, ZE and ZP) led to a small decrease of the average stress endured by the capsule. The most extreme of the cases was for the moderate disruption of the anterior zonules, that led to a resulting average stress in the capsule of $\overline{VM_{CB}} = 64.7kPa$, for 360 degree dialysis.

The analysis of cases with severe zonulopathy led to the following deductions: the equatorial zonules are the ones with the lowest impact in this quantity, followed by the posterior zonules. The anterior zonules are the ones that, individually, cause the capsular bag to endure the smallest value of average Von-Mises stress in conditions of severe dialysis. As for the case of the zonular set groups ($ZA + ZE$ and $ZA + ZE + ZP$), the severe dialysis of these assemblies led to the biggest difference in terms of capsular bag average stress.

The curve denoting a severe disruption of the anterior and equatorial fibers had a downward slope throughout the extension progression of dialysis, although more pronounced for the first 180 degrees of extension. From then on, the slope showed a more lenient inclination, and at 360 degrees dialysis, the average stress endured by the model with zonulopathy of anterior and equatorial fibers was $\overline{VM_{CB}} = 35.0kPa$.

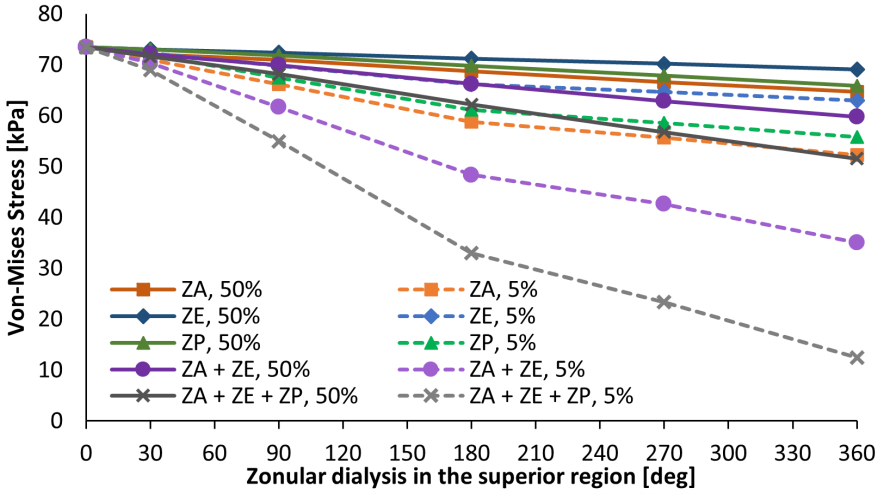

Figure 4.18: Average Von-Mises stress in the capsular bag for models with initial superior dialysis.

The curve referring to the dialysis of the three sets of fibers had the same trend as the previously mentioned assembly, and the resulting average stress in the capsular bag amounted to only $\overline{VM_{CB}} = 12.4kPa$ for 360 degree dialysis, a reduction of 83.1% from the healthy value found for this quantity, $\overline{VM_{CB}} = 73.4kPa$.

The curves displayed in Figure 4.18 relate directly to the averaged amount of stress that the capsular bag endures for different types of pseudoexfoliative conditions. From these results, one notes that due to the deteriorated conditions of the zonules, their stretching does not cause the same deformation on the capsule, which then translates to a reduction of the amount of stress that the capsule is under. Since the

areas of greater stress in the capsule are the attachment regions to the anterior, equatorial and posterior zonular fibers, as these components are thinned, the same displacement of the remaining fibers does not cause the same behavior in the capsule, leading to the reduction of Von-Mises average stress that the component endures.

Stress endured by the zonules

The maximum value of Von-Mises stress that the zonules endure during disaccommodation of the lens is depicted in Figure 4.19.

Overall, the results found for the moderate disruption of the fibers showed no significant increase of the maximum stress endured by the zonules, $max(VM_Z)$. Notably, the maximum value of the Von-Mises stress for moderate zonulopathy, was related to the dialysis of the three sets of zonules, with 180 degrees extension, totalling a value of $max(VM_Z) = 269kPa$, a result that showed an increase from the healthy model's value of $125kPa$.

Nonetheless, the models that accounted for severe dialysis of the zonules all showed a significant increase of the maximum zonular stress, with the exception of the equatorial zonules.

Accordingly, the individual disruption of the anterior fibers showed a similar behavior to the one of the individual posterior fibers, where there was a increase of the maximum stress endured by the zonules up to 270 degree dialysis extension, followed by a reduction from the forementioned cases to the ones with 360 degree dialysis.

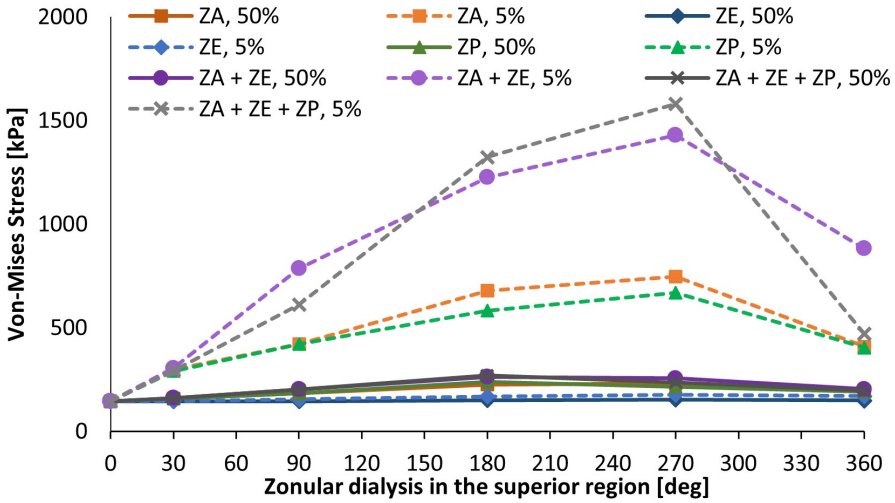

Figure 4.19: Maximum Von-Mises stress in the zonules for models with initial superior dialysis.

The same results were found for the cases of dialysis of the groups of zonules ($ZA + ZE$ and $ZA + ZE + ZP$), where an increase of stress was observed up to 270 degree dialysis extension, and a reduction observed for the dialysis of the whole structure. For the case of the severe disruption of the anterior and equatorial zonules, the maximum Von-Mises stress for 270 degree and 360 degree zonulopathy extensions was valued $max(VM_Z) = 1429kPa$ and $max(VM_Z) = 881kPa$, respectively. As for the case of severe disruption of the three sets of zonules, the values obtained for 9 and 12 clock-hours were $max(VM_Z) = 1581kPa$ and $max(VM_Z) = 470kPa$, correspondingly.

When examining the zonular areas that endured the greater amount of stress when under pseudoexfoliative conditions, the case of severe disruption of the anterior zonules was analyzed, for 90 degree extension, since this case still had the presence of healthy zonules, as per Figure 3.10. The Von-Mises stress distribution on the anterior zonules is depicted in Figure 4.20, where the edges that mark the separation between the different healthy and diseased regions are depicted with wider black lines.

As can be seen in the referred figure, the 90 degree region with severe disruption of the zonular fibers, where $T_Z = 0.5\mu m$, is the one that endures the greater amount of stress, in particular, in the area proximal to the capsular bag attachment. The areas of moderate disruption on both sides show a reduction of the stress endured, when compared with the severely damaged region. Lastly, the healthy region of zonules had the smallest amount of stress concentration. Nonetheless, the healthy region denotes a greater stress concentration in the areas closer to the moderately dialysed regions.

These results suggest that the stress endured by the diseased regions propagates to the healthy zonules, which then causes a progression of the degeneration, given that the latter fibers are now under a greater amount of stress that expected in healthy conditions.

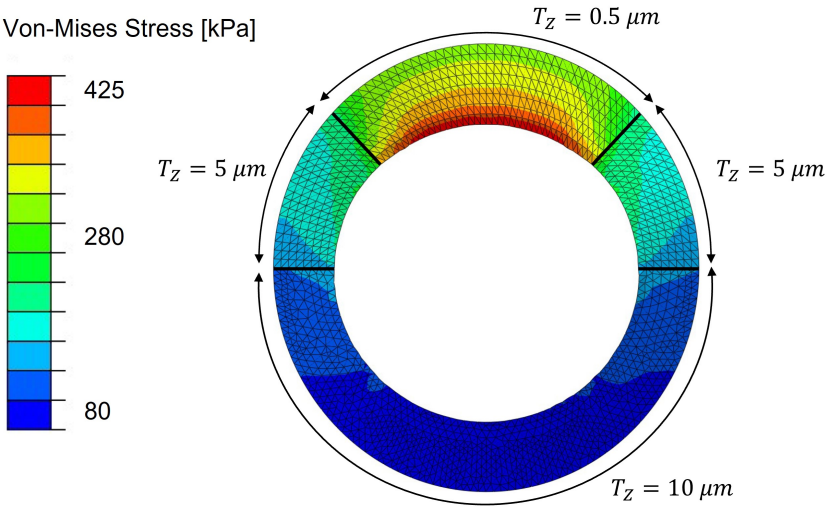

Figure 4.20: Von-Mises stress distribution for the case of severe 90 degree dialysis of the anterior zonules.

Stress endured by the cortex and nucleus

The maximum Von-Mises stress is analyzed together for the cortex and nucleus, $max(VM_{C+N})$, and the resulting values of the endured stress by the lenticular components are represented in Figure 4.21.

The referred figure denotes an overall reduction of the stress endured by the cortex and nucleus, as the pseudoexfoliation syndrome evolves and reaches more advanced stages.

The analysis of the equatorial fiber disruption shows that although the moderate dialysis does not cause a significant decrease in the stress endured by the lens, the severe zonulopathy of the equatorial zonules has one of the most significant impacts in the stress reduction endured by these components.

The anterior zonule disruption has an inverse effect in the cortical and nuclear stress, since its dialysis leads to an increase of the resulting maximum stress.

Nonetheless, the dialysis of the posterior zonules shows no significant impact in the cortical and nuclear maximum Von-Mises stress, being that the stress values are $max(VM_{C+N}) = 0.204kPa$ for both the moderately and severely dialysed posterior fibers, in a 360 degree extension.

When analyzing the groups of anterior and equatorial zonules, their behavior shows a similar trend to the one where only the equatorial fibers were disrupted. The same behavior similarity between ZE and $ZA + ZE$ is also visible when comparing their severe disruptions, with the addition that the behavior of the equatorial zonules, when individually considered, causes a slightly more severe reduction of stress in the lens than the sets of equatorial and anterior fibers considered together.

These results, show once again that the dialysis of the anterior fibers causes an increase of the cortical and nuclear maximum Von-Mises stress, a trend that is observed only for this set of fibers.

Finally, the analysis of the three zonules shows a similar behavior to the one observed by the disruption of the anterior and equatorial sets of zonules, up to the level of 270 degree of dialysis extension. For the case of 360 degree of dialysis of $ZA + ZE + ZP$, there is an abrupt reduction of the maximum Von-Mises stress in the lens, reaching only a value of $max(VM_{C+N}) = 0.081kPa$.

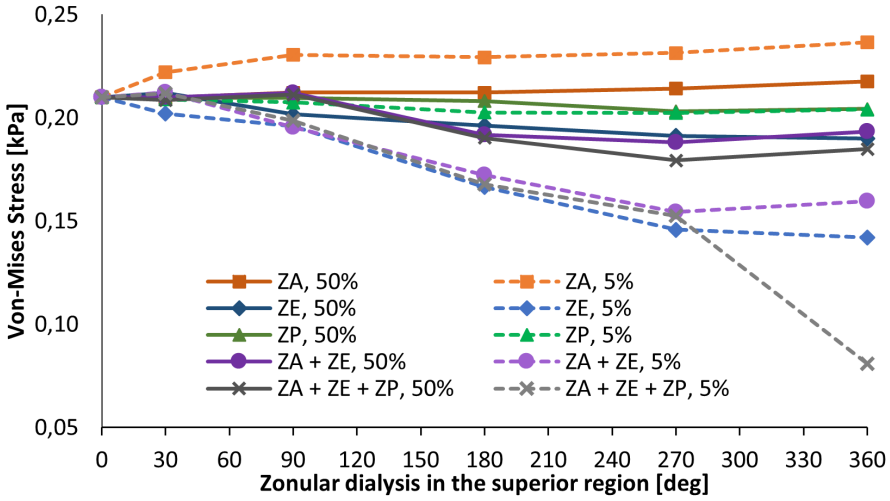

Figure 4.21: Maximum Von-Mises stress in the cortex and nucleus for models with initial superior dialysis.

Comparison between superior and inferior dialysis

As previously mentioned, the information related to models with an inferior dialysis origin is portrayed in Appendix C, where the results found for the lens thickness and radius variations, zonular force, average capsular Von-Mises stress and maximum zonular and lenticular Von-Mises stress are represented.

In order to understand the relevant disparities between the two groups of models (with inferior and superior dialysis), an approximation error was computed between superior and analogous inferior models, resorting to Equation 4.2.

$$\lambda[\%] = \frac{value_{inf} - value_{sup}}{value_{sup}} \cdot 100 \tag{4.2}$$

Note that the presented variable can have negative values: when the referred value for the inferior dialysis is smaller than the superior one, λ has a negative value, in order to highlight this behavior.

The results found for the lens thickness variation showed a negligible difference between values with superior and inferior origins. The case where the lens thickness variation disparity was greater was for the severe disruption of the three sets of zonular fibers, with 180 degree extension, where the superior dialysis case had a resulting thickness variation of $\Delta T_L = 4.82\%$, whereas the inferior case had $\Delta T_L = 4.90\%$, leading to a percentage difference of 0.08%.

Similarly to the lens thickness variation measurements, the discrepancy between superior and inferior lens radius variations was not significant.

The total zonular force had higher values for all the cases where there was a superior dialysis i.e., the approximation error had negative values for all the comparisons between inferior and superior cases. The average approximation error was $\overline{\lambda} = -1.6\%$. The most extreme case, where $\lambda = -10.0\%$, occurred for the severe 270 degree dialysis of all the zonular sets. For this case, the superior dialysis had a value of $F_Z = 38.8mN$, whereas the total zonular force for the inferior case was $F_Z = 34.9mN$.

These results show that when there is a degeneration with a superior origin, the zonular fibers endured a greater amount of force when achieving the same displacement as an analogous lens complex with inferior zonulopathy.

The evaluation of the capsule's average Von-Mises stress did not denote a significant difference between the two types of cases: the average approximation error was valued $\overline{\lambda} = -0.2\%$, ranging from $\lambda = -2.5\%$ to $\lambda = 1.0\%$, for all the models designed.

The most important differences between the two types of degeneration were observed in the maximum Von-Mises stress endured by the zonules, the maximum Von-Mises stress endured by the lenticular components and last but not least, the accommodation amplitude. Accordingly, the average values of the errors of approximation for these quantities can be observed in Figure 4.22, for the different designed zonular sets of dialysis.

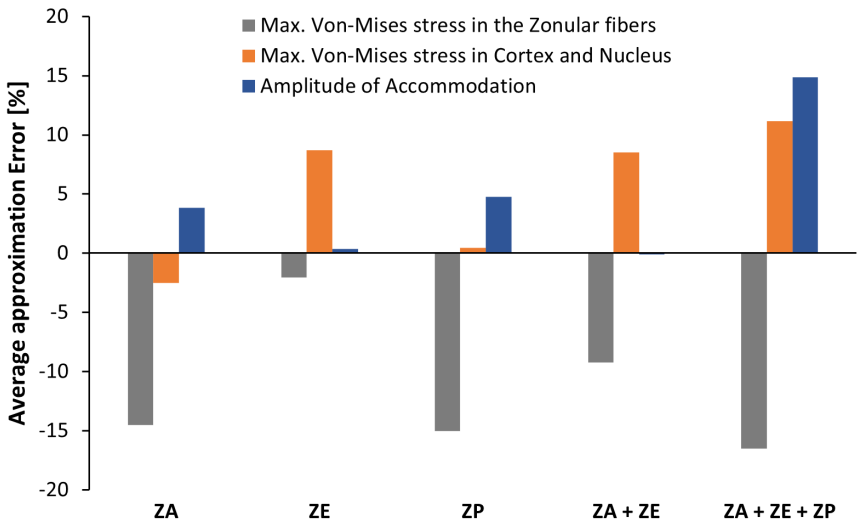

Figure 4.22: Comparison between superior and inferior values for maximum Von-Mises stress in the zonules, in the lens, and amplitude of accommodation.

The reasoning for the approximation error evaluation, concerning the dialysis of the different zonular sets has to do with the disparity of behaviors that each set produced.

The first examined quantity that showed a significant discrepancy between inferior and superior dialysis was the maximum Von-Mises stress endured by the zonular fibers, represented in grey, in Figure 4.22. The average approximation error for each of the zonular groups considered (ZA, ZE, ZP, $ZA + ZE$ and $ZA + ZE + ZP$) denoted that the stress endured by models with superior dialysis origin endured a greater amount of stress than the analogous models with inferior dialysis origin, as defined by the negative values of $\overline{\lambda}$.

When considering the individual zonulopathy of the anterior and posterior zonules, the values found for the approximation error were $\overline{\lambda} = 14.5\%$ and $\overline{\lambda} = -15.0\%$, respectively. These values show a significant discrepancy between the superior and inferior dialysis.

For the case of the dialysis of the equatorial fibers, the difference was less significant ($\lambda = -2.1\%$). Nonetheless, as previously mentioned, these fibers did not have a significant impact in the Von-Mises stress endured by the three groups of zonules.

The assessment of the groups of zonules, $ZA + ZE$ and $ZA + ZE + ZP$, led to the approximation error values of $\overline{\lambda} = -9.2\%$ and $\overline{\lambda} = -16.5\%$, respectively.

These results imply that the zonulopathy causes a greater amount of stress in the zonules when its origin has a superior location. Consequently, since the healthy zonular fibers suffer a greater disruption as the stress magnitude increases, the same fibers would be under a greater degeneration when in the presence of a superior dialysis, when compared with the analogous case of inferior dialysis.

The analysis disparity between the superior and inferior values of the maximum Von-Mises stress in the cortical and nuclear components of the lens is also depicted in Figure 4.22.

The anterior zonular fiber disruption showed a peculiar behavior, when compared with the rest of the zonular sets: the average approximation error between superior and inferior values was valued as $\overline{\lambda} = -2.5\%$, denoting that the superior dialysis caused a greater stress in the cortex and nucleus than the inferior dialysis. However, all the other sets had an opposite behavior, where the average approximation error was positive, showing a greater stress in the models with inferior dialysis than models with a superior one. Accordingly, the values found for the different zonular sets were:

- $\overline{\lambda} = 8.7\%$ for degeneration of the equatorial fibers.

- The posterior fiber disruption showed the smallest approximation error magnitude, $\overline{\lambda} = 0.5\%$, denoting a non-significant discrepancy between inferior and superior dialysis values. This is related to the fact that the posterior fiber dialysis showed no impact in the variation of the cortical and nuclear maximum Von-Mises stress, as can be observed in Figure 4.21.

- The value obtained for the average approximation error was $\overline{\lambda} = 8.7\%$ for the disruption of the anterior and equatorial zonules, and the corresponding value for the three sets of zonules was $\overline{\lambda} = 11.2\%$, showing the biggest disparity between the obtained values for inferior and superior dialysis.

Last but not least, the impact on the amplitude of accommodation was compared between inferior and superior dialysis for the different zonular fiber evaluations (as depicted in blue, Figure 4.22).

The equatorial fibers, given that they have no significant impact in the accommodative capacity of the lens, as can be observed in Figure 4.13, did not present a significant difference between the inferior and superior dialysis values, given that their approximation error was $\overline{\lambda} = 0.4\%$.

Nonetheless, the anterior and posterior zonules, when analyzed individually, led to the average approximation errors $\overline{\lambda} = 3.8\%$ and $\overline{\lambda} = 4.8\%$, respectively.

The behavior of the anterior and equatorial zonular dialysis shows no significant disparity between inferior and superior values, given that $\overline{\lambda} = -0.1\%$.

Finally, the most significant disparity encountered was for the zonulopathy of the three sets of fibers, where $\overline{\lambda} = 14.9\%$. For this group of models, the maximum values of λ were the cases of the moderate disruption of the zonules with 270 degree extension $\lambda = 60.1\%$, and the severe disruption with 90 degrees extension $\lambda = 23.0\%$, whereas the minimum value was $\lambda = 0$, for the cases of disruption where the accommodation amplitude of the lens was 0 dioptres, both for the inferior and superior cases of dialysis.

The results found for both the maximum Von-Mises stress in the zonules and the accommodation amplitude of the lens point to the same conclusion, that the superior dialysis leads to a most severe degeneration of the zonules and the visual capacity of the lens. This is due to the two fore-mentioned factors:

- The inferior dialysis leads to a less severe reduction of the accommodation amplitude of the lens.
- The inferior dialysis presents smaller stress magnitudes in the zonules, which then leads to a less severe progression of the zonulopathy condition.

For further analysis of the results found for the approximation error, its calculations are presented in Appendix C, Tables C.2–C.7. Additionally, the results found for all the models depicting the pseudoexfoliation syndrome can be observed in Appendix C, Table C.9 and C.10.

Chapter 5

Conclusions

In this dissertation one can learn the biomechanical impact of the pseudoexfoliation syndrome in the human lens complex. The work developed progressed from being able to understand and apply the state of the art in this field, by developing the healthy lens model, to establishing the most advanced and complete model for zonulopathy conditions.

The main objective of this work was to address the challenge of determining the biomechanical and optical behavior of the human lens complex under healthy and diseased conditions.

The first part of this goal involved the construction and validation of *in silico* experiments concerning the healthy human lens and its surrounding structures.

This was also possible due to the development of a measurement methodology of the dioptric power of the crystalline lens throughout its deformation, by means of the calculation of the accommodation amplitude (ΔCOP). This method was proposed and validated, resorting to available literature data. This is a measurement that is also attainable in a clinical setup.

Accordingly, the initial model, constructed with the basis of the available literature data, was developed taking into account the geometry of a 62 year-old lens, given that this age is within the age range of the pseudoexfoliation syndrome.

This initial validation then led to the design of a novel 3D model for the healthy lens complex, where the biomechanical effects of both geometrical changes in the zonular fibers and the boundary conditions of the capsular bag were assessed. As such, the approaches towards the refinement of the initial model, led to the following conclusions:

- The variation of the assessed geometrical parameters of the zonules, where the vertical length of the fibers can be up to 5.6% greater than the horizontal one, contributed to the development of four models. As such, the outcomes of this study were that for the model with greatest average fiber length, $\overline{l_Z}$, the accommodative capacity of the 62 year-old lens reaches values that are in a greater accordance with the literature analyzed, $\Delta COP = 1.38D$. The same applies to the total zonular force for this model, $F_Z = 129.9mN$, given that this value is smaller than the one of the initial model ($F_Z = 134.1mN$) and, consequently, closer to literature values.

- The assessment of the boundary conditions of the capsular bag, where the anchorage regions to

the zonules were altered, led to the conclusion that when there is a zero-width insertion ring as the surface of attachment to the capsule, the values of force and accommodative amplitude are greater than for the cases where the capsule has bands of insertion with width greater than zero. As a matter of fact, the behavior of the lens remains practically unaltered for different widths of capsule anchorage bands, except for the case of zero-width insertion rings. The total force value presented for the chosen case with insertion bands in the capsule amounted to $F_Z = 113.7mN$, whereas the accommodative amplitude was valued as $\Delta COP = 1.33D$.

For the final assessment of the healthy lens, the refined model was subjected to gravity conditions. The results found for the evaluation of the impact of gravity in the lens complex revealed that there is a stress redistribution in the lenticular components, where the superior portions of both the nucleus and cortex are under a greater amount of stress than the inferior ones. Nonetheless, the stress magnitude endured by the lens both with and without gravity was virtually the same.

The second part of the objective defined was the analysis of the biomechanical behavior of the lens under diseased conditions, in particular, due to the pseudoexfoliation syndrome.

The subject of zonulopathy underwent a thorough numerical investigation and evaluation, due to the construction of several pseudoexfoliative models that implemented a gradual and progressive degeneration of various groups of zonular sets, under several types of dialysis extension and different severity disruptions. As such, the zonulopathy caused by this syndrome was progressively applied to the zonular fibers, in order to understand the advancement of the disease, as well as the implications that it might have in the lens complex, both from a biomechanical perspective and an optical one.

When ascertaining the impact that each group of zonules had in the different measured quantities, the results portraying the accommodative capacity of the lens show that the equatorial zonules do not have a significant impact in the lens accommodation process. The same cannot be said for the anterior and posterior zonules, when considered individually, whose dialysis leads to a severe reduction of the accommodative amplitude of the lens, even in moderate pseudoexfoliation conditions (from the healthy value of $\Delta COP = 1.24D$, to $\Delta COP = 0.72D$ for the case of 12 clock-hour moderate dialysis of the anterior zonules). With the progression of the disease in the anterio-posterior direction, the accommodative capability becomes even more deficient, given that the moderate disruption of 12 clock-hours of the anterior and equatorial zonules leads to a amplitude of accommodation of 0.78 dioptres, whereas the three sets of moderately disrupted lead to the complete loss of the accommodative capacity, where $\Delta COP = 0D$.

The results found for the lens thickness variation denoted the same trend as the accommodative capacity, given that the equatorial zonules did not have an impact on this quantity. On the contrary, the lens radius variation loss was prominent with the weakening of the equatorial zonules. When considering dialysis of the anterior and equatorial zonules, and the group of three sets of zonules, all the formentioned quantities showed a significant decrease, since the disruption was spread through several zonular sets, instead of just one.

As the progression of the disease increased, the force acted on the zonules during the disaccommodation process reduced significantly, given that for the same stretching input, the weakened fibers were

no longer able to sustain the same effort. From a healthy value of $F_Z = 112.1mN$ to the most acute case of zonulopathy, where the three sets of zonules were severely disrupted throughout their whole structures, there was a loss of 86.7% of the total force endured by the zonules ($F_Z = 14.9mN$).

Additionally, with the progression of the disease, the stress endured by the zonules increased significantly, reaching values up to 11 times higher for the maximum Von-Mises stress (from a healthy value of $144.25kPa$ to the most acute case of dialysis - 12 clock-hours of severe dialysis of the three zonules, $max(VM_Z) = 1581.00kPa$). The stress on the zonules increased in the diseased regions of the zonules, and this stress propagated to the healthier regions of the fibers, causing the healthy zonules to be under a greater amount of stress, which can then lead to a further propagation of the disease.

The results found for the comparison between inferior and superior dialysis showed that the location of the zonulopathy in the lens complex has a significant impact in the progression of the disease and the accommodative capacity of the lens. The superior dialysis presents optimal conditions to further the disruption of the fibers and reduce the accommodative amplitude of the lens, when compared with the inferior dialysis location. Accordingly, the accommodative capacity of the inferior models was, on average, 4.7% greater than for the cases with superior dialysis. When the three sets of zonules were disrupted, this discrepancy increased significantly, reaching an average value of 14.9% for the mentioned models, and with a maximum value of 60.1%.

The impact of the dialysis origin was also prominent in the stress endured by the zonules, given that for all the models with superior zonulopathy, there is a significantly higher stress intensity than for the case of inferior disruption. The increase of stress endured by the healthier zonules leads to a greater propagation of the dialysis in the fibers and, consequently, the zonular fibers with a superior dialysis sustain a greater risk of disruption than the inferior ones.

These results present a quantification of the visual accommodative capacity of a 62 year-old lens throughout the progression of the pseudoexfoliation disease, and break new ground in this subject, given the lack of experimental and clinical data concerning this syndrome.

Consequently, they become of great importance in the analysis of the severity of the pseudoexfoliation syndrome, given that they provide data in the context of the locations that present a greater risk to a surgeon when coming in contact with the human lens complex. Additionally, the amplitude of accommodation measurement of the afflicted eye presented by this dissertation becomes a valuable asset when estimating the severity of the syndrome in a patient, given that the accommodation amplitude can be obtained in a clinical setup.

5.1 Limitations and Future Work

The work presented in this dissertation led to the development of innovative data concerning the healthy lens complex configuration, as well as the pseudoexfoliation syndrome and its effect in the studied system.

Nonetheless, the lack of clinical, experimental and *in silico* data is a notable limitation of the work developed throughout this dissertation. Due to the variety of geometrical parameters and constitutive

modeling choices taken by each group of investigation in this matter, the results found by each author are not directly comparable.

Alongside this limitation is the lack of attainable *in vivo* data that gives the investigators a realistic scope of the movements that occur during the accommodation process, and other quantities that are extremely difficult to estimate, such as the force endured by the zonules during this process. Another limitation of the current work lies with the constitutive modeling of the lenticular system's structures, given that in reality, they do not have linear isotropic properties. In essence, the material properties found for all the structures, with the exception of the zonules, are in actuality, simplifications of the complex and anysotropic material properties that these structures have.

When it comes to the pseudoexfoliation syndrome, the research concerning this subject is becoming more prevalent due to the aging of the world-wide population. Nevertheless, the essential experimental data that would allow for a more complete constitutive model of the weakened zonules is lacking. Additionally, a quantification of the zonular fiber loss for different levels of the disease would provide a greater indication when ascertaining the severity of zonular dialysis.

In terms of the *in silico* models presented, the development of models that show an evolution of the zonule dialysis, where there is no longer a discontinuity between healthy and diseased regions, would allow for studies with a better physiological relevance.

As a future work, the comprehensive study involved in the knowledge gained towards the mentioned syndrome could also be applied to other diseases of the human lens complex, such as the formation of cataract in the crystalline lens. As mentioned in Section 1.1, a connection between the conditions of cataract and pseudoexfoliation has been found and, as such, the study of the overlap of these two conditions would also present a valuable future research towards this subject.

Finally, the methodology applied towards the construction of the models in this dissertation could also be applied for cases in post-surgical perspectives, such as cataract surgery, where the nucleus and cortex are removed and substituted by an intraocular lens.

Bibliography

Amigó, A. and Bonaque-González, S. (2016). Is the capsular bag perimeter round or elliptical? *Journal of ophthalmic & vision research*, 11(2):159.

Atchison, D. A., Smith, G., and Smith, G. (2000). *Optics of the human eye*, volume 2. Butterworth-Heinemann Oxford.

Bahrami, M., Heidari, A., and Pierscionek, B. K. (2016). Alteration in refractive index profile during accommodation based on mechanical modelling. *Biomedical optics express*, 7(1):99–110.

Belaidi, A. and Pierscionek, B. (2007). Modeling internal stress distributions in the human lens: can opponent theories coexist? *Journal of vision*, 7(11):1–1.

Besner, S., Scarcelli, G., Pineda, R., and Yun, S.-H. (2016). In vivo brillouin analysis of the aging crystalline lens. *Investigative ophthalmology & visual science*, 57(13):5093–5100.

Biermann, J., Bredow, L., Boehringer, D., and Reinhard, T. (2011). Evaluation of ciliary sulcus diameter using ultrasound biomicroscopy in emmetropic eyes and myopic eyes. *Journal of Cataract & Refractive Surgery*, 37(9):1686–1693.

Bocskai, Z. and Bojtár, I. (2013). Biomechanical modelling of the accommodation problem of human eye. *Periodica Polytechnica. Civil Engineering*, 57(1):3.

Burd, H., Judge, S., and Cross, J. (2002). Numerical modelling of the accommodating lens. *Vision research*, 42(18):2235–2251.

Burd, H. J., Judge, S. J., and Flavell, M. J. (1999). Mechanics of accommodation of the human eye. *Vision research*, 39(9):1591–1595.

Cardoso, T. (2018). Modelling of the human lens complex under cataract surgery. Master's thesis, Instituto Superior Técnico.

Castro, A. and Alves, J. (2020). Numerical implementation of an osmo-poro-visco-hyperelastic finite element solver: application to the intervertebral disc. *Computer Methods in Biomechanics and Biomedical Engineering*, pages 1–13.

Duane, A. (1922). Studies in monocular and binocular accommodation with their clinical applications. *American Journal of Ophthalmology*, 5(11):865–877.

Hayashi, K., Hirata, A., and Hayashi, H. (2007). Possible predisposing factors for in-the-bag and out-of-the-bag intraocular lens dislocation and outcomes of intraocular lens exchange surgery. *Ophthalmology*, 114(5):969–975.

Hermans, E., Dubbelman, M., Van der Heijde, G., and Heethaar, R. (2006). Estimating the external force acting on the human eye lens during accommodation by finite element modelling. *Vision Research*, 46(21):3642–3650.

Hermans, E., Dubbelman, M., Van der Heijde, G., and Heethaar, R. (2008). Change in the accommodative force on the lens of the human eye with age. *Vision Research*, 48(1):119–126.

Heys, K. R., Cram, S. L., and Truscott, R. J. (2004). Massive increase in the stiffness of the human lens nucleus with age: the basis for presbyopia?

Hoffman, R. S., Snyder, M. E., Devgan, U., Allen, Q. B., Yeoh, R., Braga-Mele, R., Committee, A. C. C., et al. (2013). Management of the subluxated crystalline lens. *Journal of Cataract & Refractive Surgery*, 39(12):1904–1915.

Holden, B. A., Fricke, T. R., Ho, S. M., Wong, R., Schlenther, G., Cronjé, S., Burnett, A., Papas, E., Naidoo, K. S., and Frick, K. D. (2008). Global vision impairment due to uncorrected presbyopia. *Archives of ophthalmology*, 126(12):1731–1739.

Holzapfel, G. A., Gasser, T. C., and Ogden, R. W. (2000). A new constitutive framework for arterial wall mechanics and a comparative study of material models. *Journal of elasticity and the physical science of solids*, 61(1):1–48.

Jud, L., Castro, A., Rúben, R., Feijóo, B., Ribeiro, F., and Fernandes, P. (to appear). Finite element modelling of the human eye crystalline complex under healthy and diseased conditions.

Khng, C. and Osher, R. H. (2008). Evaluation of the relationship between corneal diameter and lens diameter. *Journal of Cataract & Refractive Surgery*, 34(3):475–479.

Lanchares, E., Navarro, R., and Calvo, B. (2012). Hyperelastic modelling of the crystalline lens: Accommodation and presbyopia. *Journal of Optometry*, 5(3):110–120.

Liou, H.-L. and Brennan, N. A. (1997). Anatomically accurate, finite model eye for optical modeling. *JOSA A*, 14(8):1684–1695.

Naumann, G. O., Schlötzer-Schrehardt, U., and Küchle, M. (1998). Pseudoexfoliation syndrome for the comprehensive ophthalmologist: intraocular and systemic manifestations. *Ophthalmology*, 105(6):951–968.

Netter, F. H. (2010). *Atlas of Human Anatomy*. Elsevier Health Sciences.

Paulino, J. (2019). 3d biomechanical modelling of the human lens complex under cataract surgery. Master's thesis, Instituto Superior Técnico.

Pedrosa, C., Lisboa, M., and Prieto, I. (2016). Pseudoexfoliation: The diagnosis at first sight. *Hospital Prof. Dr. Fernando Fonseca*, 4(1/2):54–55.

Pierscionek, B., Bahrami, M., Hoshino, M., Uesugi, K., Regini, J., and Yagi, N. (2015). The eye lens: age-related trends and individual variations in refractive index and shape parameters. *Oncotarget*, 6(31):30532.

Ribeiro, F. (2019). *Presbiopia*. Sociedade Portuguesa de Oftalmologia, 1st edition.

Ribeiro, F., Ceia, P., and Jud, L. (to appear). Pseudophakic eye models. IOL Power Club.

Ritch, R. and Schlötzer-Schrehardt, U. (2001). Exfoliation syndrome. *Survey of ophthalmology*, 45(4):265–315.

Rosen, A. M., Denham, D. B., Fernandez, V., Borja, D., Ho, A., Manns, F., Parel, J.-M., and Augusteyn, R. C. (2006). In vitro dimensions and curvatures of human lenses. *Vision research*, 46(6-7):1002–1009.

Schlötzer-Schrehardt, U. and Naumann, G. O. (1994). A histopathologic study of zonular instability in pseudoexfoliation syndrome. *American journal of ophthalmology*, 118(6):730–743.

Schlötzer-Schrehardt, U. and Naumann, G. O. (2006). Ocular and systemic pseudoexfoliation syndrome. *American journal of ophthalmology*, 141(5):921–937.

Strenk, S. A., Semmlow, J. L., Strenk, L. M., Munoz, P., Gronlund-Jacob, J., and DeMarco, J. K. (1999). Age-related changes in human ciliary muscle and lens: a magnetic resonance imaging study. *Investigative ophthalmology & visual science*, 40(6):1162–1169.

Ungerer, J. (2000). The optometric management of presbyopic airline pilots. *Unpublished MSc Optometry thesis, University of Melbourne, cited in Atchison and Smith*.

Van Alphen, G. and Graebel, W. P. (1991). Elasticity of tissues involved in accommodation. *Vision Research*, 31(7-8):1417–1438.

Von Helmholtz, H. and Southall, J. P. (1924). Mechanism of accommodation.

Wang, K. and Pierscionek, B. K. (2019). Biomechanics of the human lens and accommodative system: Functional relevance to physiological states. *Progress in retinal and eye research*, 71:114–131.

Wang, K., Venetsanos, D., Wang, J., and Pierscionek, B. K. (2016). Gradient moduli lens models: how material properties and application of forces can affect deformation and distributions of stress. *Scientific reports*, 6(1):1–10.

Wang, K., Venetsanos, D. T., Hoshino, M., Uesugi, K., Yagi, N., and Pierscionek, B. K. (2019). A modeling approach for investigating opto-mechanical relationships in the human eye lens. *IEEE Transactions on Biomedical Engineering*, 67(4):999–1006.

Wang, K., Venetsanos, D. T., Wang, J., Augousti, A. T., and Pierscionek, B. K. (2017). The importance of parameter choice in modelling dynamics of the eye lens. *Scientific reports*, 7(1):1–12.

Weeber, H. A. and Van Der Heijde, R. G. (2008). Internal deformation of the human crystalline lens during accommodation. *Acta ophthalmologica*, 86(6):642–647.

Wilson, D. J., Jaeger, M. J., and Green, W. R. (1987). Effects of extracapsular cataract extraction on the lens zonules. *Ophthalmology*, 94(5):467–470.

World Health Organization (2002). *Active ageing: A Policy Framework*. Madrid, Spain.

Yavas, G., Öztürk, F., Küsbeci, T., Inan, Ü., Kaplan, Ü., and Ermiş, S. (2009). Evaluation of the change in accommodation amplitude in subjects with pseudoexfoliation. *Eye*, 23(4):822–826.

Scientific Publications

The insight gained in this dissertation allowed for the contribution led by Filomena Ribeiro M.D. in the Chapter Pseudophakic Eye Models, published by IOL Power Club (Ribeiro et al., to appear), where the finite element modeling of the healthy lens complex was approached, as well as the lenticular complex under pseudoexfoliative conditions.

Additionally, the work developed in this dissertation will be presented in the 17th International Symposium on Computer Methods in Biomechanics and Biomedical Engineering and the 5th Conference on Imaging and Visualization (CMBBE 2021) (Jud et al., to appear), where the lens under healthy and pseudoexfoliation conditions is analysed.

Appendix A

Literature Review Auxiliary Data

This appendix accounts for the material properties of the literature data described in Section 2.2.

	Age	Zonules		Capsular Bag		Cortex		Nucleus	
		$E_Z[MPa]$	ν_Z	$E_{CB}[MPa]$	ν_{CB}	$E_C[kPa]$	ν_C	$E_N[kPa]$	ν_N
Cardoso (2018)	X	0.35	0.47	1.50	0.47	3.70	0.47	0.60	0.47
Bahrami et al. (2016)	27	10.00	X	5.00	0.47	0.60 - 3.00	0.49	0.60	0.49
Hermans et al. (2006)	29	applied forces		1.27	0.47	3.42	0.49	0.55	0.49
Paulino (2019)	29	Table 3.2		1.50	0.47	3.70	0.47	0.60	0.47
Lanchares et al. (2012)	30	applied forces		X	x	X	X	X	X
Wang et al. (2017)	35	0.35	0.47	4.90	0.47	3.70	0.47	0.60	0.47
Burd et al. (2002)	45	X	X	1.45	0.47	3.98	0.49	0.99	0.49
Hermans et al. (2008)	45	applied forces		1.45	0.47	1.37	0.49	3.43	0.49
Belaidi and Pierscionek (2007)	46	X	X	3.90	0.47	4.00	0.47	1.00	0.47
Wang et al. (2016)	48	0.35	0.47	4.20	0.47	4.00	0.49	1.10	0.49
Weeber and Van Der Heijde (2008)	60	0.35	0.47	1.50	0.47	6.25 - 108.50*	0.50	6.25 - 108.50*	0.50
Bocskai and Bojtár (2013)	60	1.50	0.40	1.45	0.47	3.818	0.49	5.25	0.49
Wang et al. (2019)	62	0.35	0.47	1.50	0.47	0.43	X	0.82	X

Table A.1: Literature data concerning the material properties of the lens complex components. (X - Data not made available by the authors; * - Authors considered the lens as a single structure)

Appendix B

Central Optical Power parameters

The present appendix aims to introduce the reader to the parameters used in the calculation of the Central Optical Power. The coordinates of the nodes depicted in Figure 3.11 are described in Table B.1.

	x	y	z
a_1	0.00	1.87	-2,53
a_2	0.00	2.03	-1,49
a_3	0.00	2.09	-0,45
a_4	0.00	2.09	0,45
a_5	0.00	2.03	1,49
a_6	0.00	1.87	2,53
p_1	0.00	-2.07	-2,44
p_2	0.00	-2.40	-1,46
p_3	0.00	-2.57	-0,44
p_4	0.00	-2.57	0,44
p_5	0.00	-2.40	1,46
p_6	0.00	-2.07	2,44

Table B.1: Node coordinates used to calculate the anterior and posterior radii of curvature.

Table B.2 displays the node combinations used in order to obtain 20 anterior radii of curvature, which were then averaged in order to obtain a radius of curvature for each of the 7 stages of the simulation, from the accommodated state to the relaxed state. Nonetheless, for the calculation of the posterior radius of curvature, the same table is valid.

Radius of Curvature			
Combination	1st node	2nd node	3rd node
1	a_1	a_2	a_3
2	a_1	a_2	a_4
3	a_1	a_2	a_5
4	a_1	a_2	a_6
5	a_1	a_3	a_4
6	a_1	a_3	a_5
7	a_1	a_3	a_6
8	a_1	a_4	a_5
9	a_1	a_4	a_6
10	a_1	a_5	a_6
11	a_2	a_3	a_4
12	a_2	a_3	a_5
13	a_2	a_3	a_6
14	a_2	a_4	a_5
15	a_2	a_4	a_6
16	a_2	a_5	a_6
17	a_3	a_4	a_5
18	a_3	a_4	a_6
19	a_3	a_5	a_6
20	a_4	a_5	a_6

Table B.2: Node combinations used to calculate radius of curvature

Appendix C

Developed *in silico* Models

The present appendix accounts for all the results obtained for the developed *in silico* models of this dissertation.

Healthy Lens Models

Model	Lens			Zonules				Capsular Bag							Cortex and Nucleus				
	$\Delta T_L[\%]$	$\Delta R_L[\%]$	$\Delta COP[D]$	$F_Z[mN]$	$VM_{min}[kPa]$	$VM_{avg}[kPa]$	$VM_{max}[kPa]$	LE_{min}	LE_{max}	$S_{min}[kPa]$	$S_{max}[kPa]$	$VM_{min}[kPa]$	$VM_{avg}[kPa]$	$VM_{max}[kPa]$	$S_{min}[kPa]$	$S_{max}[kPa]$	$VM_{min}[kPa]$	$VM_{avg}[kPa]$	$VM_{max}[kPa]$
Initial Model	14,20	7,87	1,57	134,1	65,16	110,30	150,16	0,0166	0,0825	41,52	171,59	46,05	74,32	149,47	-0,642	0,841	0,020	0,079	0,188
Oval-5.6	15,20	8,14	2,03	142,8	64,40	114,32	182,45	0,0203	0,0878	40,53	180,09	50,85	81,62	164,39	-0,581	0,638	0,021	0,083	0,215
Oval-2.8	14,59	7,99	1,73	138,0	65,03	110,70	161,19	0,0177	0,0850	42,02	176,25	47,85	76,31	153,44	-0,641	0,755	0,016	0,081	0,202
Oval+2.8	13,86	7,76	1,45	131,4	63,32	103,63	149,86	0,0166	0,0824	40,99	171,83	44,70	72,36	149,74	-0,626	0,748	0,016	0,078	0,198
Oval+5.6	13,55	7,66	1,38	129,9	61,25	99,92	149,69	0,0171	0,0823	40,29	171,72	43,53	70,75	149,67	-0,616	0,752	0,016	0,077	0,196
Band1	13,60	7,86	1,30	113,4	59,69	99,75	141,79	0,0173	0,0842	46,36	197,36	44,99	72,62	178,78	-0,517	0,799	0,014	0,078	0,201
Band2	13,63	7,89	1,34	114,4	59,56	100,09	144,70	0,0170	0,0846	46,39	177,64	45,01	71,79	155,01	-0,615	0,755	0,015	0,078	0,199
Band3	13,59	7,90	1,32	112,9	59,26	99,73	142,38	0,0171	0,0847	32,27	166,38	44,79	71,24	144,09	-0,662	0,784	0,014	0,077	0,183
Band4	13,61	7,87	1,33	113,7	59,61	99,84	141,89	0,0171	0,0844	46,70	181,54	45,28	73,08	159,42	-0,576	0,764	0,014	0,077	0,202
Band5	13,59	7,90	1,32	113,5	59,39	99,85	143,82	0,0171	0,0847	43,34	177,51	45,12	72,02	154,84	-0,515	0,760	0,018	0,077	0,204
Band6	13,58	7,87	1,32	113,0	59,44	99,62	141,99	0,0171	0,0846	43,09	173,41	45,33	71,56	150,69	-0,622	0,768	0,015	0,077	0,201
Band7	13,56	7,88	1,31	113,3	59,41	99,64	142,25	0,0171	0,0845	40,08	170,24	45,19	71,17	147,62	-0,643	0,770	0,018	0,077	0,199
Gravity Model	13,35	7,94	1,24	112,1	58,13	99,08	144,25	0,0169	0,0853	30,11	182,57	44,81	73,38	160,07	-0,471	0,637	0,018	0,076	0,210

Table C.1: Results found for the healthy lens complex models.

Inferior Dialysis Graphical Results

The outcomes for the resulting lens thickness variation, lens radius variation, amplitude of accommodation, total zonular force, average Von-Mises stress values in the capsule, maximum Von-Mises stress values in the zonules, and maximum Von-Mises stress values in the cortex and nucleus are represented in the following figures, which represent the models with inferior dialysis.

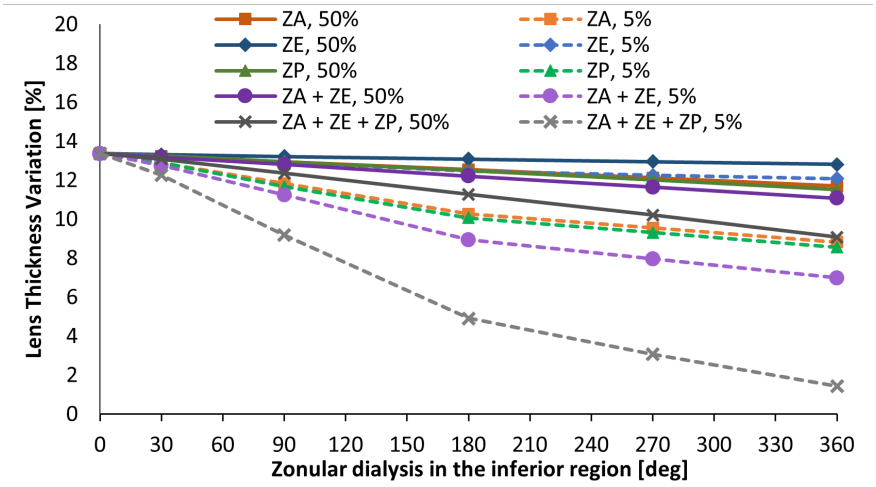

Figure C.1: Lens thickness variation for models with initial inferior dialysis.

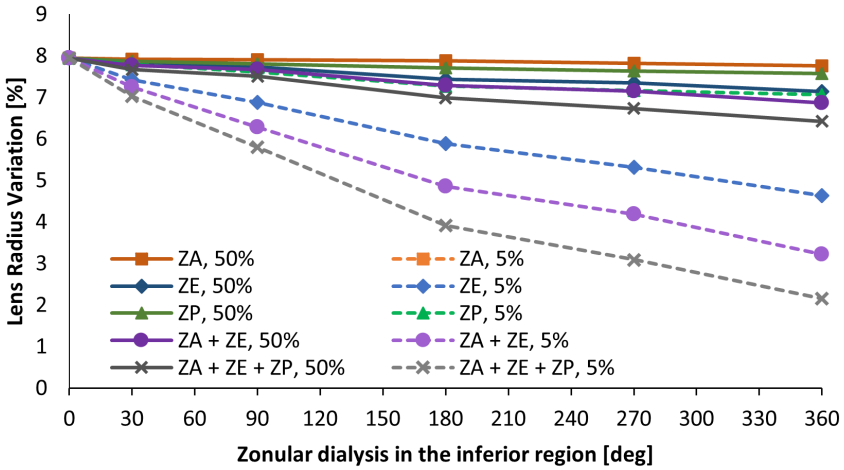

Figure C.2: Lens radius variation for models with initial inferior dialysis.

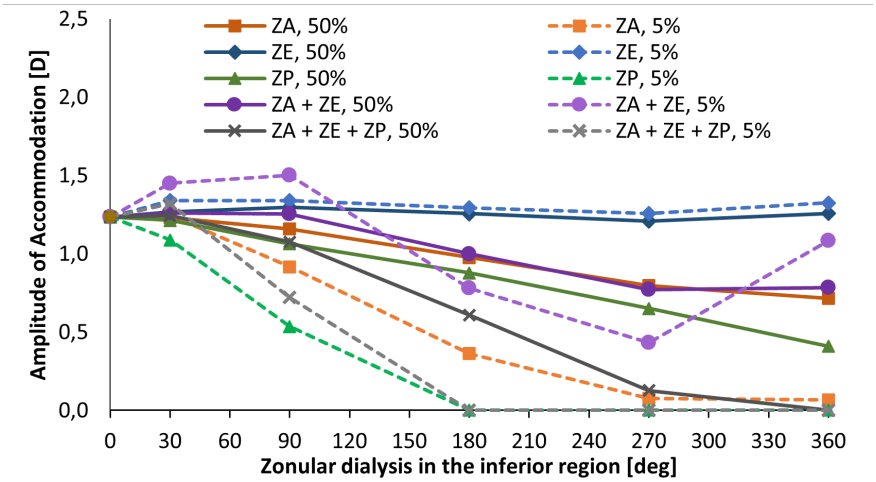

Figure C.3: Amplitude of accommodation for models with initial inferior dialysis.

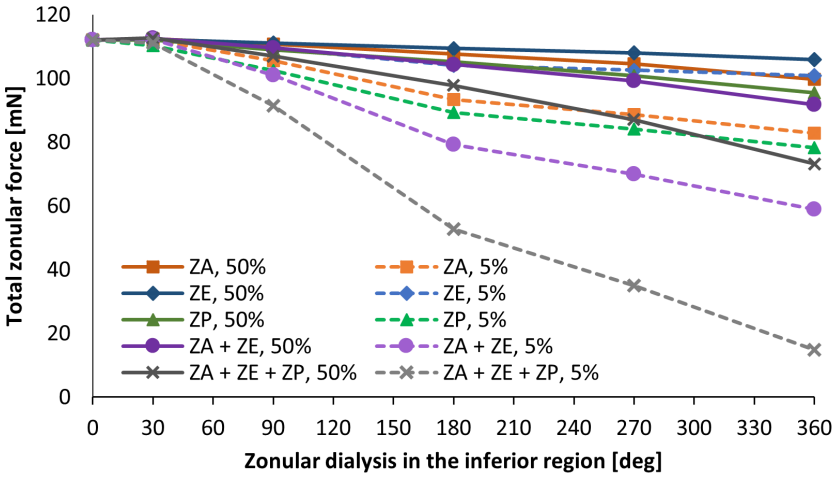

Figure C.4: Total zonular force for models with initial inferior dialysis.

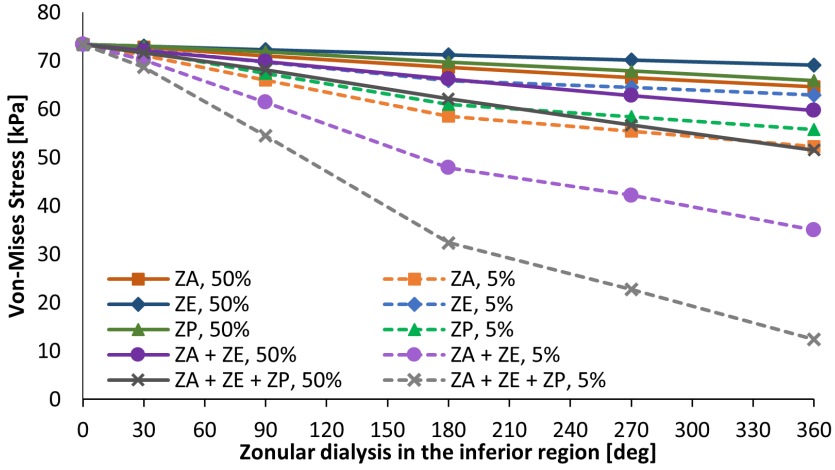

Figure C.5: Average Von-Mises stress in the capsular bag for models with initial inferior dialysis.

Approximation Error and Pseudoexfoliation Models

The approximation error accounts for the percentage difference between the inferior and superior dialysis results, and is given by Equation 4.2. The results found for this value are presented in the

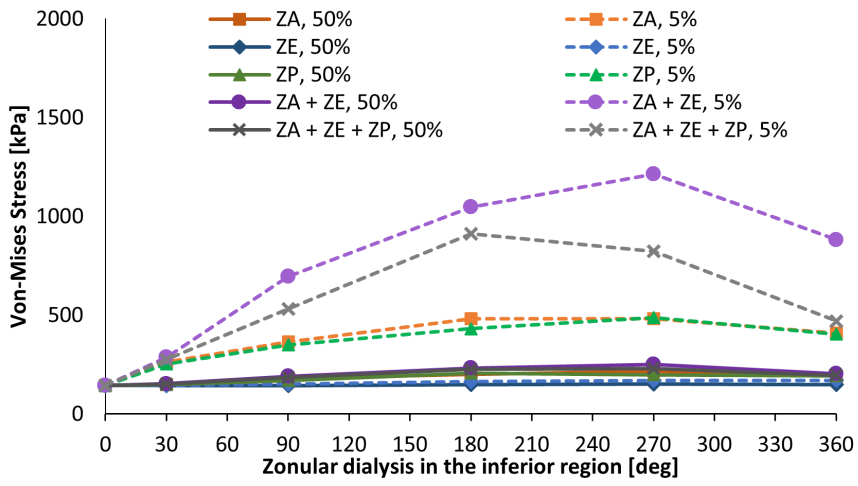

Figure C.6: Maximum Von-Mises stress in the zonules for models with initial inferior dialysis.

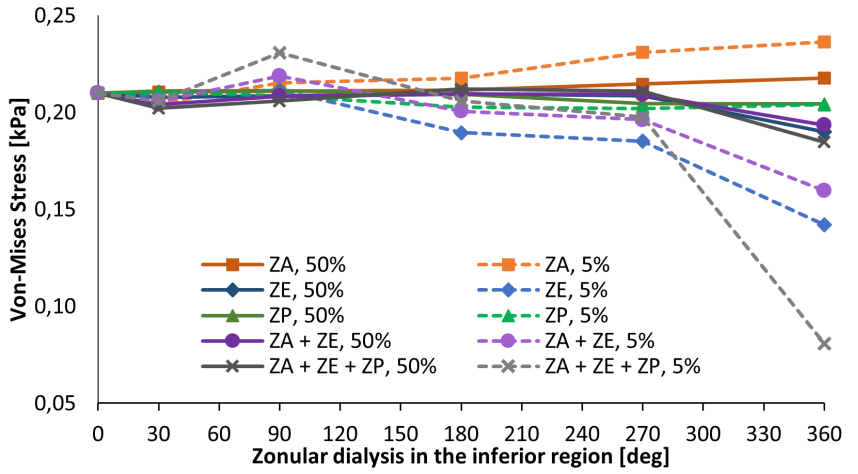

Figure C.7: Maximum Von-Mises stress in the cortex and nucleus for models with initial inferior dialysis.

following tables, where this quantity was measured for each of the individual sets of zonules considered, as well as the groupings of the anterior and equatorial zonules, and the three sets of zonules.

Zonules	Severity	Clock Hours	Models	F_Z	VM_{CB}	VM_Z	VM_{C+N}	ΔCOP
ZA	Moderate	1	1 vs 9	-0,3	1,0	-5,7	0,3	-4,9
		3	3 vs 11	-0,7	0,0	-2,6	-0,6	2,9
		6	5 vs 13	-1,3	0,0	-11,6	-0,3	2,8
		9	7 vs 15	-1,2	0,0	-6,3	0,2	2,2
	Severe	1	2 vs 10	-0,9	0,3	-11,5	-7,8	-2,1
		3	4 vs 12	-1,5	-0,2	-13,7	-6,6	6,8
		6	6 vs 14	-1,2	-0,4	-29,1	-5,1	7,2
		9	8 vs 16	-0,9	-0,4	-35,5	-0,1	15,7
Maximum approximation error, $\lambda_{max}[\%]$				-0,3	1,0	-2,6	0,3	15,7
Average approximation error, $\overline{\lambda}[\%]$				-1,0	0,0	-14,5	-2,5	3,8
Minimum approximation error, $\lambda_{min}[\%]$				-1,5	-0,4	-35,5	-7,8	-4,9

Table C.2: Approximation error results for the disruption of the anterior zonular fibers.

Zonules	Severity	Clock Hours	Models	F_Z	VM_{CB}	VM_Z	VM_{C+N}	ΔCOP
ZE	Moderate	1	19 vs 27	-0,1	0,0	-1,3	-2,1	0,1
		3	21 vs 29	-0,4	0,0	-1,6	3,5	0,1
		6	23 vs 31	-0,5	0,0	-2,1	6,8	0,2
		9	25 vs 33	-0,5	0,0	-1,6	9,1	0,1
	Severe	1	20 vs 28	-0,4	0,0	-1,5	3,3	0,5
		3	22 vs 30	-0,8	-0,1	-2,1	8,0	1,1
		6	24 vs 32	-0,6	-0,3	-1,8	13,9	-0,1
		9	26 vs 34	-0,8	-0,2	-4,4	27,1	0,7
Maximum approximation error, $\lambda_{max}[\%]$				-0,1	0,0	-1,3	27,1	1,1
Average approximation error, $\overline{\lambda}[\%]$				-0,5	-0,1	-2,1	8,7	0,4
Minimum approximation error, $\lambda_{min}[\%]$				-0,8	-0,3	-4,4	-2,1	-0,1

Table C.3: Approximation error results for the disruption of the equatorial zonular fibers.

Zonules	Severity	Clock Hours	Models	F_Z	VM_{CB}	VM_Z	VM_{C+N}	ΔCOP
ZP	Moderate	1	37 vs 45	-0,3	0,0	-6,1	0,8	2,2
		3	39 vs 47	-0,9	0,0	-7,8	0,7	4,6
		6	41 vs 49	-1,3	0,0	-14,0	0,7	4,1
		9	43 vs 51	-1,1	0,0	-8,5	0,7	3,0
	Severe	1	38 vs 46	-1,0	-0,1	-13,6	0,6	6,0
		3	40 vs 48	-1,7	-0,1	-16,9	0,5	18,2
		6	42 vs 50	-1,6	-0,1	-25,9	0,0	0,0
		9	44 vs 52	-1,5	-0,2	-27,4	-0,2	0,0
Maximum approximation error, $\lambda_{max}[\%]$				-0,3	0,0	-6,1	0,8	18,2
Average approximation error, $\overline{\lambda}[\%]$				-1,2	-0,1	-15,0	0,5	4,8
Minimum approximation error, $\lambda_{min}[\%]$				-1,7	-0,2	-27,4	-0,2	0,0

Table C.4: Approximation error results for the disruption of the posterior zonular fibers.

Zonules	Severity	Clock Hours	Models	F_Z	VM_{CB}	VM_Z	VM_{C+N}	ΔCOP
ZA+ZE	Moderate	1	55 vs 63	-0,5	0,0	-5,6	-2,8	1,4
		3	57 vs 65	-1,0	0,0	-6,1	-1,7	2,8
		6	59 vs 67	-1,4	0,0	-12,0	9,2	3,1
		9	61 vs 69	-1,1	0,0	-2,6	11,2	2,6
	Severe	1	56 vs 64	-1,1	-0,2	-6,1	-3,2	2,4
		3	58 vs 66	-1,9	-0,3	-11,7	11,9	0,7
		6	60 vs 68	-2,5	-0,9	-14,6	16,4	-3,1
		9	62 vs 70	-2,5	-1,1	-15,0	27,1	-10,6
Maximum approximation error, $\lambda_{max}[\%]$				-0,5	0,0	-2,6	27,1	3,1
Average approximation error, $\overline{\lambda}[\%]$				-1,5	-0,3	-9,2	8,5	-0,1
Minimum approximation error, $\lambda_{min}[\%]$				-2,5	-1,1	-15,0	-3,2	-10,6

Table C.5: Approximation error results for the disruption of the anterior and equatorial zonular fibers.

Zonules	Severity	Clock Hours	Models	F_Z	VM_{CB}	VM_Z	VM_{C+N}	ΔCOP
ZA+ZE+ZP	Moderate	1	73 vs 81	-0,8	0,0	-5,7	-3,1	3,7
		3	75 vs 83	-1,6	0,0	-8,6	-2,5	8,7
		6	77 vs 85	-2,6	0,0	-16,1	11,4	14,0
		9	79 vs 87	-2,6	-0,1	-3,0	17,6	60,1
	Severe	1	74 vs 82	-1,7	-0,3	-6,6	-2,7	9,0
		3	76 vs 84	-3,3	-0,8	-12,9	16,3	23,4
		6	78 vs 86	-6,9	-1,7	-31,1	22,7	0,0
		9	80 vs 88	-10,0	-2,5	-48,0	29,6	0,0
Maximum approximation error, $\lambda_{max}[\%]$				-0,8	0,0	-3,0	29,6	60,1
Average approximation error, $\overline{\lambda}[\%]$				-3,7	-0,7	-16,5	11,2	14,9
Minimum approximation error, $\lambda_{min}[\%]$				-10,0	-2,5	-48,0	-3,1	0,0

Table C.6: Approximation error results for the disruption of the anterior, equatorial and posterior zonular fibers.

All models combinations	F_Z	VM_{CB}	VM_Z	VM_{C+N}	ΔCOP
Maximum approximation error, $\lambda_{max}[\%]$	-0,1	1,0	-1,3	29,6	60,1
Average approximation error, $\overline{\lambda}[\%]$	-1,6	-0,2	-11,5	5,3	4,7
Minimum approximation error, $\lambda_{min}[\%]$	-10,0	-2,5	-48,0	-7,8	-10,6

Table C.7: Approximation error ranges and average values for all the model combinations.

Model	Zonule	Origin	Clock Hours	Severity
1	ZA	Top	1	Moderate
2				Severe
3			3	Moderate
4				Severe
5			6	Moderate
6				Severe
7			9	Moderate
8				Severe
9		Bottom	1	Moderate
10				Severe
11			3	Moderate
12				Severe
13			6	Moderate
14				Severe
15			9	Moderate
16				Severe
17		All	12	Moderate
18				Severe
19	ZE	Top	1	Moderate
20				Severe
21			3	Moderate
22				Severe
23			6	Moderate
24				Severe
25			9	Moderate
26				Severe
27		Bottom	1	Moderate
28				Severe
29			3	Moderate
30				Severe
31			6	Moderate
32				Severe
33			9	Moderate
34				Severe
35		All	12	Moderate
36				Severe
37	ZP	Top	1	Moderate
38				Severe
39			3	Moderate
40				Severe
41			6	Moderate
42				Severe
43			9	Moderate
44				Severe
45		Bottom	1	Moderate
46				Severe
47			3	Moderate
48				Severe
49			6	Moderate
50				Severe
51			9	Moderate
52				Severe
53		All	12	Moderate
54				Severe

Model	Zonule	Origin	Clock Hours	Severity
55	ZA + ZE	Top	1	Moderate
56				Severe
57			3	Moderate
58				Severe
59			6	Moderate
60				Severe
61			9	Moderate
62				Severe
63		Bottom	1	Moderate
64				Severe
65			3	Moderate
66				Severe
67			6	Moderate
68				Severe
69			9	Moderate
70				Severe
71		All	12	Moderate
72				Severe
73	ZA + ZE + ZP	Top	1	Moderate
74				Severe
75			3	Moderate
76				Severe
77			6	Moderate
78				Severe
79			9	Moderate
80				Severe
81		Bottom	1	Moderate
82				Severe
83			3	Moderate
84				Severe
85			6	Moderate
86				Severe
87			9	Moderate
88				Severe
89		All	12	Moderate
90				Severe

Table C.8: Models developed for the pseudoexfolation syndrome.

Model	Lens			Zonules				Capsular Bag							Cortex and Nucleus				
	$\Delta T_L[\%]$	$\Delta R_L[\%]$	$\Delta COP[D]$	$F_Z[mN]$	$VM_{min}[kPa]$	$VM_{avg}[kPa]$	$VM_{max}[kPa]$	LE_{min}	LE_{max}	$S_{min}[kPa]$	$S_{max}[kPa]$	$VM_{min}[kPa]$	$VM_{avg}[kPa]$	$VM_{max}[kPa]$	$S_{min}[kPa]$	$S_{max}[kPa]$	$VM_{min}[kPa]$	$VM_{avg}[kPa]$	$VM_{max}[kPa]$
1	13,21	7,92	1,30	112,8	57,54	100,35	157,18	0,0170	0,0858	29,28	183,07	44,43	72,04	160,42	-0,661	0,707	0,016	0,075	0,210
2	12,88	7,87	1,27	113,0	56,82	103,66	297,27	0,0168	0,0864	28,96	182,98	34,38	70,91	160,30	-0,659	0,721	0,015	0,074	0,222
3	12,93	7,91	1,13	111,6	56,54	101,73	183,10	0,0168	0,0859	23,54	182,61	39,24	70,98	160,07	-0,660	0,718	0,015	0,074	0,212
4	11,76	7,75	0,86	107,2	54,14	117,53	421,40	0,0065	0,0859	7,27	182,66	14,15	66,15	160,35	-0,653	0,756	0,011	0,071	0,230
5	12,51	7,82	0,95	109,0	56,05	107,06	225,23	0,0149	0,0854	28,33	182,19	34,70	68,70	160,06	-0,657	0,726	0,012	0,073	0,212
6	10,21	7,58	0,34	94,6	57,12	142,75	678,38	0,0074	0,0853	15,64	185,06	13,55	58,79	163,53	-0,652	0,779	0,013	0,066	0,229
7	12,10	7,80	0,78	105,8	56,13	109,68	230,66	0,0150	0,0844	27,93	182,15	34,54	66,53	160,37	-0,657	0,728	0,013	0,071	0,214
8	9,51	7,52	0,07	89,5	57,36	152,50	746,32	0,0069	0,0837	14,50	184,52	12,60	55,67	163,13	-0,649	0,781	0,013	0,064	0,231
9	13,23	7,92	1,23	112,4	59,22	100,45	148,26	0,0168	0,0853	30,01	182,59	44,60	72,79	160,08	-0,470	0,638	0,018	0,075	0,210
10	12,90	7,88	1,25	112,0	58,45	103,20	263,07	0,0168	0,0862	31,75	183,73	39,69	71,14	160,89	-0,635	0,653	0,016	0,074	0,205
11	12,94	7,91	1,16	110,8	58,54	101,52	178,26	0,0168	0,0858	27,77	183,07	43,68	70,97	160,43	-0,669	0,701	0,015	0,074	0,211
12	11,82	7,80	0,92	105,6	56,05	115,14	363,64	0,0073	0,0853	18,59	182,79	19,66	66,03	160,30	-0,684	0,706	0,014	0,071	0,215
13	12,53	7,88	0,98	107,6	57,81	106,48	199,05	0,0166	0,0850	28,84	182,36	40,57	68,67	160,09	-0,668	0,707	0,015	0,073	0,211
14	10,27	7,65	0,36	93,4	59,24	137,58	480,84	0,0087	0,0834	20,05	182,71	17,90	58,55	161,18	-0,676	0,735	0,013	0,066	0,218
15	12,11	7,82	0,80	104,5	57,84	109,15	216,08	0,0160	0,0837	28,21	181,54	38,92	66,50	159,76	-0,665	0,717	0,015	0,071	0,215
16	9,55	7,56	0,08	88,7	59,61	147,82	481,52	0,0074	0,0823	17,99	182,50	16,46	55,43	161,70	-0,671	0,748	0,013	0,064	0,231
17	11,69	7,76	0,72	99,7	61,13	111,33	191,06	0,0142	0,0838	28,31	182,05	37,60	64,65	160,38	-0,456	0,648	0,013	0,070	0,218
18	8,82	7,47	0,07	82,7	64,98	154,94	408,85	0,0051	0,0814	11,99	181,23	10,94	52,27	160,91	-0,429	0,696	0,016	0,063	0,236
19	13,30	7,79	1,27	112,4	57,94	100,12	144,01	0,0170	0,0854	28,50	182,62	44,15	73,03	160,26	-0,600	0,704	0,015	0,075	0,212
20	13,19	7,40	1,33	112,7	57,65	101,88	144,52	0,0175	0,0853	17,74	182,15	40,50	72,27	159,81	-0,599	0,700	0,015	0,075	0,202
21	13,20	7,72	1,30	111,4	57,66	102,90	144,55	0,0172	0,0852	25,19	181,92	41,11	72,31	159,60	-0,600	0,691	0,015	0,075	0,202
22	12,87	6,80	1,33	110,3	56,86	109,98	153,96	0,0159	0,0840	0,00	178,91	28,64	69,75	156,88	-0,597	0,598	0,014	0,072	0,196
23	13,07	7,42	1,25	109,9	57,34	106,53	150,77	0,0165	0,0840	24,15	179,12	40,07	71,21	157,06	-0,599	0,633	0,014	0,074	0,196
24	12,41	5,77	1,29	104,8	67,85	120,24	167,32	0,0146	0,0749	0,00	155,58	25,79	66,10	135,60	-0,719	0,505	0,012	0,069	0,166
25	12,94	7,34	1,21	108,5	57,48	106,74	153,25	0,0159	0,0810	23,90	172,18	39,76	70,16	150,74	-0,595	0,635	0,014	0,073	0,191
26	12,24	5,25	1,25	103,3	68,24	125,49	175,93	0,0139	0,0710	0,00	146,40	25,74	64,61	139,98	-0,571	0,487	0,012	0,068	0,146
27	13,30	7,79	1,27	112,2	59,42	100,11	142,17	0,0172	0,0856	31,66	182,76	44,10	73,03	160,29	-0,583	0,627	0,014	0,075	0,208
28	13,21	7,42	1,34	112,3	59,11	101,79	142,31	0,0176	0,0854	31,70	182,81	43,69	72,26	160,34	-0,582	0,628	0,014	0,075	0,209
29	13,22	7,73	1,30	111,0	59,17	102,82	142,26	0,0174	0,0853	31,83	182,65	43,75	72,31	160,21	-0,582	0,626	0,014	0,075	0,209
30	12,92	6,87	1,34	109,5	58,32	109,46	150,69	0,0172	0,0843	30,10	181,34	42,18	69,67	159,19	-0,566	0,606	0,015	0,072	0,212
31	13,08	7,43	1,26	109,4	58,89	106,41	147,61	0,0166	0,0842	30,77	181,19	43,06	71,22	159,05	-0,569	0,601	0,015	0,074	0,210
32	12,46	5,88	1,29	104,1	69,64	119,38	164,23	0,0157	0,0758	16,53	159,50	38,62	65,90	139,23	-0,508	0,582	0,018	0,069	0,190
33	12,95	7,35	1,21	108,0	59,02	106,66	150,78	0,0159	0,0814	27,99	176,91	42,28	70,16	155,84	-0,565	0,575	0,015	0,073	0,209
34	12,25	5,31	1,26	102,5	69,92	125,05	168,18	0,0153	0,0716	0,00	152,64	28,86	64,48	139,78	-0,626	0,578	0,011	0,068	0,185
35	12,80	7,13	1,26	105,9	69,11	106,62	148,61	0,0160	0,0775	25,04	161,84	40,12	69,08	141,08	-0,420	0,582	0,017	0,072	0,190
36	12,07	4,63	1,32	100,8	105,93	130,88	169,28	0,0130	0,0605	0,00	142,77	25,47	62,94	139,55	-0,652	0,486	0,012	0,066	0,142
37	13,25	7,86	1,19	112,3	58,28	100,56	157,23	0,0186	0,0851	39,11	182,27	43,23	72,96	159,84	-0,471	0,641	0,017	0,075	0,210
38	12,87	7,79	1,03	111,4	57,56	103,46	291,29	0,0205	0,0855	25,25	181,84	35,76	72,01	159,30	-0,471	0,648	0,015	0,074	0,209
39	12,92	7,80	1,02	109,9	58,02	101,58	182,59	0,0205	0,0855	25,83	182,10	38,67	71,82	159,73	-0,470	0,647	0,016	0,074	0,210
40	11,61	7,61	0,45	104,3	55,08	115,57	420,22	0,0105	0,0856	19,48	182,03	21,33	67,44	159,32	-0,469	0,665	0,014	0,069	0,207
41	12,47	7,70	0,84	106,6	56,96	106,91	237,72	0,0143	0,0848	30,20	181,14	36,46	69,75	158,72	-0,472	0,652	0,017	0,072	0,208
42	10,01	7,26	0,00	90,8	58,87	137,97	581,30	0,0071	0,0809	18,61	176,38	16,85	61,09	155,59	-0,468	0,677	0,012	0,064	0,203
43	12,00	7,62	0,63	101,9	57,08	109,25	215,25	0,0146	0,0821	25,72	177,73	36,47	67,87	156,90	-0,474	0,654	0,016	0,070	0,203
44	9,28	7,14	0,00	85,3	59,21	145,24	668,70	0,0068	0,0786	17,06	175,27	14,78	58,55	155,57	-0,466	0,679	0,011	0,062	0,202
45	13,26	7,86	1,21	112,0	59,83	100,58	147,71	0,0183	0,0851	41,15	182,11	44,07	72,96	159,69	-0,469	0,688	0,017	0,075	0,211

Table C.9: Results found for the pseudoexfoliation models (1/2).

Model	Lens			Zonules				Capsular Bag							Cortex and Nucleus				
	$\Delta T_L[\%]$	$\Delta R_L[\%]$	$\Delta COP[D]$	$F_Z[mN]$	$VM_{min}[kPa]$	$VM_{avg}[kPa]$	$VM_{max}[kPa]$	LE_{min}	LE_{max}	$S_{min}[kPa]$	$S_{max}[kPa]$	$VM_{min}[kPa]$	$VM_{avg}[kPa]$	$VM_{max}[kPa]$	$S_{min}[kPa]$	$S_{max}[kPa]$	$VM_{min}[kPa]$	$VM_{avg}[kPa]$	$VM_{max}[kPa]$
46	12,89	7,79	1,09	110,3	59,16	103,03	251,68	0,0206	0,0852	32,92	181,94	42,67	71,95	159,49	-0,470	0,691	0,015	0,074	0,210
47	12,94	7,80	1,06	109,0	59,63	101,46	168,31	0,0197	0,0852	31,67	182,05	43,37	71,82	159,59	-0,469	0,687	0,018	0,074	0,211
48	11,66	7,61	0,54	102,5	56,72	112,94	348,99	0,0137	0,0850	25,14	182,51	27,87	67,39	160,30	-0,468	0,705	0,016	0,070	0,209
49	12,48	7,71	0,88	105,3	58,57	106,35	204,44	0,0156	0,0845	31,49	181,63	40,01	69,75	159,44	-0,470	0,696	0,018	0,072	0,209
50	10,06	7,26	0,00	89,3	60,94	133,02	430,60	0,0090	0,0799	21,91	175,42	22,51	61,00	155,01	-0,468	0,695	0,014	0,064	0,203
51	12,00	7,63	0,65	100,8	58,66	108,60	197,01	0,0144	0,0822	27,60	178,35	37,78	67,86	156,98	-0,472	0,700	0,016	0,070	0,205
52	9,31	7,16	0,00	84,1	61,48	140,24	485,60	0,0086	0,0780	19,81	173,48	21,12	58,43	154,70	-0,466	0,696	0,012	0,062	0,202
53	11,51	7,57	0,41	95,5	61,84	110,48	192,08	0,0138	0,0813	28,14	177,85	35,27	65,85	156,93	-0,472	0,655	0,017	0,069	0,204
54	8,55	7,07	0,00	78,2	67,52	144,37	403,54	0,0067	0,0758	17,87	172,42	17,13	55,76	154,53	-0,465	0,677	0,016	0,060	0,204
55	13,17	7,76	1,24	113,1	57,35	101,44	160,91	0,0171	0,0855	28,81	182,51	43,75	72,02	159,95	-0,661	0,704	0,014	0,075	0,210
56	12,72	7,28	1,42	113,4	56,22	107,30	304,56	0,0171	0,0863	21,40	182,72	34,72	70,26	159,85	-0,657	0,713	0,013	0,072	0,212
57	12,77	7,67	1,22	110,6	56,01	106,07	202,82	0,0170	0,0858	17,34	181,85	39,24	69,86	159,24	-0,659	0,671	0,014	0,073	0,212
58	11,19	6,29	1,49	103,0	51,95	151,46	786,07	0,0062	0,0850	0,00	178,87	10,81	61,60	156,54	-0,644	0,631	0,008	0,065	0,196
59	12,18	7,28	0,97	105,8	55,07	116,54	262,07	0,0136	0,0841	23,51	178,81	31,64	66,19	156,70	-0,653	0,646	0,012	0,070	0,192
60	8,92	4,85	0,81	81,2	62,90	235,55	1224,86	-0,0060	0,0726	0,00	151,77	1,29	48,32	136,98	-0,559	0,501	0,005	0,055	0,172
61	11,63	7,14	0,75	100,3	55,41	120,10	255,35	0,0131	0,0815	20,26	172,27	30,29	62,84	150,60	-0,648	0,655	0,012	0,068	0,188
62	7,95	4,18	0,48	71,8	64,62	274,74	1428,66	-0,0090	0,0679	0,00	146,12	0,58	42,63	137,26	-0,533	0,457	0,005	0,051	0,154
63	13,18	7,76	1,26	112,6	58,93	101,41	151,90	0,0172	0,0856	31,98	182,89	44,30	72,01	160,31	-0,636	0,651	0,016	0,075	0,204
64	12,75	7,25	1,45	112,2	57,87	106,86	285,84	0,0170	0,0863	29,46	183,83	39,45	70,15	160,99	-0,633	0,657	0,015	0,073	0,206
65	12,80	7,67	1,26	109,5	57,64	105,83	190,39	0,0170	0,0858	23,76	183,38	42,90	69,84	160,72	-0,635	0,657	0,015	0,073	0,208
66	11,23	6,28	1,50	101,0	53,91	147,17	693,83	0,0091	0,0850	0,00	181,51	15,92	61,40	159,25	-0,625	0,612	0,009	0,066	0,219
67	12,21	7,28	1,00	104,3	56,81	115,65	230,61	0,0154	0,0842	29,57	181,14	36,19	66,16	159,06	-0,631	0,596	0,013	0,071	0,209
68	8,94	4,85	0,78	79,2	66,01	222,02	1045,72	-0,0044	0,0731	0,00	156,80	3,55	47,90	137,57	-0,551	0,571	0,008	0,057	0,201
69	11,64	7,14	0,77	99,2	57,11	119,16	248,62	0,0147	0,0818	25,97	177,66	34,88	62,82	156,39	-0,625	0,601	0,013	0,068	0,209
70	7,96	4,18	0,43	70,0	68,25	257,76	1214,05	-0,0081	0,0691	0,00	150,68	1,41	42,18	137,41	-0,525	0,568	0,010	0,052	0,196
71	11,07	6,86	0,78	91,7	74,18	120,94	203,23	0,0131	0,0747	22,30	158,99	35,22	59,68	139,25	-0,406	0,589	0,013	0,065	0,193
72	6,98	3,22	1,08	58,9	97,06	277,44	881,20	0,0015	0,0608	0,00	145,38	2,40	34,98	137,44	-0,403	0,384	0,005	0,047	0,160
73	13,07	7,67	1,20	113,5	57,56	102,81	159,92	0,0187	0,0851	34,60	181,55	42,08	71,61	159,19	-0,660	0,703	0,013	0,074	0,209
74	12,19	7,07	1,21	113,1	55,55	111,60	293,25	0,0198	0,0859	20,73	181,99	34,08	68,90	159,26	-0,655	0,707	0,014	0,070	0,212
75	12,32	7,51	0,99	108,7	55,90	108,69	201,58	0,0178	0,0857	17,11	181,67	33,53	68,18	158,88	-0,656	0,673	0,014	0,071	0,211
76	9,07	5,81	0,58	94,6	48,50	168,84	609,82	0,0058	0,0875	0,00	180,36	9,42	54,94	156,85	-0,641	0,629	0,008	0,056	0,199
77	11,23	6,99	0,53	100,4	53,78	123,91	269,37	0,0130	0,0839	23,01	178,01	28,91	62,15	156,05	-0,650	0,632	0,012	0,066	0,190
78	4,82	3,94	0,00	56,7	60,26	260,84	1323,00	-0,0006	0,0708	0,00	147,05	1,05	32,92	128,11	-0,540	0,493	0,004	0,036	0,168
79	10,18	6,72	0,08	89,4	54,43	130,46	236,22	0,0129	0,0812	18,79	171,62	28,36	56,74	150,01	-0,640	0,640	0,010	0,061	0,179
80	3,03	3,09	0,00	38,8	56,72	315,36	1581,00	-0,0013	0,0631	0,00	133,49	0,12	23,35	116,72	-0,487	0,464	0,001	0,026	0,153
81	13,08	7,67	1,24	112,7	59,24	102,78	150,84	0,0183	0,0851	41,70	182,11	44,07	71,59	159,70	-0,635	0,650	0,016	0,074	0,202
82	12,24	7,02	1,32	111,1	57,35	110,82	274,04	0,0209	0,0857	28,79	182,97	39,31	68,69	160,37	-0,632	0,659	0,014	0,071	0,206
83	12,36	7,50	1,08	106,9	57,70	108,29	184,22	0,0202	0,0855	23,60	182,20	41,36	68,15	159,73	-0,631	0,659	0,017	0,071	0,206
84	9,18	5,79	0,72	91,4	50,91	162,00	531,34	0,0084	0,0868	0,00	184,99	14,03	54,51	161,99	-0,625	0,608	0,011	0,058	0,231
85	11,27	6,98	0,61	97,8	55,72	122,42	225,90	0,0143	0,0837	25,90	180,27	35,99	62,12	158,40	-0,628	0,592	0,013	0,067	0,212
86	4,90	3,92	0,00	52,7	64,31	239,51	911,82	0,0016	0,0709	0,00	153,47	3,55	32,36	135,02	-0,534	0,587	0,007	0,039	0,206
87	10,20	6,73	0,13	87,0	56,32	128,75	229,24	0,0129	0,0816	25,39	177,15	32,97	56,71	155,96	-0,618	0,597	0,012	0,062	0,211
88	3,07	3,09	0,00	34,9	64,12	278,59	822,01	0,0010	0,0649	1,96	143,21	1,70	22,75	126,79	-0,483	0,571	0,006	0,028	0,198
89	9,08	6,42	0,00	73,1	78,14	132,39	195,44	0,0114	0,0694	20,45	151,32	28,54	51,51	133,41	-0,420	0,611	0,013	0,057	0,185
90	1,42	2,15	0,00	14,9	149,47	274,59	469,80	-0,0001	0,0250	0,00	56,69	0,23	12,41	50,68	-0,187	0,361	0,002	0,017	0,081

Table C.10: Results found for the pseudoexfoliation models (2/2).